# MICROFLUID FLOW AND PARTICLE TRANSPORT IN EVAPORATING DROPS

*A Thesis Submitted in the Partial Fulfillment of the Requirements for the Award of the Degree of*

***Doctor of Philosophy***

*by*

**Ashish Kumar Thokchom**

Department of Chemical Engineering

Indian Institute of Technology Guwahati

Assam-781039, India

June 2015

*Dedicated to*

*my Grandma and my family*

# CERTIFICATE

*It is certified that the work contained in the thesis entitled "**Microfluid flow and particle transport in evaporating drops**," by **Ashish Kumar Thokchom**, has been carried out under our supervision and that this work has not been submitted elsewhere for a degree.*

Date: _____


Dr. Anugrah Singh

Professor

Department of Chemical Engineering

IIT Guwahati, Guwahati 781039

India

Dr. Subarata Kumar Majumdar

Associate Professor

Department of Chemical Engineering

IIT Guwahati, Guwahati 781039

India

# Acknowledgement

*I would like to show my gratitude to my advisor, Dr. Anugrah Singh, for giving me an opportunity to work in Flow Visualization Lab. I genuinely appreciate the advice, support, and patience he has shown to me throughout this journey. With his helpful discussion and positive encouragement inspired me to become a good researcher. I would also like to thank my co-advisor Dr. Subrata K Majumder for his kind advice and encouragement.*

*I would like to thank my Doctoral committee: Dr. Pallab Ghosh, Dr. VS Mohalkar and Dr. Ujjal Kumar Saha for their time and guidance. I also like to thank Mr. Bhaskar Medhi Joyti for his sincere help and contribution during my PIV experiments. I sincerely thank Dr. Rajaram Swaminathan for giving me an opportunity to work together during my research work on biological suspension. I also sincerely thank Mr. Menish K. Medhi during my fabrication work in central workshop facility, Indian Institute of Technology Guwahati.*

*Thank to my lab mates and friends: S. Yadav, Mallikarajun Reddy, Abhishek Gupta, Niloy De, Dharmendra Reddy, Sudhershan, Vipin Agarwal, Emran, Aslum, Srinivas R., Jaijus P.J., Ashok Kumar and Saumya Prasad. I would like to thank all the friends, faculty, staff, and students in Department of Chemical Engineering, Indian Institute of Technology Guwahati.*

*My special gratitude to my brother Peshojit Thokchom, my sister Lushina Thokchom, my aunty Anuradha Thokchom and finally my parents Mr. Mangi Singh Thokchom and Mrs. R.K. Pashot Devi. They have always supported and encouraged and have been there in every step of the way. I would also like to thank my wife, Thounaojam Bembem and my parents in-law, Thounaojam Kishorchand and Koijam Rajlakshmi for their love and support.*

Ashish Kumar Thokchom

# Abstract

Formation of ring like structure after complete evaporation of droplet on a substrate is ubiquitous in nature. This phenomenon is not specific to the coffee drop but it can be seen in a drying drop of colloidal suspension such as blood, paint etc. This seemingly simple phenomenon has acquired great attention in the recent years due to its wide applications. Many applications such as DNA microarray, inject printing, paint etc. are associated with this simple phenomenon. Controlling of this phenomenon is problematic in these applications and a complete understanding of underlying mechanism of this phenomenon is required.

Some recent studies have shown that the final deposition pattern on the substrate is strongly affected by the fluid motion inside the evaporating droplet with pinned contact. Most of the previous studies believed that the coffee ring structure is caused by the radial outward flow from the center to the edge of the droplet. Some studies have shown that the secondary fluid flow inside the evaporating droplet known as Marangoni flow can suppress the coffee ring effect. Subsequent studies have been explored that the formation of coffee ring structure can also be controlled by the particle-particle interaction, particle-substrate interaction and nature of the substrate. The objective of our work is to determine the internal fluid flow pattern, particle concentration, and particle deposition pattern in evaporating droplet through experimental measurement as well as numerical simulation. Qualitative visualization of flow patterns inside the droplet may provide better understanding about the particle transport inside the evaporating droplet. In this study, the internal fluid flow and deposition pattern of the evaporating droplet of polystyrene particles placed on substrate was investigated through experiment using Particle image Velocimetry (PIV) technique. External heating of the substrate modifies the surface

temperature distribution of the droplet which generates internal fluid flow consequently affecting the final deposition pattern of the dispersed particles. Despite this, many aspects of fluid flow, particle transport, heat and mass transfer associated with this phenomenon are yet to be completely understood. Recently, researchers believed that uniform surface temperature distribution for all the conditions of evaporation is not reasonable and a non-monotonic surface temperature profile must exist during the transition period i.e. when the contact angle is near to the critical value. In this study, we have realized the non-monotonic temperature variation along the droplet surface experimentally and resulting fluid flow patterns inside the droplet was measured.

Recently, pattern formation of various biofluids has been studied due to potential applications in development of simple and inexpensive rapid disease diagnostic devices. Due to the complex nature of biofluids, a comprehensive understanding of the underlying mechanism of pattern formation is lacking. In this study, the effect of chemotaxis on such pattern formation has been realized experimentally in drying droplets of bacterial suspensions. The velocity field, concentration profile and deposition pattern in the evaporating droplet of *E. coli* suspension in the presence and absence of nutrients were investigated. Finally, we demonstrate the internal fluid flow and particles distribution pattern of sessile droplet placed on curved surface through experimental as well as numerical simulation.

# Contents

# List of Figures

# List of table

# Nomenclature

**Notation**

| | |
|---|---|
| A | Contact area of the droplet |
| $B_o$ | Bond number |
| $C_p$ | Specific heat of the liquid (J/kg-K) |
| $D_{vap}$ | Diffusivity of water vapor ($m^2/s$) |
| $f_i$ | Fraction of solid surface wet by liquid droplet |
| $F_1$ | Force due to evaporation |
| $F_2$ | Force between the suspended particles and substrate |
| $F_3$ | Force due to secondary flow |
| $F_4$ | Force due to particle-particle interaction |
| Gr | Grashoff number |
| H | Relative humidity |
| $h_o$ | Height of the droplet (mm) |
| $h_s$ | Thickness of the substrate (mm) |
| $H_{vap}$ | Heat of water vaporization (kJ/kg) |
| *j* | Evaporation flux (J/s) |
| $M_a$ | Marangoni number |
| N | Number of particles |
| $N_i/N_T$ | Average particles density |
| P | Pressure ($N/m^2$) |
| Q | Heat flux |
| r | Roughness of the substrate |

| | |
|---|---|
| $R_D$ | Peak |
| $R_F$ | Inherent noise |
| $R_{II'}$ | Cross correlation function |
| $\Delta T$ | Temperature gradient |
| <U> | Average radial velocity. |
| *U* | Velocity of liquid in *x*-direction (m/s) |
| *v* | Velocity of liquid in *y*-direction (m/s) |
| $V_d$ | Volume of the droplet |
| *x* | Location of the particles |
| $\Delta X$ | Displace of particles in the fluid |

**Abbreviations**

| | |
|---|---|
| CCD | Charge Couple Device |
| DDPIV | Defocussing Digital Particle Image Velocimetry |
| GFP | Green Fluorescent Protein |
| IR | Infrared |
| LED | Light Emitting Diode |
| OCT | Optical Coherent Topography |
| PIV | Particle Image Velocimetry |

**Subscript**

| | |
|---|---|
| a | Apex of the droplet |
| cond | Conduction |
| e | Edge of the droplet |

| | |
|---|---|
| evap | Evaporation |
| L | Liquid |
| LV | Liquid-vapor |
| s | Substrate |
| SL | Solid-liquid |
| SV | Solid-vapor |
| Tot | Total |
| vap | Vapor |

***Greek Symbol***

| | |
|---|---|
| θ | Contact angle of the droplet |
| θ* | Contact angle of the droplet on rough surface |
| $\rho$ | Density of droplet liquid (kg/m$^3$) |
| $\rho_{vap}$ | Density of water vapor(kg/m$^3$) |
| $\mu$ | Droplet liquid viscosity (kg/m-s) |
| ϒ | Interfacial surface force (N/m) |
| σ | Local value of surface tension (N/m) |
| Ω | Liquid/gas surface tension (N/m) |
| *k* | Thermal conductivity (W/m. K) |

# CHAPTER 1

# Introduction and Literature Survey

## 1.1 Introduction

Microdroplets are of great interest because their physiochemical properties and dynamics is associated with many industrial and biological applications such as microfluidics, lap on chip, micro-nano patterning, inkjet printing, disease diagnostics technique etc. (Larson *et al.*, 2014; Trantum *et al*, 2014; Yunker *et al.*, 2011). Evaporation of droplet is one of the important aspects that have attracted much scientific attention. There are numbers of interesting mechanism involved in the evaporation of microdroplet. In this section, several physical mechanisms related to microdroplet placed on solid substrate are discussed. The fundamental concepts on shape of the microdroplet, Young's equation, surface tension, drops on inhomogeneous surface and evaporation of droplet are also discussed. The governing equation for volume of the evaporating droplet, evaporation rate, particle distribution and surface temperature along the droplet interface are presented in this section. Finally, on the coffee ring stain formation is discussed in detail.

### 1.1.1 Shape of the microdroplet

The shape of the droplet depends on the volume of liquid. It is easily observed that the large volume of liquid droplet rested on flat surface have a flattened shape whereas small

liquid droplets have a spherical cap as shown in Figure 1.1 (Berthier, 2008). This observation is based on the balance between the gravity and surface tension. The shape of microdroplet is governed by the interfacial surface tension whereas the shape of the large liquid droplet results from a balance between the two forces. The shape of the liquid droplet is characterized by the capillary length, *l*. The capillary length is defined as the ration of Laplace pressure to hydrostatic pressure (de Gennes *et al*., 2004). Therefore,

$$\frac{\Delta P_{Laplace}}{\Delta P_{Hydrstatic}} = \frac{\frac{\gamma}{l}}{\rho g l} \tag{1.1}$$

where $\gamma$ is the surface tension, $g$ is the gravity and ρ is the density of the liquid.

When the two pressure are of the same order then,

$$l = \sqrt{\frac{\gamma}{\rho g}} \tag{1.2}$$

A diameter of the liquid droplet smaller than capillary length has a shape resembling that of a spherical cap whereas liquid droplet larger than capillary length is flattened by the gravity.


**Figure 1.1.** The shape of the liquid droplet by placing the droplet on a horizontal surface: (a) small droplet and (b) large droplet.

## 1.1.2 Interfacial forces near the contact line

The interactions between the solid, liquid and gas in the evaporating droplet are controlled by the interfacial energy between these phases. The interface may deform or change shape

to minimize the surface energy of the system, resulting in the change of droplet shape discussed in the previous section.

The liquid molecules experience various intermolecular forces such as van der Waals forces, electrostatic forces, hydrogen bond etc. The molecules at the interface experiences the energy imbalance caused by the greater interaction between the same liquid molecules compared to that between the liquid and gas molecules, which results to minimize the surface energy. For example, consider the potential energy between the liquid molecules as U. The liquid molecules at the liquid-vapor interface will experience an energy loss of U/2. The surface tension, γ, is a measure of this energy loss per unit surface area or,

$$\gamma = \left[\frac{\partial U}{\partial A}\right]_{T,V,n} \tag{1.3}$$

where, T is the temperature, V is the volume of the liquid and n is the number of the molecules in the system.

Each of the three interfaces in the sessile microdroplet has a particular free energy per unit area. Figure 1.2 illustrates the existence of interfacial tension near the contact line of the sessile droplet placed on the substrate. When the droplet is in equilibrium, the forces acting on the contact line should be zero. As per Young's equation it can be expressed as:

$$\Upsilon_{SV} - \Upsilon_{SL} - \Upsilon_{LV}\cos\theta = 0 \tag{1.4}$$

where $\Upsilon_{SV}$, $\Upsilon_{SL}$ and $\Upsilon_{LV}$, are the surface forces of the solid/vapor, solid/liquid and liquid/vapor interfaces at the contact. This equation holds that the system must be is in the thermodynamic equilibrium and the surface should be flat, smooth and free from contamination.

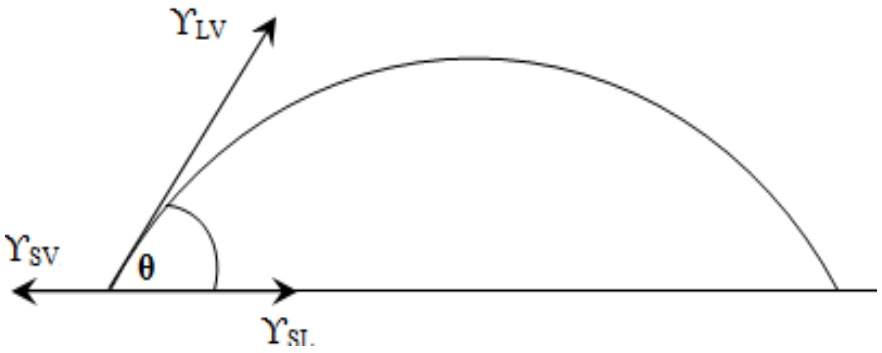


**Figure 1.2.** Interfacial forces at the contact line of an evaporating droplet.

Well microfrabicated surfaces have some roughness and may not be chemically homogeneous as shown in Figure 1.3. The correction is required in Young's Law to take into account of imperfection of the surfaces. The contact angle of the liquid droplet and solid surface can be modified by the roughness of the surface. The roughness of the surface amplifies the hydrophilic or hydrophobic properties of the substrate (de Gennes *et al.*, 2004).

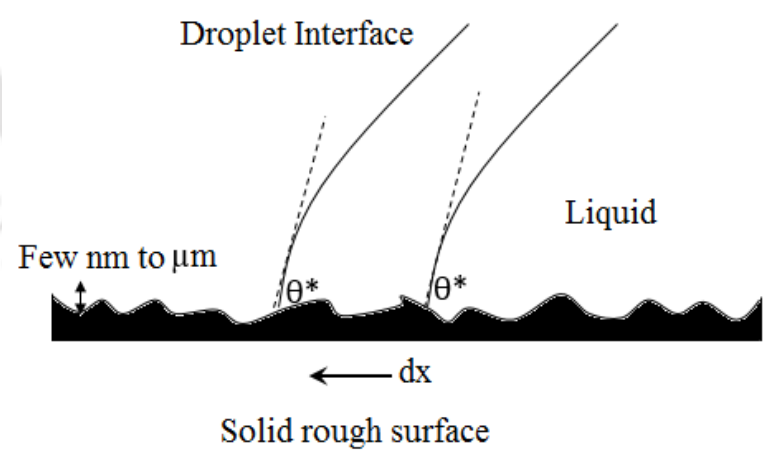


**Figure 1.3.** Liquid drop in contact with rough surface.

Suppose a small displacement, dx of the contact line of the droplet placed on a rough surface occurs as shown in Figure 1.3. The work done on the contact line is given by

$$dW= (\Upsilon_{SL} -\Upsilon_{SV}) rdx+ \Upsilon_{LV} \cos \theta^* dx \quad (1.5)$$

where r is the roughness of the surface. Thus the change of energy is

$$dE = dW= (\Upsilon_{SL} - \Upsilon_{SV}) rdx+ \Upsilon_{LV} \cos \theta^* dx \quad (1.6)$$

At equilibrium state the energy is minimum and this implies

$$\frac{dE}{dx} =0 \quad (1.7)$$

Hence, the equation (1.5) becomes,

$$(\Upsilon_{SL} - \Upsilon_{SV}) r+ \Upsilon_{LV} \cos \theta^*=0 \quad (1.8)$$

Recalling equation (1.4) and equating with equation (1.8), the Wenzel's equation can be obtained as

$$\cos \theta^* = r \cos \theta \quad (1.9)$$

where r is the roughness of the substrate. By definition r > 1.

When a liquid droplet is placed on a heterogeneous surface, the Wenzel law is not sufficient. A more complex model is required to measure how the apparent contact angle changes when various materials are involved. This heterogeneous surface as shown in Figure 1.4 can be explained using the Cassie–Baxter equation

$$\cos \theta^* = \sum_i f_i \cos \theta_i \quad (1.10)$$

$$\sum_i f_i = 1$$

where $f_i$ are the solid fraction of the i materials.

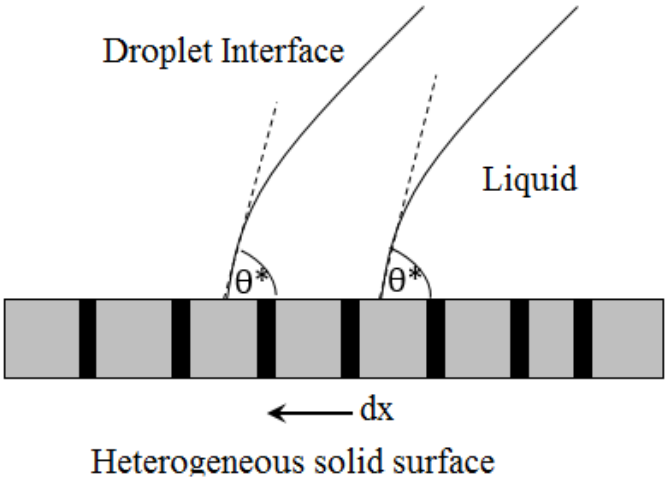


**Figure 1.4.** Contact line of the droplet on heterogeneous surface.

### 1.1.3 Evaporation of droplet

Evaporation of droplet is an inevitable natural process. Evaporation of droplet placed on the substrate causes the volume of the droplet to decrease until it completely dries. Three mechanisms influence the evaporation process. The first is change of phase from liquid to vapor: the rate at which liquid molecules cross the droplet interface. The second mechanism is transport of liquid molecules from droplet interface to the surrounding. This transport can be purely diffusion or a combination of both diffusion as well as natural convection. The third smechanism is the rate-limiting step, which involves the evaporative cooling and heat transfer to liquid-air interface.

Evaporation of drop can occur in two basic modes. The first one is the constant area mode, in which the contact line remains pinned and the contact angle of the droplet decreases with time as shown in Figure 1.5a. The second mode is the constant angle mode, in which the contact line is free to move and contact area decreases as shown in Figure 1.5b. On rough surfaces contact area mode prevails whereas on smooth surface contact angle mode can exit.

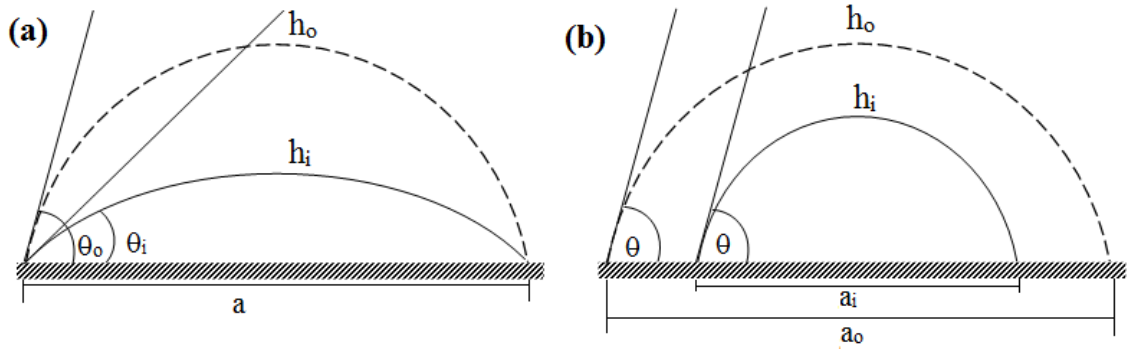


**Figure 1.5.** (a) A liquid droplet evaporating in constant contact-area mode. (b) A liquid droplet evaporating in constant contact-angle mode.

## 1.1.4 Evaporation model

For microdroplet, the evaporation model is within the continuum mechanics regime where the droplet assumes the shape of as a spherical cap. One of the most widely used model for evaporation of droplet is "constant area" model described by the Deegan *et al.* (1997) which was later modified by Popov (2005). In this model, the contact line of the droplet is assumed to be pinned throughout the process. The contact angle and height of the droplet decrease with time. The parameters describing the problems are illustrated in Figure 1.6. To determine the evaporation rate, the height of the droplet must be determined as a function of time. Assuming the shape of the drop as a spherical cap, the height of the droplet h(r, t) can be expressed as

$$h(r,t) = \sqrt{\frac{R^2}{sin^2\theta} - r^2} - \frac{R}{tan\theta(t)} \tag{1.11}$$

From eqn. 1.11, the volume of the droplet, $V_d$, can be expressed as

$$V_d(t) = \int_r^R h(r,t) 2\pi r dr \tag{1.12}$$

$$V_d(t) = \frac{\pi R^3}{3sin^3\theta(t)}(1 - cos\theta(t))^2(2 + cos\theta(t)) \tag{1.13}$$

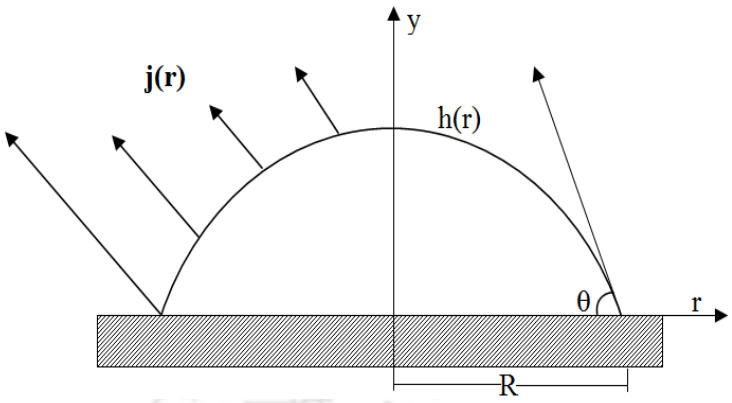


**Figure 1.6.** Evaporation of droplet placed on the substrate.

## 1.1.5 Evaporation rate

At the droplet interface, the evaporation flux is expressed by

$$J(r,t) = D_V \nabla c \tag{1.14}$$

where $D_V$ is the vapor diffusivity and $\nabla c$ is the gradient in vapor concentration.

For relatively flat droplet, the evaporation flux along the droplet free surface can be well approximated by the simple form given by (Deegan *et al.*, 2000),

$$J(r,t) = J_o(\theta)\left(1 - \left(\frac{r}{R}\right)^2\right)^{-\lambda(\theta)} \tag{1.15}$$

where $\lambda(\theta) = ½ - \pi/\theta$ with $\theta$ in radian.

Following the approximation of Hu and Larson (2006), the evaporation rate can be expressed as,

$$J_o(\theta) = \frac{C_v\,(1-H)}{R}\left(\frac{(8\pi-4)\left(\theta-\frac{\pi}{2}\right)^2}{\pi^3} + 1\right) \tag{1.16}$$

where H is the relative humidity, R is the radius of the droplet (mm) and $C_v$ is the vapor concentration, mol/mm$^3$.

### 1.1.6 Heat flux through the interface of the droplet

In the region r/R << 1, the radial heat flux can be neglected in a small droplet compared to the axial one. Therefore, the heat flux is perpendicular to the surface of the substrate i.e. the heat transfer can be considered as 1D. Thus, the heat due to conduction ($Q_{cond}$) can be expressed as

$$Q_{cond} = \frac{k_s(T_o - T_{SL}(r))}{h_s} = \frac{k_L(T_{SL}(r) - T_i(r))}{h_r} \tag{1.23}$$

where $h_s$ is the substrate thickness; $h_r$ is the height of the droplet, $T_o$ is the ambient temperature (K); $T_{SL}$ and $T_i$ are the temperature at the solid-liquid interface and liquid-vapor interface respectively. The heat fluxes due to conduction and evaporation at the droplet interface are balanced (Xu *et al.*, 2010). Therefore,

$$Q_{cond} = Q_{evap} = HJ_o\left(1 - \frac{r^2}{R^2}\right)^{-\lambda}\left(1 + \left(\frac{dh}{dr}\right)^2\right)^{1/2} \tag{1.24}$$

The surface temperature can be expressed as

$$T_i(r) = T_o H\left(1 - \frac{r^2}{R^2}\right)^{-\lambda}\left(1 - \frac{r^2 sin^2\theta}{R^2}\right)^{-1/2}\left(\sqrt{\frac{1}{sin^2\theta} - \frac{r^2}{R^2}} - \frac{1}{tan\theta} + K_R\right) \tag{1.25}$$

where H is the relative humidity and $K_R$ is the ratio of thermal conductivity of the substrate to the thermal conductivity of the liquid drop.

### 1.1.7 Internal fluid flow

In natural process, two types of fluid motion can exist within the evaporating droplet. One is the buoyancy dominant convection while the other is convection due to surface tension effect.

In buoyancy convection commonly known as Rayleigh convection, gravity is the driving force. If a liquid droplet placed on a wetting substrate is heated from bottom the

liquid density at the bottom becomes lighter than at the top. The system is not necessarily undergoes convective motion since viscosity and thermal diffusivity of the fluid try to prevent the convective motion. If the fluid is heated sufficiently large enough (higher temperature gradient across the layer), then only the system becomes unstable and convective motion is induced by the gravity from the region of low density region to high density region as shown in Figure 1.7a.

Earlier, it was not realized that the nonunifrom evaporation rate along the interface of the droplet can lead to a secondary convection involving gradients in the surface tension, which in general coexists with Rayleigh's buoyancy convection. This situation, now called Benard-Marangoni convection. Lu *et al.* (2011) have shown by numerical simulations that the Marangoni convection dominates over the natural convection inside the small droplet placed on the heated surface. Gradients in the surface tension cause surface tension forces away from the warmer spot. These forces drive flows from the region of lower surface tension to higher surface tension region as shown in Figure 1.7b. This instability does not involve gravity, so may be expected even under zero-gravity conditions.

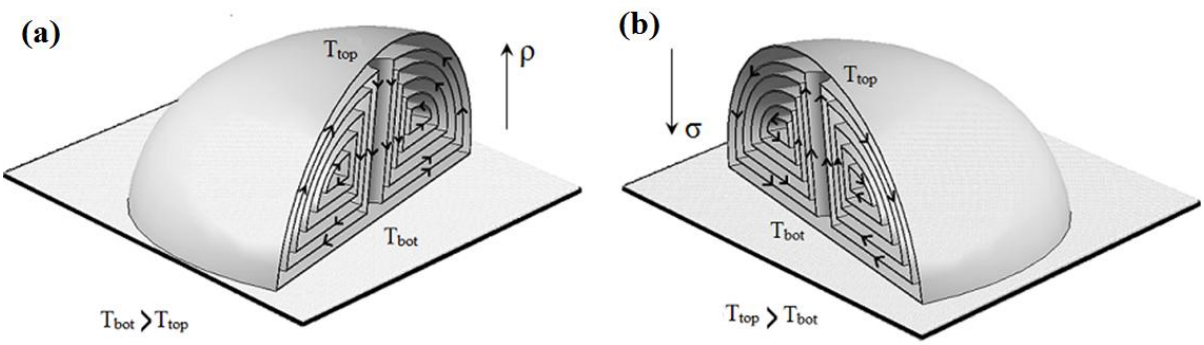


**Figure 1.7.** Schematic diagram of convection cells inside the evaporating droplet. (a) Rayleigh convection cells; (b) Marangoni convection. $T_{bot}$ and $T_{top}$ are the temperature at the bottom surface and top free surface.

## 1.1.8 Dimensionless numbers

As already discussed in the previous section, Marangoni stress driven and buoyancy driven convection are expected to influence the internal fluid motion inside the evaporating droplet. Since the size of the droplet is very small, the buoyancy driven convection is expected to be low. However, the relative strength of these two needs to be ascertained. Three important dimensionless numbers are used to characterize the natural convection and Marangoni convection inside the evaporating droplet.

### 1.1.8.1 Grahshoff number

In natural convection, an important dimensionless number is the Grahshoff number (Gr). It is defined as the ratio of buoyancy force to viscous force,

$$G_r = \frac{\beta g R^3 \Delta T}{\vartheta^2} \tag{1.26}$$

where β is the volume expansion coefficient of the liquid, R is the radius of the droplet, ΔT is the temperature difference between substrate and droplet surface and ϑ is the kinematic viscosity. The natural convection can be ignored when the Gr value is less than 2400 (Holman 2002).

### 1.1.8.2 Marangoni number

Marangoni convection occurs when the surface tension of an interface (generally liquid-air) depends on the temperature. It is to be noted that Marangoni stress can also develop due to variation of surfactant concentration on the surface. In the case of temperature dependence, the Marangoni convection is also called thermo-capillary convection. The Marangoni number may be regarded as the ratio of surface tension forces and viscous

forces. The dimensionless number that is used to describe the importance of Marangoni convection is defined as:

$$\mathbf{M_a} = \frac{\Delta T}{\alpha \mu}\frac{d\sigma}{dT} \tag{1.27}$$

where 'α' is the thermal diffusivity and ΔT is the temperature difference between substrate and droplet surface. dσ/dT is the rate of change of surface tension with temperature. Marangoni convection can be neglected when Ma is less than 100 (Carey 1992).

#### 1.1.8.3 Bond number

The strength of Marangoni convection inside the evaporating droplet can be further determined by another dimensionless number called Bond number. This can be defined as the ratio of gravitational forces to the surface tension. Bond number ($B_o$ ) is given by

$$B_o = \frac{\beta g \vartheta^2}{\frac{d\sigma}{dT}} \tag{1.28}$$

when Bo << 1, Marangoni convection is dominant over the natural convection and when $B_o$ >> 1, the natural convection is dominant inside the evaporating droplet.

## 1.1.9 Coffee ring stain

Self-assembly of dispersed particles in evaporating droplet on a wetting surface leads to interesting pattern formation in the dried residue. Such self-organizing characteristic indicates the multistate scale transport phenomenon occurring within the evaporation drops. Although the process is very simple, the physics is very complicated but relevant to various industrial and biological applications. The complex fluid motion, particle transport and self-assemble of dispersed particle make a rich fundamental system for scientific research of interest.

Particles in an evaporating droplet often leave ring-like pattern on the underlying substrate after complete evaporation. Deegan *et al.* (1997) were the first to explain the capillary flow as the underlying mechanism of ring formation in a drying drop, more commonly known as '*coffee ring effect'* as shown in Figure 1.8. The phenomenon is not specific to coffee drop but it can happen to any drops of colloidal suspensions, biological and DNA suspensions. Control of this phenomenon is critical in many applications such as paint manufacturing; electronic circuits and ink-jet printing where uniform distribution of particles on the substrate is required. The phenomenon is more promising when it comes to microfluidics involved in DNA microarray and protein arrays (Vincent *et al.* 2005; Fang *et al.* 2006; Jing *et al.* 1980). This has attracted many researchers with the objective to understand the basic physical events behind the coffee ring formation.

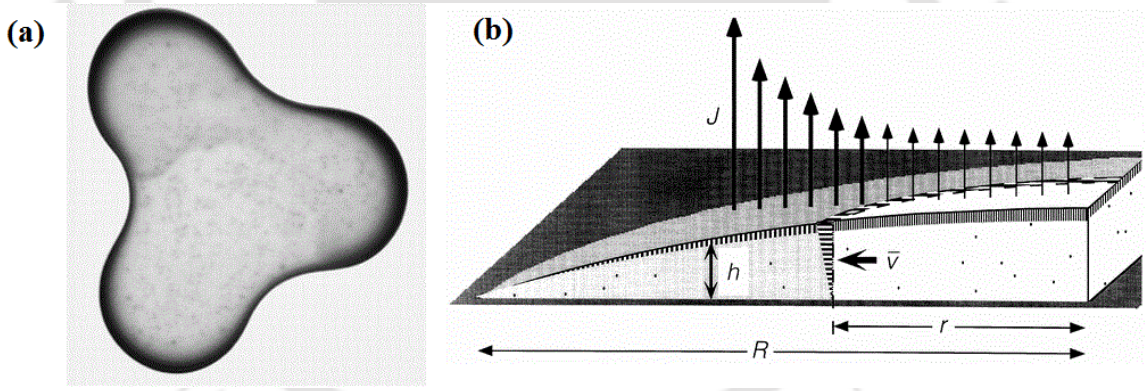


**Figure 1.8.** (a) Image of the coffee ring pattern. (b) Mechanism of outward flow during evaporation. (From Deegan *et al*. 1997, *Nature* **389**, 827-829. Copyright 1997 by the Nature Publishing Group)

Recently interest has emerge in understanding the deposition patterns of drying drop of biological fluids for the development of inexpensive disease diagnostic techniques. Drying drop of biological fluids reveals uniqueness in pattern formation that reflects the health of the person and this can be used for characterization of the blood

sample and as potential marker for disease diagnosis (Burtin *et al.* 2010; Sefiane *et al.* 2010). This confirms the importance of physiochemical properties of biological fluids in addition to the mechanisms of particle transport in pattern formation. Even though many mechanisms were framed to explain this phenomenon, a complete understanding on the coffee drop effect is far from reality. The proposed work is to understand the internal fluid flow pattern, particle transport and subsequent particle deposition pattern of an evaporating droplet of polystyrene particles as well as biological matter. The results may provide better way to understand the underlying mechanism in coffee ring effect and is expected to contribute significantly in the development of low cost disease diagnostic techniques.

## 1.2 Review of the literature

Research interest on formation of coffee ring structure is increasing due to the various research applications and relevance to many scientific fields. In this section, a relevant literature survey on various aspects of particle deposition pattern of an evaporating droplet including general pattern formation and internal fluid flow of the evaporating droplet is discussed. Finally, a review on various techniques available to visualize the internal fluid flow in an evaporating droplet is also discussed.

### 1.2.1 General pattern formation and dynamics of the evaporating droplet

A systematic study on formation of ring like deposition pattern of drying droplet of colloidal suspension was first started by Deegan *et al.* (1997, 1998, 2000, 2000a). They have explained the underlying mechanisms involved in the coffee ring formation. Using flow visualization with polystyrene particles in water droplet, they showed that nonuniform evaporation along the droplet interface induced capillary flow which

transported solute to the contact line, where evaporation is maximum. The particles accumulated near the contact line, which was pinned throughout the evaporation process. Subsequent to these findings there are many studies reporting the application of "*coffee ring effect*" in evaporation induced self-assembly of particles (Jing *et al.*, 1980; Leng, 2010; Marin *et al.*, 2011; Vincent *et al.*, 2005). On the other hand, the formation of ring like structure can be troublesome in many applications such as ink-jet printing (Soltman and Subramanian, 2008), electrowetting (Eral *et al.*, 2011; Ko *et al.* 2008), paint manufacturing (Xu *et al.*, 2007), DNA microarray (Jing *et al.*, 1980; Marin *et al.*, 2011; Vincent *et al.* 2005), etc. This unique phenomenon has also showed the potential to develop inexpensive medical test devices (Burtin *et al.*, 2011; Trantum *et al.*, 2012, 2013, 2014; Wong *et al.* 2011). Several studies have also explored the control of the coffee ring structure such as the use of ellipsoidal particles (Yunker *et al.*, 2011), nature of the substrate (Petsi *et al*. 2010; Wen *et al.*, 2013), addition of surfactants (Hu and Larson 2005) and chromatographic and filtration effects (Nilghaz *et al.*, 2015). This has necessitated the goal of understanding the underlying flow phenomenon inside an evaporating droplet.

Several groups proposed theoretical models for the velocity field drop and the resulting final deposition. A model by Fischer (2002) considered a colloidal sessile drop in several different modes of evaporation including an open system, one in which evaporation was greatest at the center of the droplet. By modeling flow profile inside the droplet, it was verified that the solute was distributed at the periphery for the open system. When the evaporation was maximum at the center, the solute was distributed uniformly on the substrate with no ring formation. Popov (2005) have studied the velocity field theoretically by considering a very thin drop and derived the expressions for height averaged radial velocity profile inside the drop. Adachi *et al.* (1995) have observed the

'stick slip' motion of the contact line and reported that there is a competition between the friction force and surface tension which generates a stripped film composed of particles on complete drying. Ristenpart *et al.* (2007) argued that for organic liquids, non-uniform evaporation along the surface induces variation in temperature along the droplet interface and these variations create a thermo-capillary flow inside the droplets. Widjaja and Harris (2008) performed numerical simulations to study the deposition pattern in evaporating droplets containing solute particles. They found that the convection and diffusion mass transfer of the particle in the bulk liquid influences the deposition rate on the substrate. They also did not consider the role of Marangoni flow in evaporating droplets.

A technique was developed to regulate the particle deposition by manipulating the contact line, the evaporation flux, shape of the particles, size of the particles, particle-particles interaction, particle-substrate interaction etc. (Bhardwaj et al., 2010; Shen et al. 2010; Yunker et al., 2011). Yunker *et al.* (2011) observed that the particle deposition pattern on the substrate is strongly influenced by the shape of the particle. They have shown through experiment that the ellipsoidal particles left uniform distribution on the substrate whereas spherical particle showed a ring like deposition upon complete evaporation as shown in Figure 1.9. They predicted that the particles with high aspect ratio collects at the interface forming a loosely packed network and resist the convection causing coffee ring pattern whereas spherical particles exhibit coffee ring formation. They additionally reported that the particles with high aspect ratio can be used in paint manufacturing, ink-jet printing and other applications so the standard of the coating may be improved with considerable reduction in price. Bhardwaj *et al.* (2010) have shown that the pH scale of the droplet induces the Derjaguin-Landau-Verwey-Overbeek (DLVO) forces that prevent the ring like deposition pattern to a homogenous pattern. They proposed

a phase diagram to describe the shape of the deposition pattern. This is based on three modes of fluid motion related to final deposition pattern such as a capillary flow, Marangoni flow and fluid flow driven by the DLVO interactions.

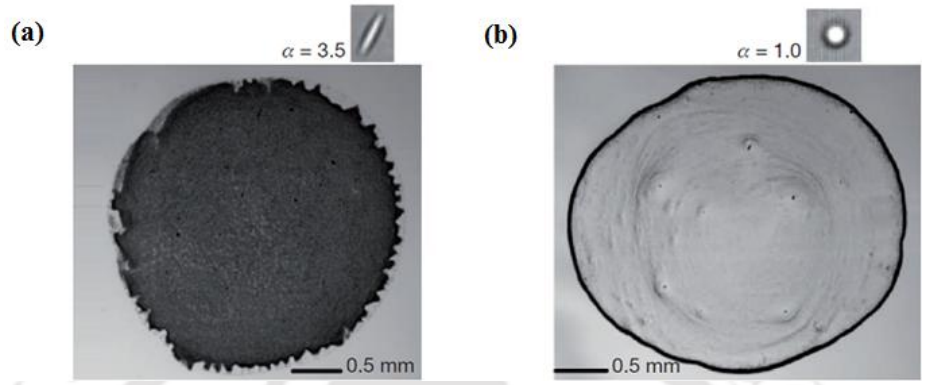


**Figure 1.9.** Photograph of the deposition pattern: (a) Ellipsoidal particles, (b) spherical particles. (From Yunker *et al.* 2011, *Nature* **476**, 308-311, 2011. Copyright 2011 by the Nature Publishing Group).

Droplet of nanoparticles or colloidal suspension also shows a self-assembly of particle deposition pattern upon complete evaporation. Understanding such morphology of self-assembled particle deposition pattern will enhance the potential to develop high throughput technologies from ink-jet printing to drug screening. Xu *et al.* (2007) have shown that nanoparticles can be self-assembled by allowing a solution of nanoparticles to evaporate on a sphere-on-flat geometry. This self-assembly of particles on a substrate is of great importance in many micro level applications. It is a great challenge to control this phenomenon in small droplets. Majumder *et al.* (2012) found that the phenomenon of evaporating droplet can be used for depositing catalyst nanoparticles to form a single walled carbon tubes as well as to manufacture plasmonic films of well-spaced, un-aggregated gold nanoparticles. Lebedev-Stepanov *et al.* (2013) additionally found that ring like pattern formation is the self-assembly of the particles that give coherent patterns of reasonably well-defined morphology. Hong *et al.* (2007, 2009) were able to get order

polymer pattern of concentric rings and punch-like form by interacting the polymer and the substrate. Marin *et al.* (2011) observed the ordered particles arrangement at the early stage while disordered arrangement were observed at the end of the evaporation of droplet.

To understand the role of fluid motion on particle depositions there have been some studies to map the velocity field. Hu and Larson (2006) using the lubrication analysis of fluid flow studied the effect of Marangoni flow inside the evaporating droplets through finite element simulations. They observed that the ring like deposition pattern is not only due to the pinning of contact line but Marangoni stress driven flow also has strong influence on particle deposition. Their experimental results indicate that the particle deposition in octane droplet can be localized predominantly at the center instead at the edge of the contact line. They believed that a nonuniformity of temperature of the surfaces leads to difference in surface tension on the interface, which induces thermal Marangoni flow (See Figure 1.10). This makes the fluid near the edges rise towards the top of the droplet and plunge downward to the center of the droplet. They observed qualitative agreement of experimental and simulation results for deposition pattern. The particle concentration profile showed a large peak at the edges of the water droplet when Marangoni flow was weak or absent. When the Marangoni flow was strong, a large peak was observed at the center of octane droplet. They also reported the role of surfactant on Marangoni flow.

Zhang and Wang (1982) observed the Marangoni flow and natural convection in an evaporating droplet. Savino and Monti (1996) and Savino *et al.* (2002) have experimentally shown the existence of Marangoni flow in droplets of organic fluid but not in case of water droplet. David *et al.* (2007) investigated experimentally the role of thermal conductivities of the substrate on the evaporation of water droplet. Girard *et al.* (2008)

measured the temperature profile inside a water droplet place on heated substrate by infrared camera and observed that the temperature gradient within the evaporating droplet was less than 1$^{o}$C. A temperature difference as small as 0.5$^{o}$C within the droplet is enough to generate the Marangoni flow inside the evaporating droplet. Lu *et al.* (2011) found numerically that the Marangoni convection is dominant over the natural convection inside the droplet placed on the heated surface.

Although typically neglected, many studies have focused on the influence of gravity on pattern formation. Sommer (2005) studied the impact of gravity on droplet of nanosphere suspension and found that the consequences of gravity are negligible once the diameter of droplet of nanosphere suspensions was less than 10 µm. Most of the literatures neglected the consequences of gravity because of the small size of the droplet, the particles and small bond number. Separation of both Marangoni and buoyancy effects can be achieved only at zero gravity condition.

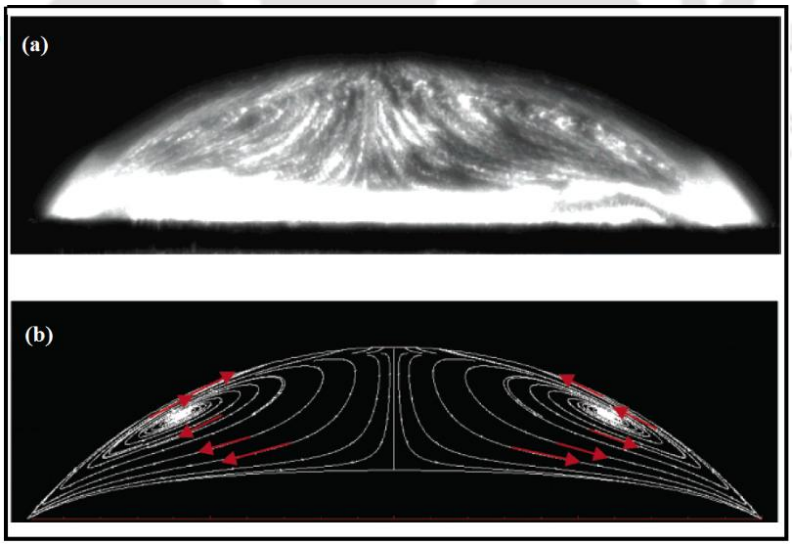


**Figure 1.10.** Marangoni flow inside the evaporating octane droplet, (a) imaged experimentally and (b) predicted (Ma=45000). (From Hu and Larson 2006, *J. Phys. Chem. B.* **110**, 7090–7094. Copyright 2006 by the American Chemical Society).

## 1.2.2 Drying pattern

When the liquid droplet is pinned during evaporation, solute particles generally accumulated in ring like pattern due to 'coffee ring effect'. Formation of ring structure has been demonstrated in various system and uniform deposition is often preferred in applications such as paint industry and inkjet printing. This pattern formation in evaporating droplet can be influenced by wetting properties, fluid motion, heat and mass transfer etc. In this section, various deposition patterns and physical mechanisms in an evaporating droplet are discussed.

### 1.2.2.1 Ring like stain

Deegan et al. (1997) theoretically predicted the velocity field, the growth rate of the ring and particles distribution inside the droplet. Later, Hu and Larson (2006) showed that only the pinning of contact line and continuous evaporation of solvents were not enough for coffee ring formation, but the Marangoni flow should be suppressed. Based on the experiments on organic fluids, they found that the stains were left at the center of the droplet, as a result of a convection driven by the Marangoni stress arising from the non-uniform evaporation along the droplet interface. Therefore, to ensure the production of coffee-ring stains, the Marangoni flow should be reduced. Another factor that may determine the formation of a coffee ring is the droplet size. Shen *et al.* (2010) determined the minimum size of the coffee ring formation with three different diameters of polystyrene particles (i.e. 20 nm, 60 nm and 100 nm). The particle deposition from the small droplet (diameter less than ~10 μm) failed to show any coffee ring like structure as shown in Figure 1.11. A minimum diameter of the droplet was found to exist for coffee ring like pattern at this scale. This is often due to the increased rate of evaporation when compared to the rate of particle diffusion.

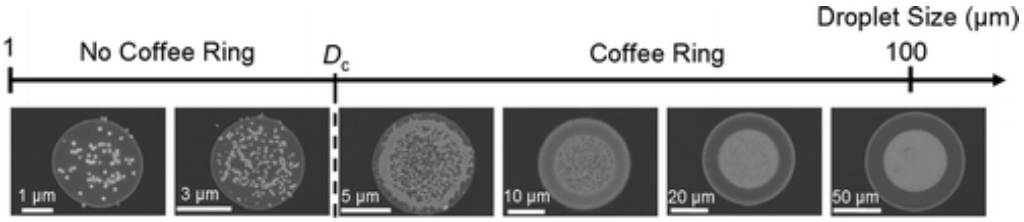


**Figure 1.11.** Different nanoparticle deposits on hydrophilic Platinium substrate with diameters ranging from 3 to 100 μm. (From Shen *et al.*, 2010, *J. Phys. Chem. B.* **114**, 5269–5274. Copyright 2010 by the American Chemical Society).

### 1.2.2.2 Uniform pattern

As discussed above, the external conditions, interior flows including the capillary flow and Marangoni flow, and the particle–particle interactions determine the deposition patterns. These factors might compete with each other to produce the final deposition patterns. Bigioni *et al.* (2006) demonstrated that the particle deposition pattern can be controlled by the evaporation kinetics and the particle interactions with the liquid–gas interface. After the evaporation, a uniform distribution of latex spheres was generated by an induced "Wenzel state" resulting from a porous gel foot formed by the spheres at the rim of the droplet (Cui *et al.* 2012). Moreover, with the help of an attractive particle–interface interaction, a rapid early stage evaporation dynamically produced a two-dimensional (2D) assembly of nanoparticles at the liquid–gas interface.

### 1.2.2.3 Stick-slip pattern

A liquid droplet placed on a non-perfect homogenous surface, the dynamics of the contact line showed the stick–slip behavior. Several rings with one another are left on the solid surface after complete evaporation as shown in Figure 1.12 (Moffat *et al.*, 2009). However, for the pure ethanol droplet, it behaved like a continuously receding contact line at a constant contact angle. Accumulation of particles near the contact line enhances the stick-

slip behavior of the liquid droplet. The hysteretic energy barriers that were close to the line tension induced the "slip" behavior. Once the depinning force surpassed the hysteretic energy barrier, the pinned contact line was unable to maintain on the solid surface but to recede back. An unexpected phenomenon of the three-phase line drift was observed, named as "pseudo-pinning." It may have resulted from the small scale pinning of the local contact line by the deposited particles, or by the increased viscosity due to intense accumulation of the nanoparticles (Moffat *et al.*, 2009**;** Orejon *et al.* 2011**;** Moffat and Sefaine, 2009a).

In order to explain this oscillatory motion, Adachi *et al.* (1995) built a mathematical model from which the mechanism of the stripe-stain formation was obtained. It was indicated that the contact line bore a friction force when the particles transported from the center to the edge of the droplet. Due to the competition between the friction force and surface tensions near the contact line, the contact line of the droplet oscillated during evaporation which result a striped film composed of particles. Therefore, no matter if the contact line was pinned or depinned, the forces acting on it determined its behavior to a great extent.

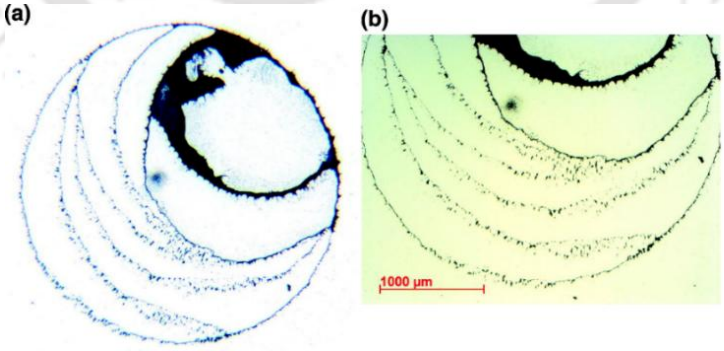


**Figure 1.12.** Stick slip pattern after complete evaporation of ethanol drop containing $TiO_2$ nanoparticles. (From Moffat *et al.*, 2009, *J. Phys. Chem. B.* **113**, 8860. Copyright 2009 by the American Chemical Society).

### 1.2.2.4 Fingering pattern

Deposition pattern like fingering structure is induced by the instability occurring at the contact line with a dewetting behavior. The structure instability was early proved to depend on the capillary flow, Marangoni effect and some other external forces like gravity and centrifugal forces (Pauliac-Vaujour *et al.*, 2008; Cazabat et al. 1990). Weon and Je (2013) showed that a fingering structure emerges in the coffee ring from the droplet containing bidispersed particles. Both symmetric and asymmetric structures were observed after complete evaporation of nanofluid droplet (Crevoi and Duan, 2013) as shown in Figure 1.13. The occurrence of asymmetric fingering structure was thought to have resulted from the uneven distribution of the evaporation rate along the droplet free surface or the dynamic of the contact line of the droplet.

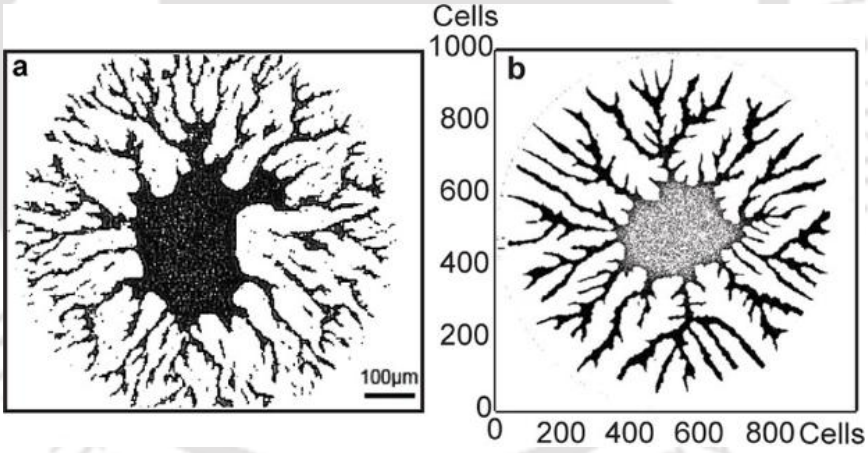


**Figure 1.13.** Fingering structure pattern from copper nanofluid droplets (a) symmetric (b) asymmetric. (From Crevoi and Duan, 2013, *J Phys. Chem C* **117,** 7835. Copyright 2013 American chemical Scociety).

## 1.2.3 Factors affecting dried pattern

As mentioned above, the deposition patterns are strongly affected by the dynamic of the contact line. Besides, the particle deposition is also strongly affected by internal fluid flow pattern as well as forces acting on the dispersed particles. Three most commonly observed

deposit patterns are coffee-ring pattern, a uniform distribution, and center spot like pattern. The earlier theoretical models assuming the potential flow inside an evaporating droplet predicted velocity vectors going from the center of the drop, parallel to the flat substrate, towards the edge as shown in Figure 1.14a. Figure 1.14b shows schematic of evaporating sessile droplet and various forces acting on the suspended particles. Deegan *et al.* (1997) argued that the evaporation rate near the edge of the droplet is much higher than that at the center, leading to more loss of solvent at the edge compared to the center. The capillary forces caused by the flow from the droplet center toward the edge (to compensate for solvent loss since the contact line is pinned) will create a force ($F_2$) on the particle. The force of attraction between the suspended particle and substrate ($F_1$) can impede the motion of the particle towards the edge (Sommer and Rozlosnik 2005). $F_3$ denotes the force due to secondary flow in the droplet. The vertical temperature gradient ($\Delta T$) can cause buoyancy driven convection. Due to unequal evaporation fluxes ($J_r$) at the droplet surface the temperature and surface tension at the apex ($T_a$, $\sigma_a$) and edge ($T_e$, $\sigma_e$) would be different. The resulting surface tension gradient would create Marangoni convection whose direction can be either wise depending on the direction of temperature gradient. In the absence of Benard-Marangoni instability, axisymmetric flow can be observed (Ristenpart *et al.* 2007). The axisymmetric nature of the flow allows the study in a vertical 2D plane passing through the center of the drop. By including the Marangoni stresses in the lubrication solution Hu and Larson (2006) predicted strong Marangoni flow for evaporating water droplets. The experimental observation of Deegan *et al.* (1997) and Hu and Larson (2006) showed weak Marangoni flow for water droplet. Hu and Larson (2006) attributed this to presence of contaminants on the free surface. The direction of Marangoni convection cells observed in their experiments and simulations was such that it reversed the coffee-ring phenomenon producing spot like deposition at the droplet center.

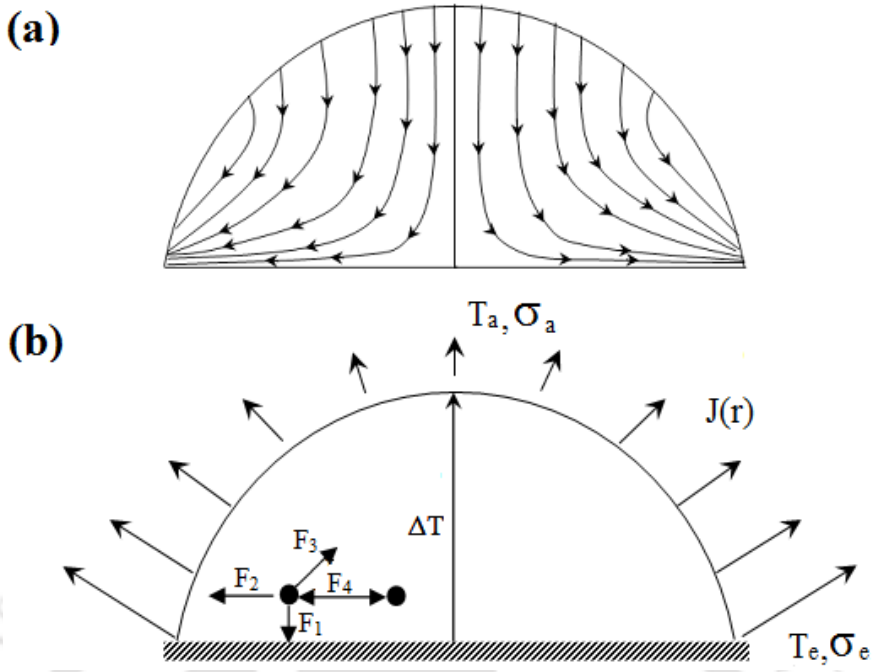


**Figure 1.14.** (a) Schematic diagram of Capillary fluid flow. (b) Various forces on a particle inside the evaporating droplet.

### 1.2.4 Surface temperature distribution

During the evaporation process, non-uniform temperature distribution along the droplet interface generates a Marangoni convection inside the evaporating droplet. Marangoni flow significantly affects the flow field and the particle deposition pattern. The temperature distribution within the droplet depends on both the conduction of heat within the droplet and the conduction of heat to the droplet from the underlying substrate. If the thermal conductivity of the substrate ($k_s$) is higher than the thermal conductivity of the liquid drop ($k_L$), then the droplet base in contact with the substrate will be isothermal. On the other hand, if $k_s$ is small then the liquid will be nonisothermal along the base of the droplet (Larson, 2014). A reduced value of substrate thermal conductivity will lower the overall temperature in the droplet as well as temperature gradient along the droplet interface (Ristempart *et al.*, 2007; Xu et al., 2010). Ritsenpart *et al.* (2007) using

asymptotic analyses have shown that the direction of circulation depends on both the contact angle and ratio of the thermal conductivities of the substrate and liquid ($K_R$). They have shown that for $K_R > 2$ the Marangoni flow is directed radially outward along the substrate whereas for $1.45 < K_R < 2$, the flow direction depends on the value of contact angle, and for $K_R < 1.45$ the circulation direction is radially inward along the substrate as shown in Figure 1.15. This theory is formulated only for substrate with infinite thickness. For the case of finite substrate thickness, where the bottom of the substrate temperature can be assumed to be at ambient temperature, a dimensionless number ($R_N$) can be defined that control the temperature distribution along the droplet free surface. $R_N$ can be defined as the ratio of thermal resistance of the substrate to the thermal resistance of the liquid droplet. The total temperature difference between the top of the droplet and the bottom of the substrate is estimated as $\Delta T_{tot} = \Delta T + \Delta T_s$ where $\Delta T$ is the temperature drop across the height of the droplet and $\Delta T_s$ is the drop across the finite thickness of the substrate. The overall temperature different can be written as (Larson 2014),

$$\Delta T_{tot} = \frac{2\,\Delta H_{vap}\,D_{vap}\,\rho_{vap}\,h_o}{k_L\,R}(1 + R_N) \qquad (1.29)$$

where, $H_{vap}$ is the heat of vaporization per unit of mass (kJ/kg), *Dvap* is the diffusivity of water vapor ($m^2/s$), $\rho_{vap}$ is the mass density of vapor ($kg/m^3$), $h_o$ is the height of the droplet (cm), $k_L$ is the thermal conductivity of the liquid, R is the radius of the droplet, $h_s$ is the thickness of the substrate (cm) and $R_N = \frac{k_L h_s}{k_s h_o}$.

If $R_N \gg 1$, then the eqn. (1.29) becomes

$$\Delta T_{tot} = \frac{2\,\Delta H_{vap}\,D_{vap}\,\rho_{vap}\,h_o}{k_L\,R} \qquad (1.30)$$

When the thermal resistance in the substrate is greater than that in the droplet, it dominates the droplet temperature. In such a situation, the lowest droplet temperature is at

the contact line, where evaporation is fastest, rather than at the top of the droplet, where the droplet height is maximum, but the evaporation rate is the lowest. Xu *et al.* (2010) predicted that the temperature distribution not only depends on the relative thermal conductivity of the substrate and liquid but also the ratio of the substrate thickness to the contact angle of the droplet. They have neglected heat convection and proposed the following condition for lowest temperature to be at the contact line: $R_N = [\sin 2\theta - 4\lambda \tan(\theta/2)]/ (4\lambda + 2\sin^2\theta)$. For small contact angles, this condition is well approximated by $R_N > 1$. For large contact angles, greater than 45°, increasing the contact angle further decreases the value of the $R_N$ needed to drive the coldest temperature to the contact line, and thereby reverse the Marangoni flow.

The criterion for direction of surface temperature can be more understood from the Figure 1.15b. David *et al.* (2007) have shown experimentally that uniform evaporation rate along the droplet free surface increases with the thermal conductivity of the substrate. Recently, Zhang *et al.* (2014) have shown through numerical simulation that uniform surface temperature distribution for all the conditions of evaporation is not reasonable and a non-monotonic surface temperature profile may exist during the transition period i.e. when the contact angle is near to the critical value as shown in Figure 1.16. They reported that the surface temperature distribution can be defined by two factors i.e. non-uniform evaporation rate along the droplet free surface and another one is non-uniform conduction path from the substrate to the droplet free surface. The surface temperature due to conduction path may be predominant over the evaporative cooling when the contact line of the droplet is large, whereas the surface temperature due to evaporation cooling is dominant when the contact angle reduces and the influence of conduction path and evaporative cooling are comparable during the transition period of the evaporating droplet.

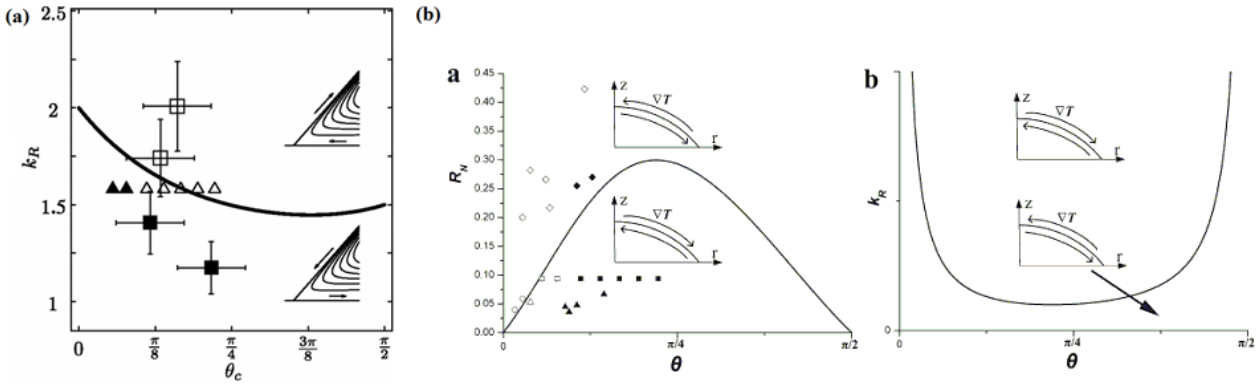


**Figure 1.15.** (a) Surface temperature gradient near the contact line of an evaporating droplet. (From Ristenpart *et al.* 2007, *Phys. Rev. Lett*. **99**, 234502. Copyright 2007 by the American Physical Society). (b) The temperature distribution relative to thermal conductivity as well as the contact angle of the droplet. (From Xu *et al.* 2010, *Langmuir* **26**, 1918-1922. Copyright 2013 by the American Chemical Society).

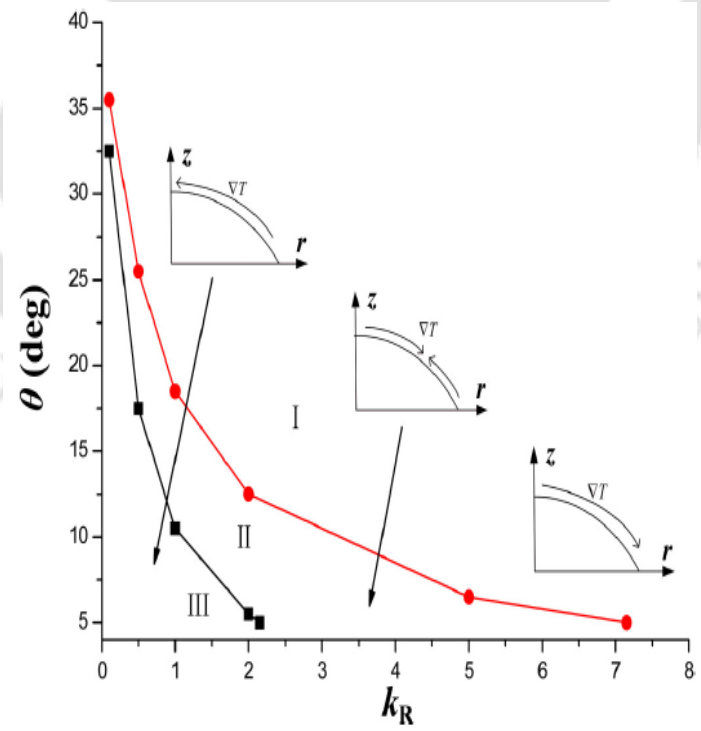


**Figure 1.16.** Phase diagram of the temperature distribution along the interface of an evaporating droplet. (From Zhang *et al.* 2014, *Phys. Rev. E.* **89**, 032404. Copyright 2014 by the AIP Publishing LLC).

### 1.2.5 Flow visualization of evaporating droplet

Only few studies have investigated the role of internal fluid flow on particle deposition in an evaporating droplet. Quantitative visualization of internal fluid flow in the evaporating drop provides clear picture of the particle transportation during the evaporation process. Therefore, it is necessary to have the correct mapping of fluid flow within the evaporating drop to control the particle transport. Savino and Monti (1996) solved the steady state flow field within the evaporating drop at steady state by considering Marangoni stress on air-liquid interface. They also performed experiments to map the velocity field within the drop. However, their theoretical results were not consistent with the experimental results because of the wrong mapping of real velocity field in spherical cap drop. The spherical form of the drop caused it to act like a lens and because of the refraction of light the object plane and image plane was not identical as shown in Figure 1.17.

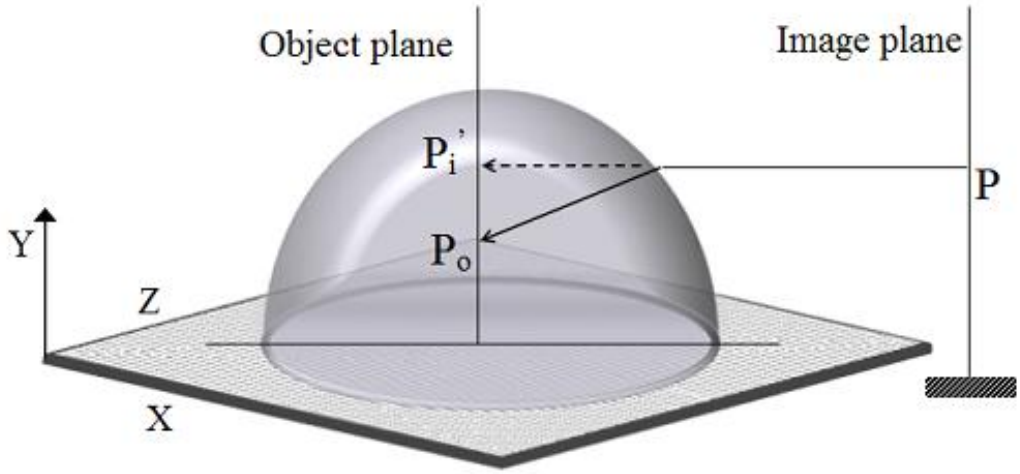


**Figure 1.17.** (a) Schematic diagram of lens effect in spherical liquid droplet.

Kang *et al.* (2007, 2011) have developed a velocity correction method based on the ray tracing method. Ray tracing is a method for presenting 3D images on 2D display by

tracing a path of light from the object place to image plane as shown in Figure 1.18a. The velocity correction method is divided into two methods. One is image mapping which use the mapped particles images for obtaining the velocity vectors by the PIV technique whereas the other one is called a velocity mapping method. However, the details of the velocity field near the free surface couldn't be captured because of image distortion caused by the refraction of the light as well as the curvature effect of the drop. This is more apparent from the image provided in Figure 1.18b. Ueno and Kochiya (1998) used 3D particle tracking method to analyze the capillary flow within the evaporating droplet.

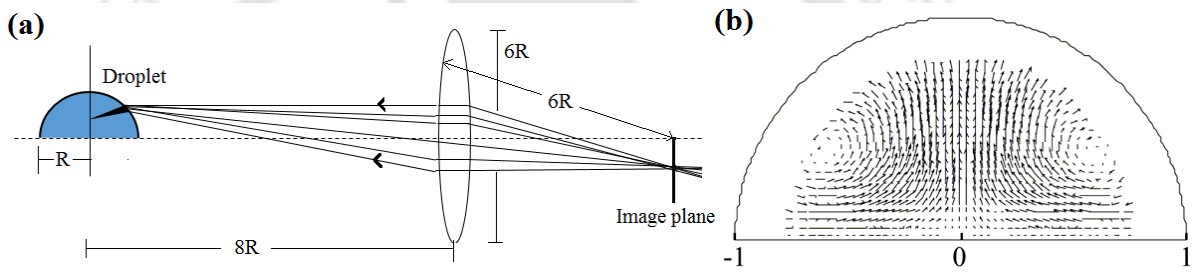


**Figure 1.18.** (a) Schematic diagram of Tracing of light ray from a point in a droplet (R is the radius of the droplet). (b) The measured velocity field by PIV technique inside the mixture of water-ethanol droplet. (From Kang *et al.* 2013, *Phys. Fluids* **25**, 042001. Copyright 2013 by the AIP Publishing LLC).

Pereira *et al.* (2007) used a 3D μ-DDPIV (micro Defocussing Digital Particle Image Velocimetry) to measure the flow field inside the evaporating droplet as shown in Figure 1.19. It is well known that diffraction and spherical aberration in microscopic imaging may cause distortion of defocussed particles. Therefore, they have used a micro target set-up over a plastic Petri dish to calibrate the defocussed particles in the images. The camera captured the defocussed particles located at different distance away from the focal plane. The target was moved in one direction starting from the reference plane, where

the defocussed particles will overlap, upto a point of maximum where detection is impossible.

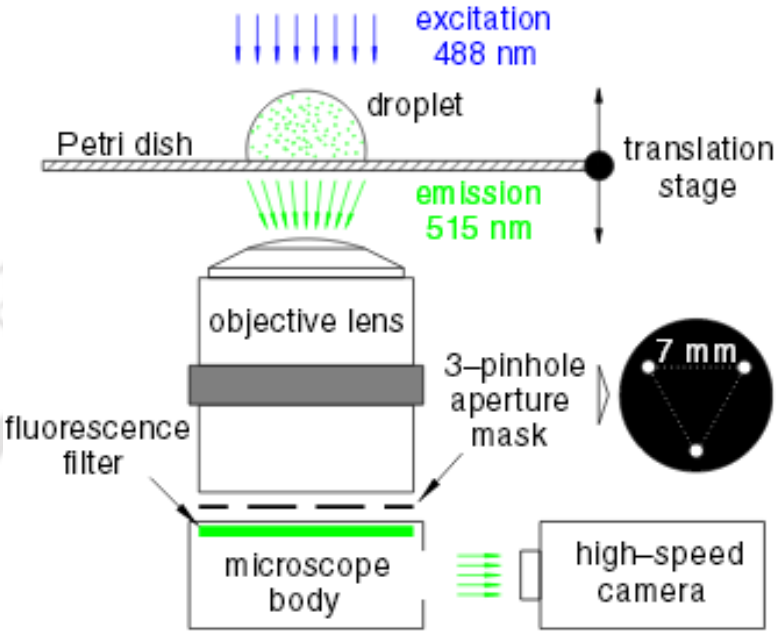


**Figure 1.19.** Schematic of the micro-DDPIV experimental setup. (From Perira *et al.* 2007, *Exp. Fluids* 42, 589–599, Copyright 2007 by the Springer).

Theoretically, as the rays pass through a convex lens not all of the refracted light can be captured by the camera perpendicular to the lens. In order to recover the lost information on the interface of the droplet, a tilt-angle method was proposed by He and Duan (2013). In this method, the camera is tilted vertically upward with an angle, α, to the axisymmetric centerline of the lens as shown in Figure 1.20. To restore the image for the temperature measurement of the droplet, Zhang and Melton (1994) applied similar method. However, for the different tilted angles, the results were found to vary. Numerical method for image recovery was developed on the basis of following assumptions: the diffraction effect is ignored since the wavelength of the illuminated laser is far smaller than the droplet size, the image deformation due to perspective view is negligible because

the magnification ratio of the camera lens is 1:1 and the droplet is considered to be axisymmetric. The loss of information on the top and right corner of the droplet interface is resulted from the limitation of the tilt-angle correction method. Only 95% of the velocity field information can be recovered due to the tilt view and the unsteady open evaporation condition.

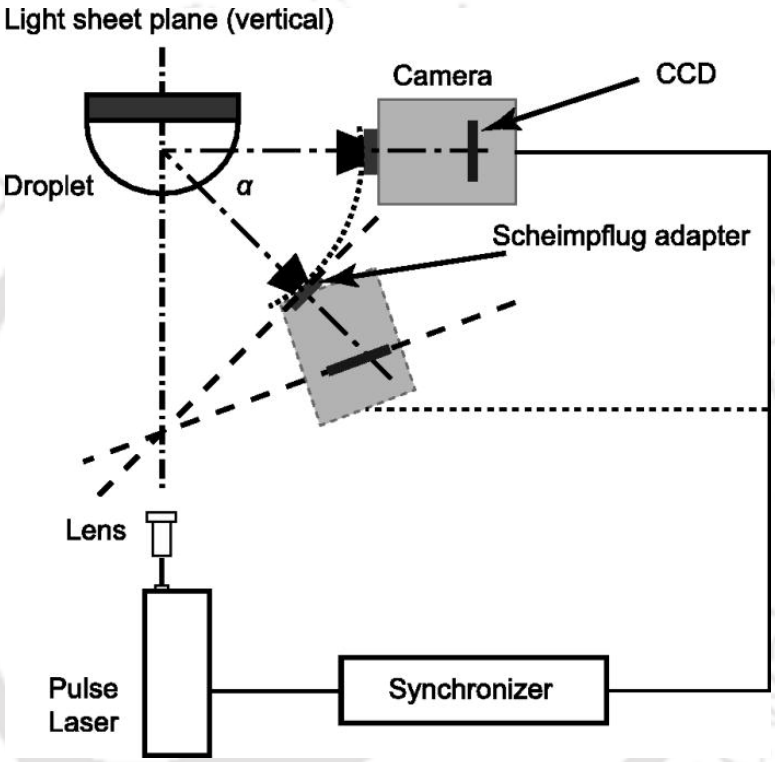


**Figure 1.20.** Schematics of the PIV system and the Scheimpflug principle when using the tilted camera to focus on the light sheet. (From He and Duan, 2013, *Appl. Phys. Lett.* **103**, 053508 Copyright 2013 by the AIP Publishing LLC).

Manukyan *et al.* (2013) visualized the interior fluid flow in polymer dispersion drop on hydrophilic and hydrophobic surfaces with spectral radar optical coherence tomography (SR-OCT). OCT is a non-invasive imaging technique based on an imaging Michelson interferometer. There are broadly speaking two types of OCT: Time-domain and Fourier-domain OCT. In a Time-domain OCT, axial structure is obtained by scanning

the reference mirror in the Michelson interferometer to change the reference path length. In a Fourier-domain instrument, the reference mirror is fixed but the interference fringes as a function of wavelength are obtained through a spectrometer and the axial structure is obtained through a Fourier transform (Drexler and Fugimoto, 2009). OCT was invented for in vivo imaging of the eye and most applications are found in the biomedical field, but recently it has also found applications in non-biomedical fields including the monitoring of the drying of thin films of various varnishes (Lawnman and Laing 2011; Stifter, 2007). Trantum *et al.* (2013) have used optical coherence tomography technique to see the internal fluid flow in 3D drop. To minimize the specular reflectance on the interface of the droplet, the OCT laser was adjusted to $9^{o}$ angle from the normal causing 10% error in particle co-ordinate data. In addition, the curvature of the droplet surface refracts the incident lasers causing lensing in OCT images. This manifest as slightly curved surface in the OCT visualization of 3D droplets like illumination, and refraction of light from the curve surface.

Several issues are encountered in visualization of flow field in the 3D evaporating droplet. There is no effective flow visualization technique available for 3D droplets. The conventional 3D experimental setups are expensive and various correlations are required to determine the velocity field. Recently Jaijus and Singh (2010) have developed an easy technique for 2D PIV measurement in an evaporating droplet. A confined 2D drop analogous to 3D drop is generated between two no-wetting transparent plates with narrow space. The drop rests on a rough wetting surface. The images are taken within the normal view of this plane. The dynamics of the drop was found to be comparable to the 3D drop. We have used this method to investigate internal motion and concentration dynamic of an evaporating droplet under various condition of evaporation.

## 1.3 Outline of the thesis

This PhD dissertation includes fundamental concepts of drying drops and detailed description of the research problems. In this study, we have highlighted that the coffee ring phenomenon can be controlled by various ways such as modifying the internal fluid flow pattern; controlling the dynamic of the contact line; using bacteria suspension displaying chemotaxis and changing the geometry of substrate.

In Chapter 1, the introduction of the subject and the motivation behind our studies is presented. A review of relevant literatures on evaporating droplet is also discussed. In Chapter-2, we investigate the internal fluid flow and particle transport in an evaporating droplet under various conditions of external heating of the substrate. The internal fluid flow and particles dynamics in evaporating droplet were determined by using the PIV technique. It also includes an explanation of experimental setup and methodology to determine the velocity fields as well as concentration dynamics inside the evaporating droplet. We have shown that the external heated substrate modifies the surface temperature gradient that generates the fluid flow inside the evaporating droplet. The surface temperature gradient is strongly influenced the Marangoni convection and finally affected the final deposition pattern. The Marangoni convection inside the evaporating is expected to be dominant over the buoyancy flow inside the microdroplet. The strength of Marangoni convection was investigated through experimental as well as numerical simulations. Analysis of dimensionless numbers was also performed to determine the strength Marangoni flow and results are presented in Chapter-2. We have also studied the evaporation of droplet with different concentration of solute particles and obtained detail information on the internal fluid motion is also discussed in Chapter-2.

In Chapter-3, we have extended the work to understand the effect of external heating of the droplet. The droplet free surface was heated by using thin wire heating element and the velocity filed and particles transport inside the evaporating droplet were studied. The contact line of the droplet subjected to external heating at the droplet interface was found to be unpinned during the process. Again, the nature of the deposition pattern was found to be strongly influenced by the dynamics of contact line of the droplet and these are discussed in Chapter-3. Most of studies reported that surface temperature gradient reverses at the critical angle of the droplet. In Chapter-4, the surface temperature profile and resulting fluid flow pattern during the transition period between the initial stage and final stage of the evaporation process are investigated through experimental and numerical simulation. The obtained results were presented in this Chapter-4.

The underlying mechanism of drying drops of biological suspension has been discussed in the Chapter 5. Flow visualization experiments using PIV were carried out with *E. coli* bacteria as biological tracer particles. Experiments were conducted for suspensions of motile (live) as well as non-motile (dead) bacteria. In the absence of any nutrient gradient like sugar on the substrate, both type of bacterial suspension showed two symmetric convection cells and a ring like deposition of particles after complete evaporation. Interestingly, the droplet containing live bacterial suspension showed a different velocity field when the sugar was placed at the base of the droplet. This can be attributed to the chemoattractant nature of the sugar which induced chemotaxis among live bacteria targeted towards the nutrient site. Deposition of the suspended bacteria was also displaced towards the nutrient site as the evaporation proceeded. The present experiments demonstrated that both velocity fields and concentration patterns can be altered by chemotaxis to modify the pattern formation in evaporating droplet containing live bacteria.

Evaporating droplet on a flat substrate is extensively studied. Less information are available on heat transfer, particle transport and internal fluid pattern inside the evaporating droplet placed on curved surface. In Chapter-6, we have investigated the evaporating droplet on curved surface. The surface temperature along the droplet interface was found to be strongly influenced by the structure of the substrate, which subsequently affects the internal fluid flow pattern, and finally suppressed the coffee ring stain. Finally, the main conclusion and overall impact of the work are discussed as well as opportunity for extending our research works are presented in Chapter-7.

# CHAPTER 2

# Microdroplet evaporation on heated substrate

## 2.1 Introduction

Most of the researchers believed that the coffee ring phenomenon is caused by the capillary flow from the bulk of the fluid toward the edges of the droplet. Subsequent studies by Hu and Larson (2005a, 2005b, 2006) showed that the Marangoni flow inside the drop can suppress the formation of the ring structure. Marangoni flow is generated by the surface tension gradient which induces Marangoni stresses. The surface tension gradient is caused by the non-uniform surface temperature distribution resulting from non-uniform rate of evaporation on the droplet surface. In the studies of Hu and Lasron (2005b, 2006) a strong Marangoni flow was observed in a droplet of organic solvent but not in the water droplet. They attributed the absence of Marangoni flow in case of water droplet to absorption of impurities on the droplet surface. Girard et al. (2006) measured the surface temperature of the evaporating droplet placed on a heated substrate by using an infrared camera and showed that a surface temperature difference as small as 0.5$^{o}$C was enough to generate Marangoni flow inside the drop. Savino et al. (2002) have reported that the internal fluid motion in an evaporating droplet can cause by both Marangoni and buoyancy driven flow. However, in a small droplet the buoyancy effect can be neglected in comparison to Maran-

goni flow. The existence of Marangoni convection inside the water drops is very weak (Savino and Monti, 1996; Girard *et al.*, 2008). Recently, Jaijus and Singh (2010) have shown the presence of strong Marangoni flow inside the evaporating water drop. In this work, we have focused on the suppression of coffee ring effect by manipulating the internal fluid flow of evaporating drop. Manipulation of internal fluid flow can be achieved by external heating of the surface. The fluid flow inside the evaporating droplet could be a combination of Marangoni and buoyancy flow (Girard *et al*. 2008; Lu *et al.* 2011). The strength of buoyancy flow was neglected in many of these studies. This is due to the small size of the droplet and the density of the particle used in our experimental studies that was nearly same with the liquid density. Experimental investigation in the absence of gravitational effect is impossible. This could only happen when the experiment is carried out in zero gravity condition. However, we have conducted the experiment in such way that the gravitational effect can have negligible effect on fluid motion. In addition, analysis of dimensionless numbers was also performed to determine the strength of buoyancy flow inside the evaporating drop. Numerical simulations at the steady state were also performed to determine the fluid flow inside the evaporating droplet.

## 2.2 Experimental details and methodology

The internal fluid flow and particle transport inside the evaporating drop were determined by the flow visualization technique using PIV. PIV is a measuring technique, which allows us to capture the flow velocity of whole flow field and related properties of the fluids. PIV can provide instantaneous velocity measurements over global (2D or 3D) domains with high accuracy. With modern computers, it is possible to capture up to several hundred recordings per minute and to evaluate a digital recording within a few seconds. It has

unique ability to capture instantaneous flow fields and thus to allow the detection of spatial structures in unsteady flows quantitatively. Experimental flow field data obtained from PIV is very useful for the validation of numerical codes.

### 2.2.1 PIV principle

Particle Image Velocimetry (PIV) is a method of determining velocity fields from images of seeded flows. The main component of PIV setup are light source such as laser, LED; CCD camera; frame grabber; tracers etc. as shown in Figure 2.1. It measures the whole velocity fields by taking two images shortly after each other and the distance of individual particles travelled is calculated within two images. From the known time difference and the measured displacement, the velocity can be calculated. As it is not possible to track individual particles, so a statistical analysis is required. Each image is divided into a grid of small sections called as interrogation areas. The corresponding interrogation areas within each of the two images are then cross-correlated. The cross-correlation function is effectively a pattern matching routine that determines the requirement of displacement to shift the first area to best overlap the second area (Adrain *et al.*, 1995; Adrain and Westerweel, 2010). This area is scaled by the magnification of the camera lens and dividing by time difference, the average velocity for the fluid within the interrogation area is obtained. This process is repeated at each grid point within the image, resulting in a map of velocity vectors to describe the flow.

There are two types of correlation analysis that can be used to determine the particle displacement.

They are:

- **Auto-Correlation Analysis** : Correlate an interrogation spot with itself

- **Cross-Correlation Analysis**: Correlate the first interrogation spot with a second spot that is offset in the mean flow direction.

Cross-correlation analysis is a little more flexible than auto-correlation analysis (Adrain *et al.*, 1995; Adrain and Westerweel, 2010). The principle of cross-correlation analysis is to offset the second interrogation window by an amount roughly corresponding to the local displacement of the particles. This offset significantly increases the probability of obtaining a valid correlation measurement between the *t* and *t'* images. To make this clear, consider a simple example as is illustrated in Figure 2.2. Suppose three particles are located at $x_1$, $x_2$ and $x_3$ in an interrogation spot at time t, (picture I in Figure 2.2a). At time t+Δt, they have moved to the positions $x_1$', $x_2$' and $x_3$' in Figure 2.2a. In passing (I' in Figure 2.2a) we note that $x_2$' is not inside the interrogation spot. This is called "loss of pairs." However, the cross-correlation function, $R_{II'}$ shown in Figure 2.2b is calculated by taking all possible displacements regardless whether the correct particles are correlated with each other or not, i.e., if the particle at $x_1$ would have moved to $x'_3$, then the displacement would be $x_3' - x_1$ and so on. Four of the six possible displacements occur only once, but $x_1' - x_1 \approx x_3' - x_3 \approx d$ occurs twice. Thus, the displacement *d* is the most likely displacement. Two-frame cross correlation is used when *t* and *t'* images are imaged onto separate frames. Correlation function is expressed as (Adrain *et al.* 1995).

$$R_{II'} = R_C + R_D + R_F \tag{2.4}$$

where $R_{II'}$ is the cross-correlation function; $R_C$ is the convolution of mean intensity of images; $R_F$ is the inherent noise in the correlation due to missing particle pairs, background noise, etc., and $R_D'$ are the peaks representing the displacement of the particles over $\Delta t$. Since only a single displacement peak is obtained, two-frame cross-correlation analysis is

ideal for flows that have reversals, since no extra image shifting is necessary to resolve directional ambiguities.

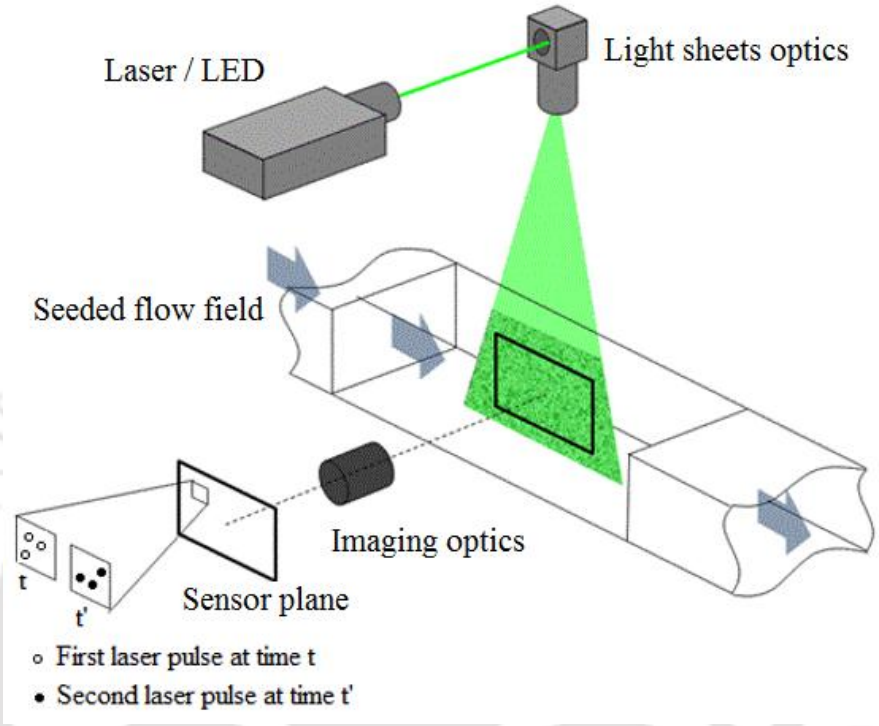


**Figure 2.1.** Schematic representation of PIV analysis.

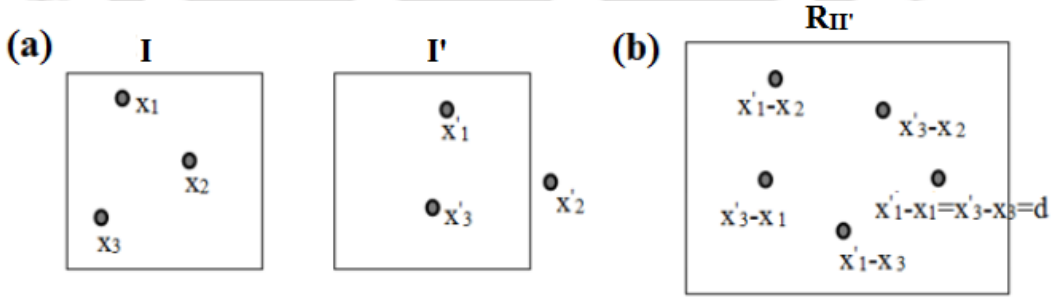


**Figure 2.2.** (a) Image intensity fields $I$ and $I'$ at times $t$ and $t' = t + \Delta t$ respectively. (b) The corresponding cross-correlation of all possible displacements.

### 2.2.2 Image analysis for velocity field

The images of droplet captured by the CCD camera were stored in 680 × 512 pixels, 12-bit grayscale format on a PC via frame grabber. These images were used to

analyze the velocity field and particle concentration. To analyze the velocity field from the images we used PIV lab program (Thielicke and Stamhuis, 2005). The best overlapping pixel area was estimated by varying interrogation window sizes from 64×64 to 128×128 pixels. These images were also used to determine the particle concentration inside the droplet.

### 2.2.3 Evaluation of particle concentration fields

The particle concentration distribution inside the droplet was determined using Particle tracking program in Matlab. This code is used to find the location of the particles and total number of particles inside the droplet.

Algorithm for finding particle concentration as follow:

1. Import image
2. Find the boundary of the droplet
3. Locate particles
4. Count number of particles in an image
5. Go to step 1 and continue till last image

All raw images were imported into the Matlab. Figure 2.3a shows a raw image of droplet captured by the CCD camera. The particles are represented as white spots in these images. The area of interest is the region enclosed between the free surface (top) and solid surface (bottom). Due to light reflection from the top and bottom surfaces the image shows thick white regions there. The boundary of the area of interest was found by locating the free surface and solid surface and the cleaned image which was subjected to PIV analysis is shown in Figure 2.3b. We are assuming that the particles are represented by pixels of intensity range in between 240 and 255. The mean diameter of the particles used in the

experiments was 2 pixels. All pixels having the given intensity range are stored in data files. Location and number of particles are obtained from the above stored data. This gives an idea about the particle concentration and the area in which particles are concentrated.

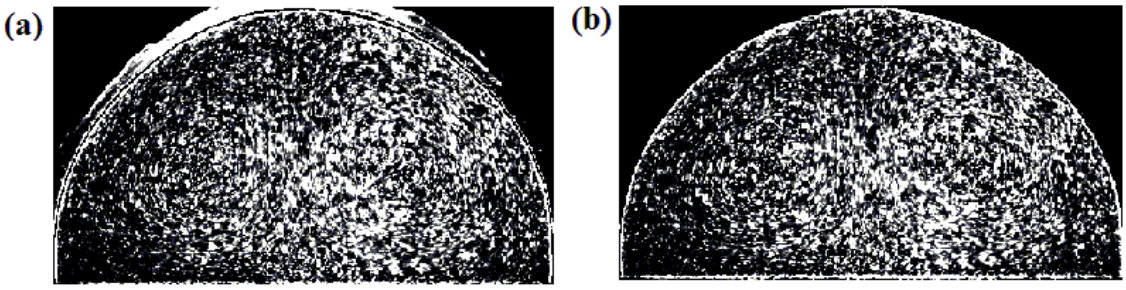


**Figure 2.3.** Image of the droplet captured by the CCD camera (a) raw image (b) Image after processing.

### 2.2.4 Experimental Set up

The experiments were conducted in various conditions of externally heated substrate. Figure 2.4a shows the schematic diagram of our experimental setup. The droplet containing suspended polystyrene particles was visualized by LED light and the images were recorded by a CCD camera (PixFly Hires from PCO) of 1360 ×1024 pixel resolution in conjugation with a zoom lens (Navitar). Since the images were taken in a plane parallel to the disc shaped droplet, there was no need of velocity mapping which arises due to the lens effect from the curved surface in case of a 3D droplet. Figure 2.4b shows the pictorial layout of our experimental setup. The images were recorded at the speed of 19 images $s^{-1}$ and stored in a computer. These images were used to determine contact angle, velocity field and particle concentration. The relative humidity range for all our experiments varied between 30 and 40%. A confined 2D droplet technique developed by the Jaijus and Singh (2010) was used to carry out the experimental investigations. It is true that 2D problem is not a complete analogue to that of the 3D droplet but in those cases where the droplet is

symmetric (which is true for smaller drops) and the internal flow is not chaotic, the evaporation dynamics is qualitatively similar. If we imagine a plane (perpendicular to the substrate) that cuts through the 3D drop with azimuthal symmetry, the velocity profile on this plane will be qualitatively similar to our 2D system as shown in Figure 2.5. It should be noted that this approach may have limitations when the gap of confinement becomes of the order of nanometer. In this proximal regime, the water no longer acts as normal lubricating fluid and its viscosity can increase by orders of magnitude that resist the drainage caused by evaporation (Zhu and Granick, 2001). The confinement-induced viscosity enhancement can be attributed to orientation of water at solid-liquid interface (Sommer and Franke, 2003; Ruan *et al.*, 2004). By using atomic-scale friction force measurements Jinesh and Frenken (2006) have shown that capillary condensation between solid surfaces introduces an elastic response in water making it behave like glue. Sommer *et al.* (2008) have provided a simple and versatile method to probe the nature of nanoscopic water layers on ultrasmooth surfaces. They have shown that the fluidity of interfacial water layers can be tuned with laser light. The stickiness of interfacial water due to increased viscosity can cause stick-slip motion of the receding interface of evaporating water droplet. For sufficiently large confinement gap (similar to the present experiments), it was observed that the nature of the receding interface is similar to the unconfined evaporating droplet (Jaijus and Singh, 2010; Thokchom *et al.*, 2014). In the narrow gap using a syringe, a small water droplet (5-6 mm diameter) having dispersed polystyrene particles was generated touching the wetting substrate. The volume of the droplet was approximately 45 µL. Upon its release, the droplet took the shape of a disc sandwiched between the two parallel non-wetting surfaces whose spacing was nearly 800 µm (Figure 2.6a). The droplet rests on a thin substrate (mild steel of 0.8 mm width) confined between two parallel glass

plates whose inner surfaces were coated with Teflon. The substrate was found to be hydrophilic, whereas the confining walls were hydrophobic in nature. In order to measure the contact angles a 3D drop was placed on the substrate and glass plate and its photograph was taken from the side. The contact angle of substrate and confining walls were measured to be $73^o$ and $140^o$ respectively (Figure 2.6b-2.7c). The evaporation of liquid occurs from the top free surface whose shape is that of semi-circular thin strip. Due to evaporation, the droplet shrinks in height, but its diameter remains constant since the base of the droplet is resting on a wetting surface. The idea of confining the droplet between two parallel and non-wetting surfaces was to allow the height to recede with time. On the other hand, since the substrate was wetting, the contact area (and diameter) remained constant during the evaporation.

In this experiment, three different cases of evaporating droplet placed on external heated substrate were considered. Figure 2.6a shows the schematic of droplet placed on a heated substrate. The temperature of the liquid near the apex ($T_a$), left edge ($T_{e1}$) and right edge ($T_{e2}$) as well as substrate surface ($T_{s1}$ and $T_{s2}$) were measured using K-type thermocouples. The temperature profile of the droplet and substrate surface was estimated by linear fit.

The internal fluid flow inside the evaporating droplet can be a resultant effect of both Marangoni flow and buoyancy flow. For microdroplets the strength of the Marangoni flow is expected to be greater than the strength of the buoyancy convection. It is impossible to separate the buoyancy flow and Marangoni flow within the evaporation process. This can only happen when the evaporation process is carried out in zero gravity condition. We have also carried out some experiments in such a way that gravitational effect can be negligible during the process. The experiment setup described in the previous section is

same except the object plane and camera position has changed in this case (Figure 2.8), i.e. the 2D droplet was placed on a horizontal plane.

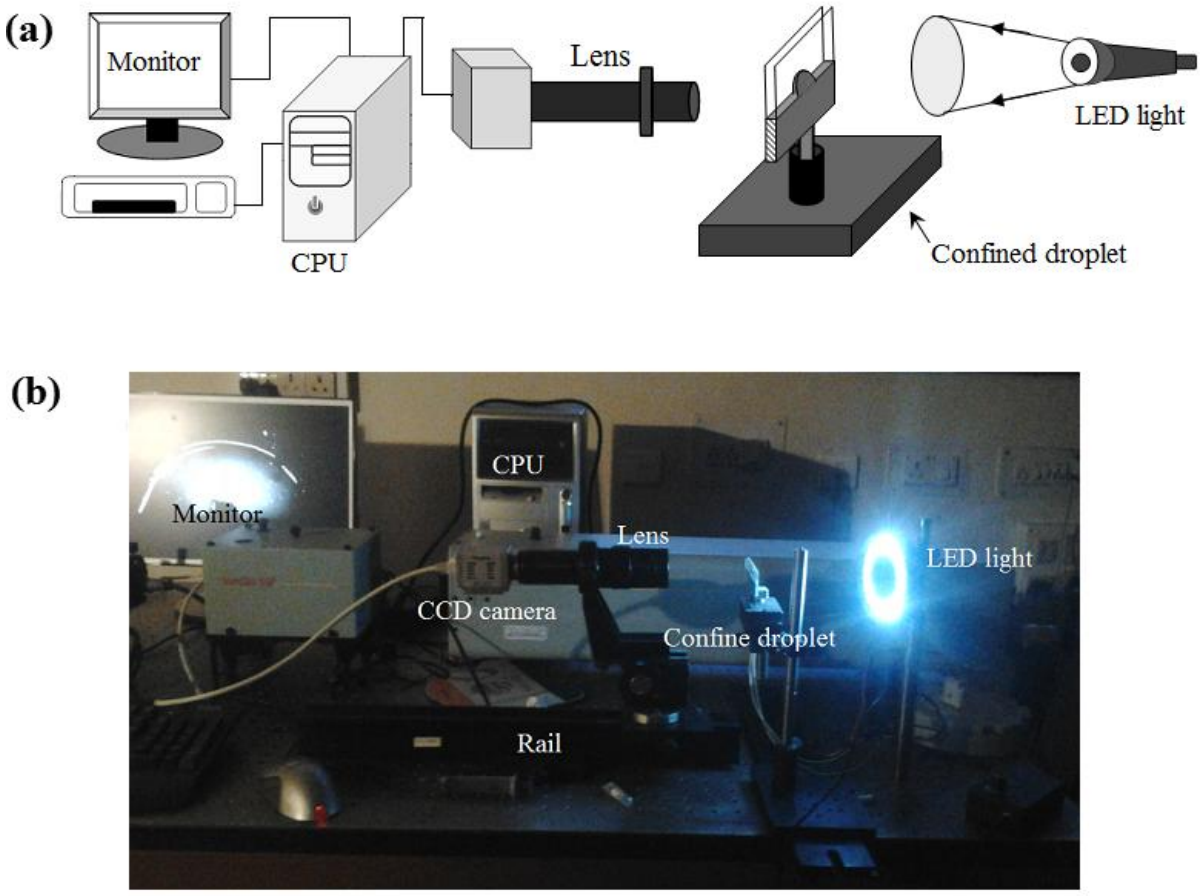


**Figure 2.4.** (a) Schematic diagram of experimental setup. (b) Pictorial representation of the experiment setup.

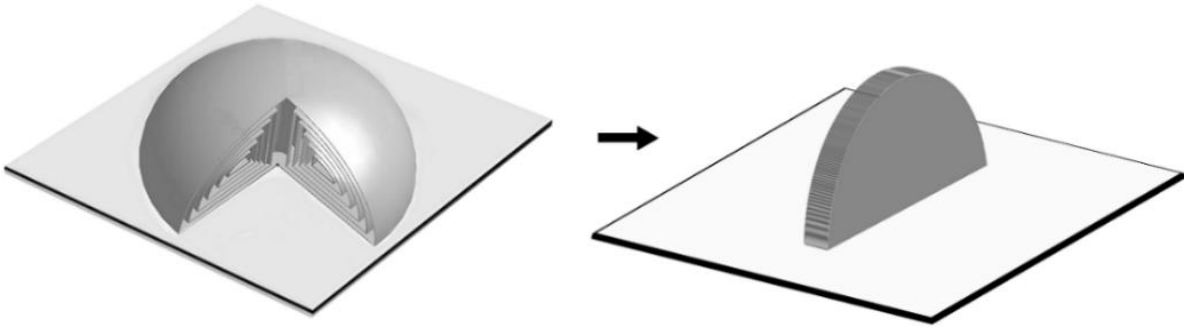

**Figure 2.5.** Analogy of 2D droplet to 3D droplet.

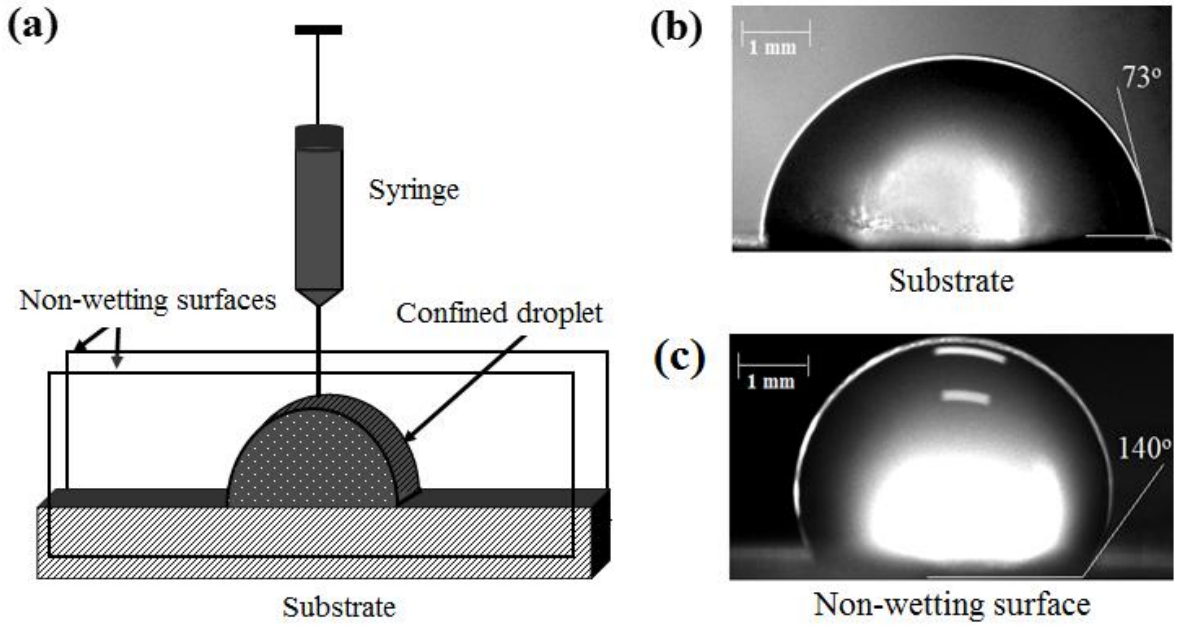


**Figure 2.6.** (a) Schematic diagram of confined droplet. Images of liquid 3D droplet placed on a substrate: (b) Wetting substrate, (c) nonwetting surface.

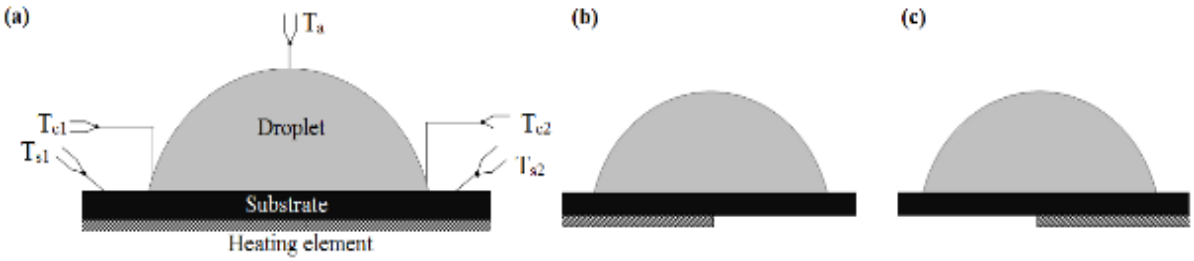


**Figure 2.7.** Schematic diagrams of different cases of substrate heating: (a) Uniform heating of the substrate, (b) Asymmetric bottom heating of the substrate with left half at higher temperature, (c) Asymmetric bottom heating of substrate with right half at higher temperature.

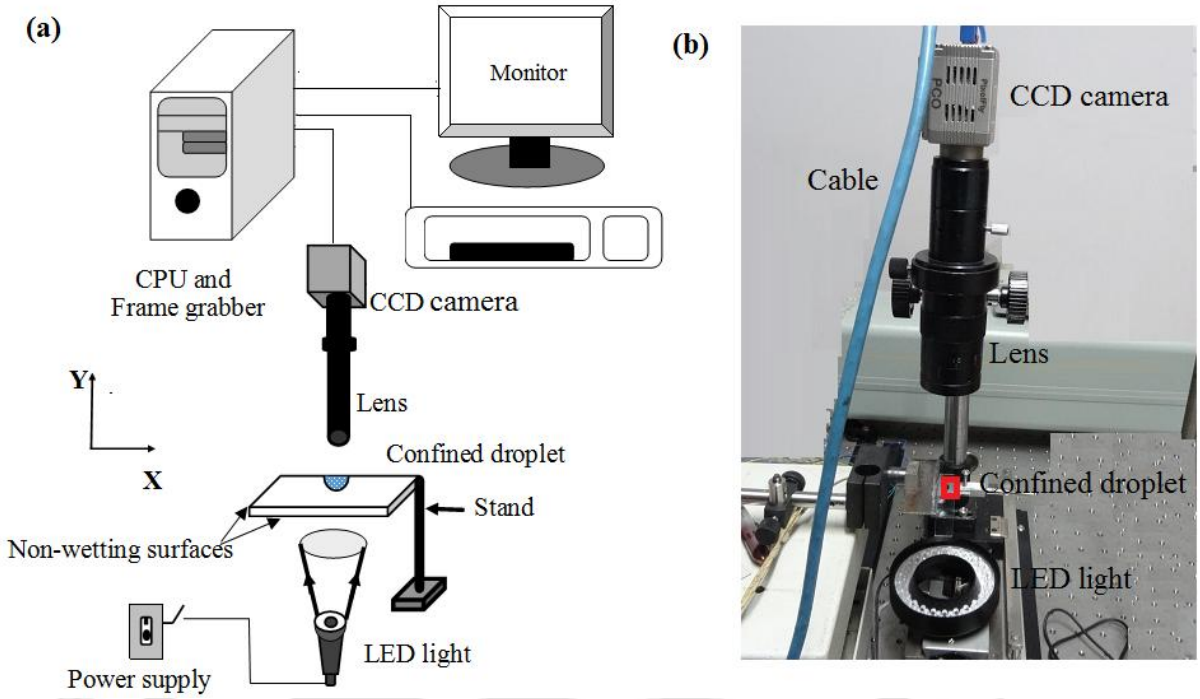


**Figure 2.8.** (a) Schematic representation of experimental set up to isolate buoyancy convection. (b) Pictorial representation of experimental set up.

## 2.3 Numerical simulation

Numerical simulations were carried out by using the boundary conditions and geometry obtained from the experiments. The system is a 2-D sessile droplet of incompressible fluid (water) of constant viscosity and having the shape of a spherical cap resting on a flat surface as shown in Figure 2.9. It is assumed that the contact line of the droplet is pinned to the substrate. A Cartesian coordinate system was used with local radial coordinate x and axial co-ordinate y. Computational fluid dynamics tool (ANSYS FLUENT) was used for the steady state simulations of fluid flow and heat transfer in the droplet. We would like to mention that in an evaporating droplet with pinned contact line, the droplet continuously loses mass, as a result the contact angle and height of the droplet decreases with time. This

makes the problem inherently a transient one and numerical simulation would require the solution of momentum, energy and mass transport equations. Transient simulations can be performed on moving grids. However, in this work we have performed only the steady state solution of continuity, momentum and energy equations on a fixed grid since the objective was to see if the fluid flow profile resulting from buoyancy and Marangoni convection can be predicted qualitatively from the numerical simulation. Therefore, our steady state simulations can be considered at best only qualitative. In a confined disc shaped drop attached to the substrate the only region through which evaporation takes place is the thin circular strip in contact with the air. Therefore, the area of exposure for evaporation is very small and the mass transfer during the evaporation will be low. Hence, the steady state simulation (without considering mass transfer) is expected to give us the qualitative information about the velocity profile.

The governing equations, i.e. continuity, momentum and energy equation are given below:

Continuity equation:

$$\nabla . \boldsymbol{v} = 0 \tag{2.5}$$

Momentum equations:

$$\rho \boldsymbol{v} . \nabla \boldsymbol{v} = -\nabla P + \mu \nabla^2 \boldsymbol{v} + \rho \beta \boldsymbol{g} \Delta T \tag{2.6}$$

Energy equation:

$$\rho C_p \boldsymbol{v} . \nabla T = k \nabla^2 T \tag{2.7}$$

In the above equations $\boldsymbol{v}$ is the velocity, $P$ is the pressure, ρ is the density of the fluid, β is the thermal expansion coefficient of water, μ is the kinematic viscosity, $T$ is the

temperature, $\boldsymbol{g}$ is the gravitational acceleration, $\boldsymbol{k}$ is the thermal conductivity and $C_p$ is specific heat capacity.

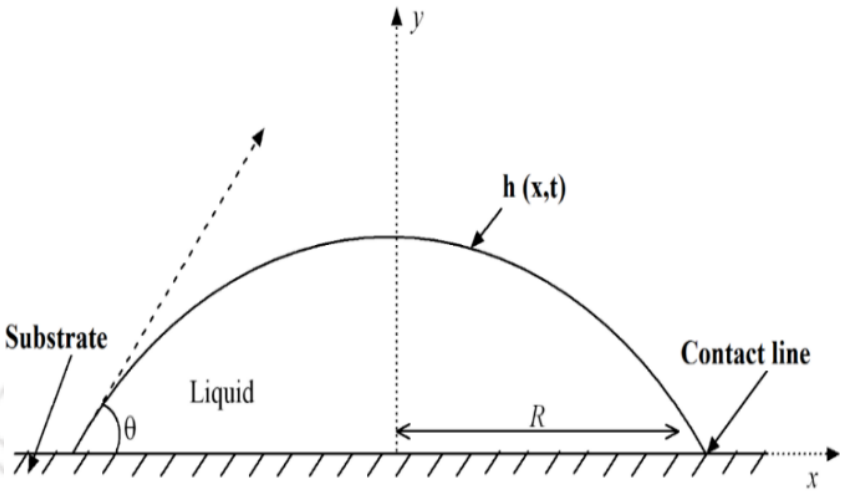


**Figure 2.9.** Computational domain.

The boundary conditions considered in the simulations are given below:

1. The bottom substrate is considered as no-slip wall.
2. The temperature of the solid substrate as well as free surface of the droplet is assumed to vary linearly with *x* co-ordinate.

This approximation is valid because the size of the droplet is very small. Therefore, the change in the temperature is almost linear over the droplet free surface and bottom substrate. At the liquid-gas interface, a tangential Marangoni stress due to free surface temperature variation is considered. The rate of change of surface tension with temperature $\left(\frac{\partial \sigma}{\partial T}\right)$ was assumed to be $0.0001627\ \mathrm{N\ m^{-1}{}^{\circ}C^{-1}}$ as reported by Hu and Larson (2006).

The governing equations (2.5-2.7) along with the above mentioned boundary conditions were solved using the finite volume method. To verify the grid independent solution, simulations were conducted on two different grids having 46206 (grid A) and

76056 (grid B) quadrilateral cells. The differences in the results from the two grids were found to be negligible confirming the grid independent solution. The results of simulations performed on grid B are presented in the following section. The results obtained from simulations were analyzed to understand the velocity field and circulation pattern.

## 2.4 Results and discussion

### 2.4.1 Analysis of height and contact line during evaporation

In order to show that a confined disc shaped droplet undergoes similar changes as one would observe in case of a 3D droplet, we have compared our results with that of Zhang et al. (2013). In our experiments the droplet was confined between two non-wetting parallel plates which enables the droplet height to continuously decrease with time in a similar fashion as one would observe in case of an unconfined droplet. The only restriction is that the gap width should be much larger than the mean free path which is typically of the order of nanometer. As already mentioned, in this proximal regime, the water viscosity increases by the orders of magnitude that resist the drainage caused by evaporation. In our experiments, the gap between the two confining surfaces was 800μm. For such large gap, the dynamic of the interface was found to be qualitatively similar with unconfined 3D evaporating droplet. Figure 2.10 shows the plot of height with time. In this plot, the height h is normalized by initial height $h_o$ and evaporation time. It was observed that the height of the droplet decreases linearly with time. This clearly shows that the lateral non-wetting surfaces are not changing the droplet dynamics. Figure 2.11 shows the time sequence of images of the droplets subjected to different cases of substrate heating as we mentioned above. The images show that the height of the droplet changes with time but the contact line remains pinned throughout the process.

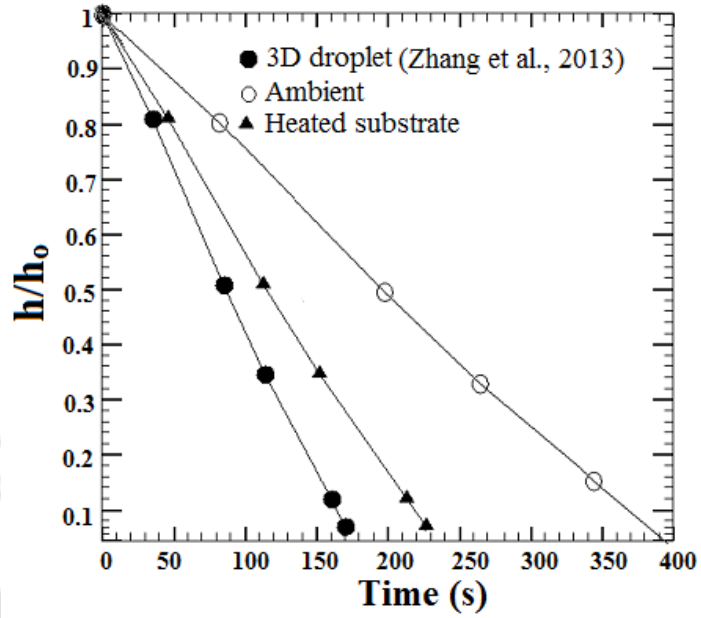


**Figure 2.10.** Time evolution of height of the droplet with time.

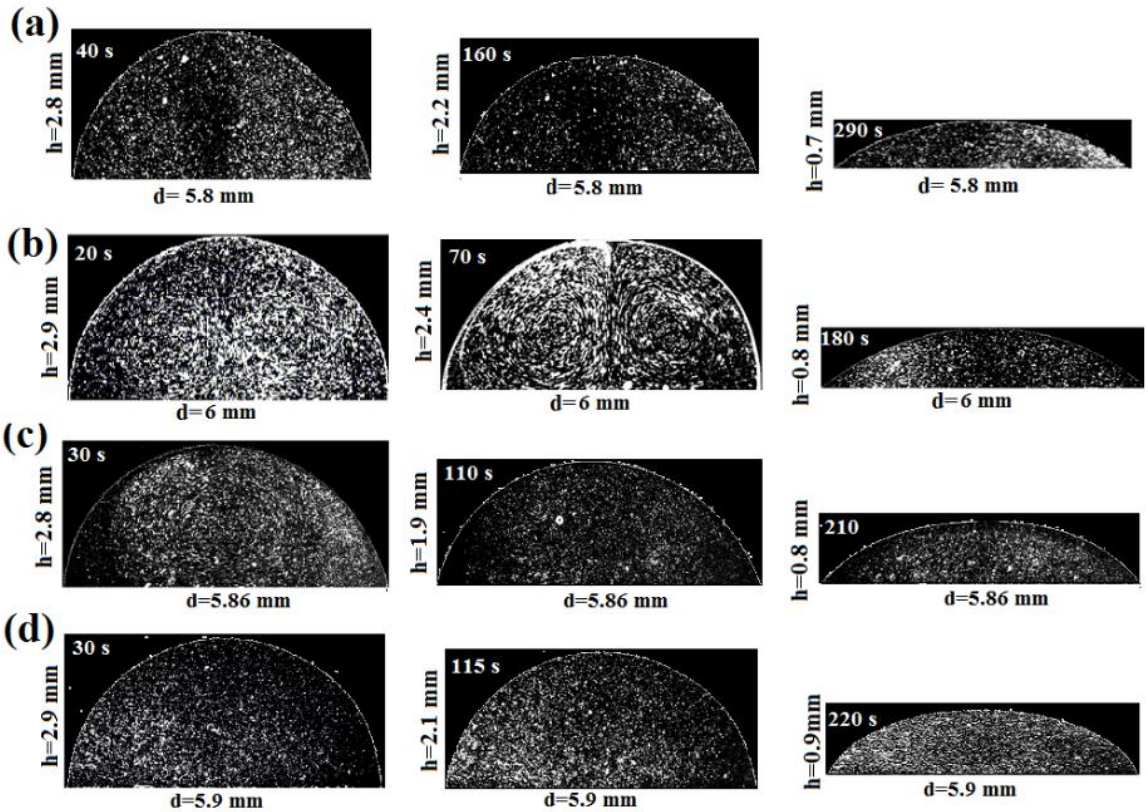


**Figure 2.11.** Time sequence of the images of the droplet (a) Ambient condition (b) Symmetric heating of the substrate (c) Asymmetric heating of the substrate (TL > TR) (d) Asymmetric heating of the substrate (TL < TR)..

## 2.4.2 Velocity field

In this section, we describe the velocity filed inside the droplet subjected to different conditions of evaporation. First, we discuss the results when the droplet was left to evaporate in ambient conditions. In this case, the substrate temperature was uniform, however lower than the droplet free surface. A small drop of water containing polystyrene particles was released near the bottom substrate from a syringe through the gap between the two parallel glass plates. As the droplet touched the wetting surface, it spread in the form of a half-disc between the two non-wetting surfaces. After 60 s, the CCD camera started grabbing the images of the droplet.

To establish the strength of the Marangoni convection, the measurement of droplet surface temperature profile is needed. We have measured the temperature at different point on the liquid surface and bottom substrate using K-type thermocouple. IR thermography has been used by Lu *et al*. (2011) and Saha *et al.* (2010) to measure the surface temperature of 3D evaporating droplets. Since the drop size in our experiments was quite small, a very high-resolution IR camera was required to measure the surface temperature profile. Moreover, the droplet was sandwiched between two glass plates; therefore the IR camera (if placed normal to the droplet plane) could have measured the temperature of the top surface of the glass plate and not the actual temperature inside the liquid. It was possible to get free surface temperature profile by taking the IR images from the top view (above the gap between the two glass plates) but curvature of the drop can make the measurement erroneous unless a high resolution camera with proper image correction is used. Due to unavailability of high-resolution IR camera in our lab, we have measured the temperatures at the apex and two edges of the droplet using thermocouples and the profile was estimated

by linear fit. We expect this to be good approximation since the temperature difference was not large. The highest temperature was recorded at the apex of the droplet. Figure 2.12a shows the experimental velocity vectors superimposed over the velocity contour when the height of the drop was 2.8 mm. Since the temperature at the apex was higher compared to the edge region, the surface tension would be higher at the edge and lower at the top free surface. The resulting gradient in surface tension will cause Marangoni stress on the droplet free surface pulling the liquid towards the bottom along the liquid-air interface. This will setup symmetric but counter-rotating Marangoni convection cells such that the fluid rotates clockwise in the right half but anti-clockwise in the left half. Similar convection cells were also observed by Kang et al. (2013) and Jaijus and Singh (2010) with the suspension of polystyrene particles. Similar flow patterns were also observed at later stages of the evaporation. But it was observed that towards the end of the evaporation process, the Marangoni flow is weak and the fluid was found to move radially outward due to capillary forces as shown in Figure 2.12d. This is expected since at small contact angle the difference in the surface temperature is too small to sustain the Marangoni convection. At low contact angles, the outward capillary flow arises due to maximum evaporation flux near the contact line.

The steady state simulations were carried out for droplets with the same geometry. The temperature boundary conditions at the droplet free surface and bottom substrate were assigned in the form of linear profile obtained from the experimental measurements of temperatures at various points. The Marangoni stress condition was applied on the free surface of the droplet. The velocity vectors superimposed over the contour obtained from the numerical simulation are shown in Figure 2.12(e-h). The velocity field and recirculation patterns observed in the simulations are found to be in good qualitative

agreement with the experiments. However, the direction of the fluid flow obtained from the experiments towards the end (290 s) was found to differ from the simulation result. The reason for this quantitative difference is that in the steady state simulations, momentum flux resulting from the evaporation was not considered. In addition, Marangoni stress along the droplet air interface was considered in the numerical simulation which in the experiments were expected to be small at the end of the process.

In contrast to the evaporating droplet in ambient condition, the direction of the circulations was reversed in the case of a droplet placed on a symmetrically heated substrate. Figure 2.13(a-d) shows the velocity vectors superimposed over the velocity contour for this case. The temperatures at various points are also shown in figure. The measured temperature near the edge was higher than the apex. This difference in temperature will create surface tension gradient along the droplet free surface such that the Marangoni stress pulls the fluid towards the apex along the liquid-air interface. As expected in this case also we observe two symmetric but counter-rotating convection cells whose direction is opposite to that observed in the previous case. The velocity profile for this case obtained from the steady state simulations are shown in Figure 2.13(e-h). The recirculation patterns predicted from the simulation are in good agreement with the experimental observations and the velocity magnitude are found to be higher for the same reason as mentioned previously.

Figure 2.14(a-d) shows the experimental results of velocity vectors superimposed over the velocity contours for the case of asymmetric heating of the substrate. Since in this case the left side of the substrate was heated, it was noticed that the droplet temperature at the left edge ($T_L$) is higher than the apex ($T_A$) and right edge ($T_R$). Thus, the temperature

on the free surface decreases monotonically from left to the right. Consequently, the surface tension gradient is set up with right edge having the maximum surface tension value and left edge the minimum. The resulting Marangoni stress drives the fluid towards the right edge along the air-liquid interface creating a convection cell in the clockwise direction. As expected, there is only a single convection cell. The simulation was carried out using surface temperature profiles obtained from the experiment. The temperature profile at the left half of the droplet free surface was assigned as linearly varying profile between the left edge and apex temperature. Similarly, the right half of the free surface was assigned linearly varying temperature profile between the apex and right edge temperature. The temperature profile at the substrate boundary was also a linear one whose form was evaluated from the left and right values. Figure 2.14(e-h) shows the corresponding velocity profiles obtained from the simulations. Again, the velocity field is observed to be in good qualitative agreement with the experiment.

In another experiment only the right half of the substrate was heated. This arrangement creates a temperature field where the temperature close to the right edge ($T_R$) was higher than the left edge ($T_L$) and the droplet apex temperature was in between the left and right values. Therefore, an asymmetric temperature gradient on the free surface of the droplet is created whose direction is just opposite to the previous case. This temperature gradient leads to higher surface tension at the left edge compared to the right edge that induces the Marangoni flow from the region of the low surface tension to the region of high surface tension. As expected, it can be observed in Figure 2.15(a-d) that a single convection cell in counter clockwise direction is setup. Figure 2.15(e-h) shows the velocity profile obtained from the simulation corresponding to this case. The results are in qualitative agreement. It is expected that unsteady simulations in which the computations

are performed on a moving grid with proper evaporation flux at the surface of the droplet would perhaps provide quantitative agreement as well.

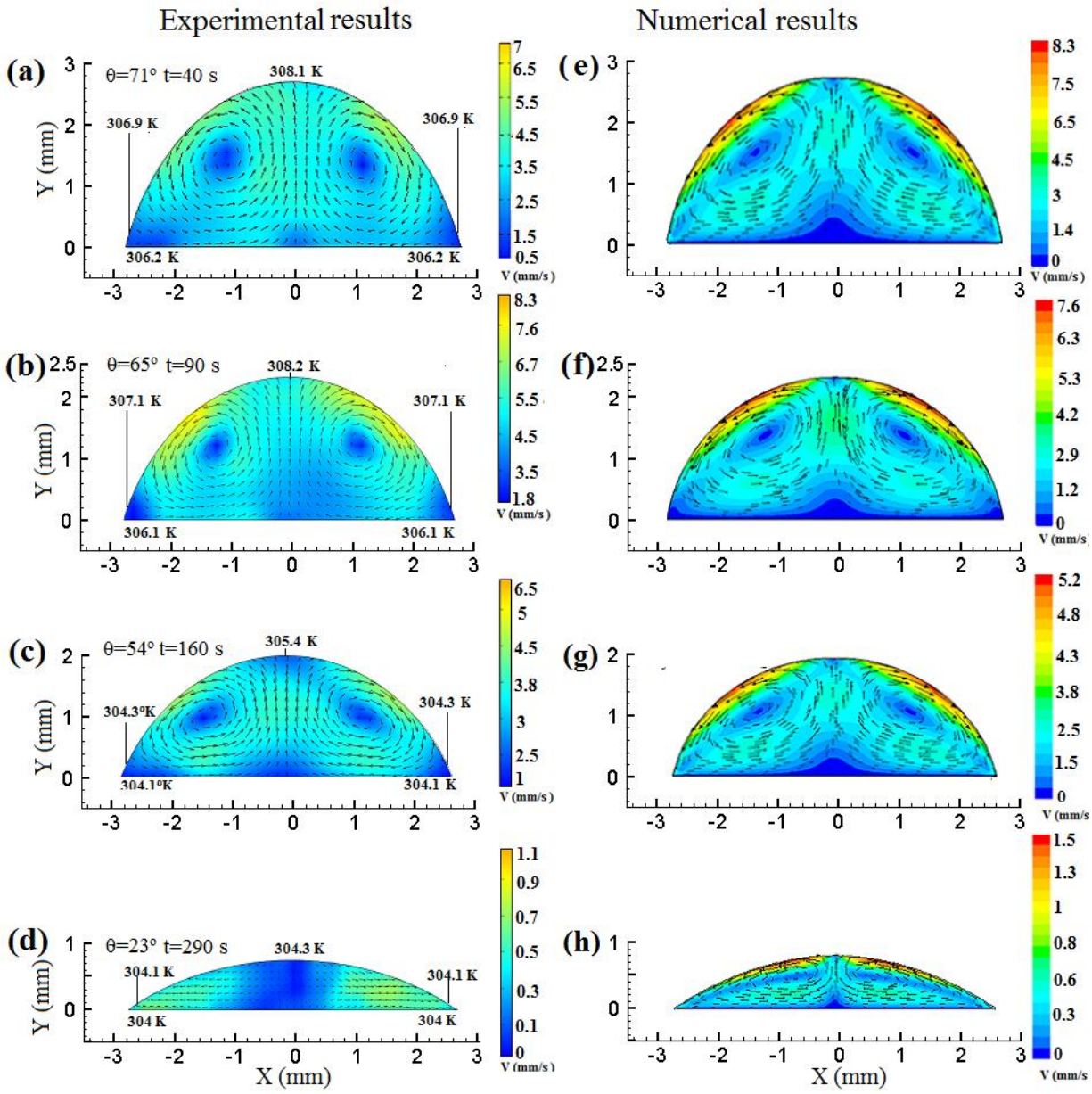


**Figure 2.12.** Experimental velocity vectors superimposed over velocity field contour colored by its magnitude during evaporation of droplet placed on the substrate in ambient condition after recorded at (a) 40 s, (b) 90 s, (c) 160 s and (d) 290 s. The right column (e-h) shows the corresponding velocity fields obtained from numerical simulation.

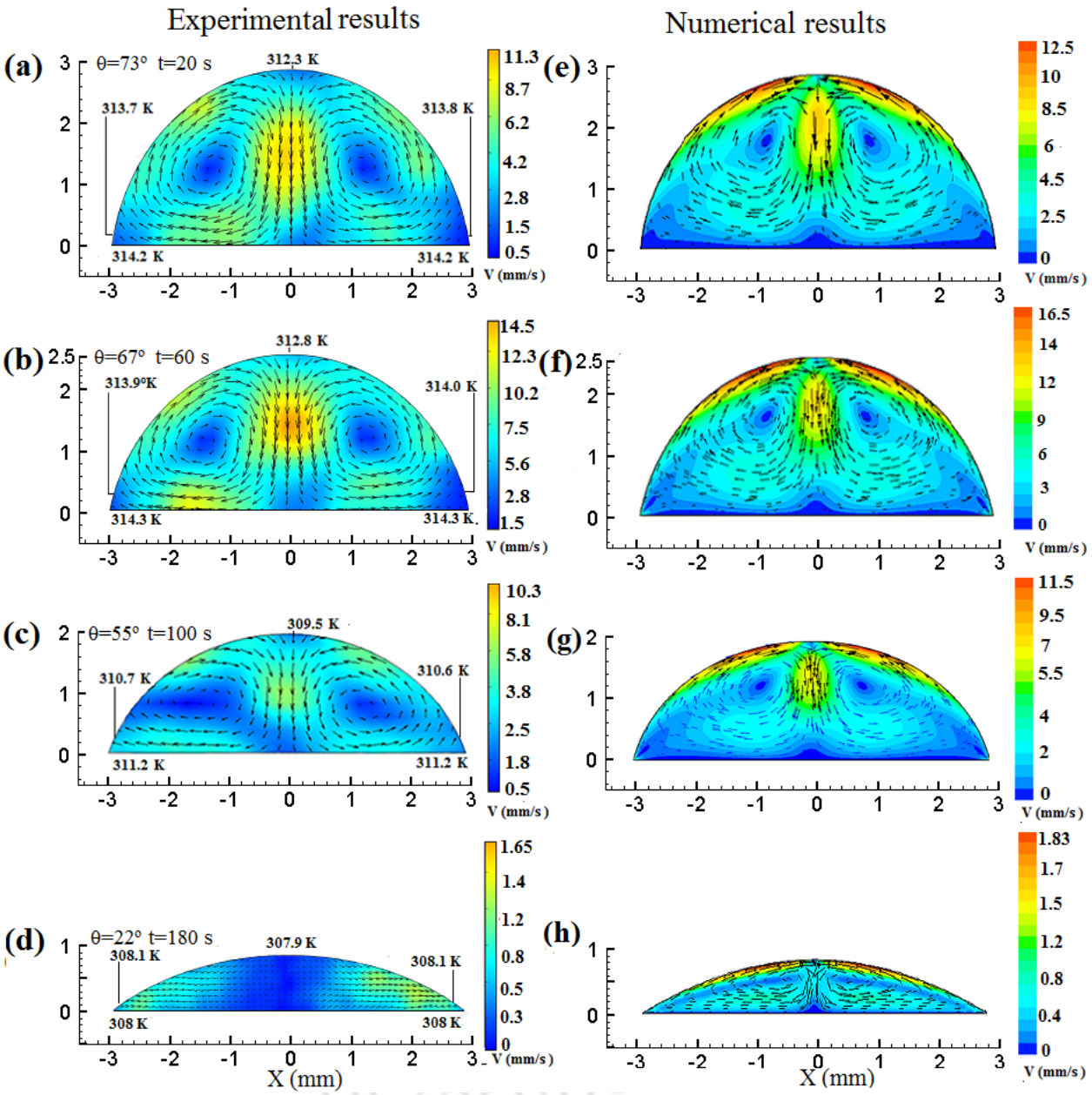


**Figure 2.13.** Experimental velocity vectors superimposed over velocity field contour colored by its magnitude during evaporation of droplet placed on the uniform symmetric heated substrate after recorded at (a) 30 s (b) 60 s (c) 100 s and (d) 180 s. The right column (e-h) shows the corresponding velocity fields obtained from numerical simulation.

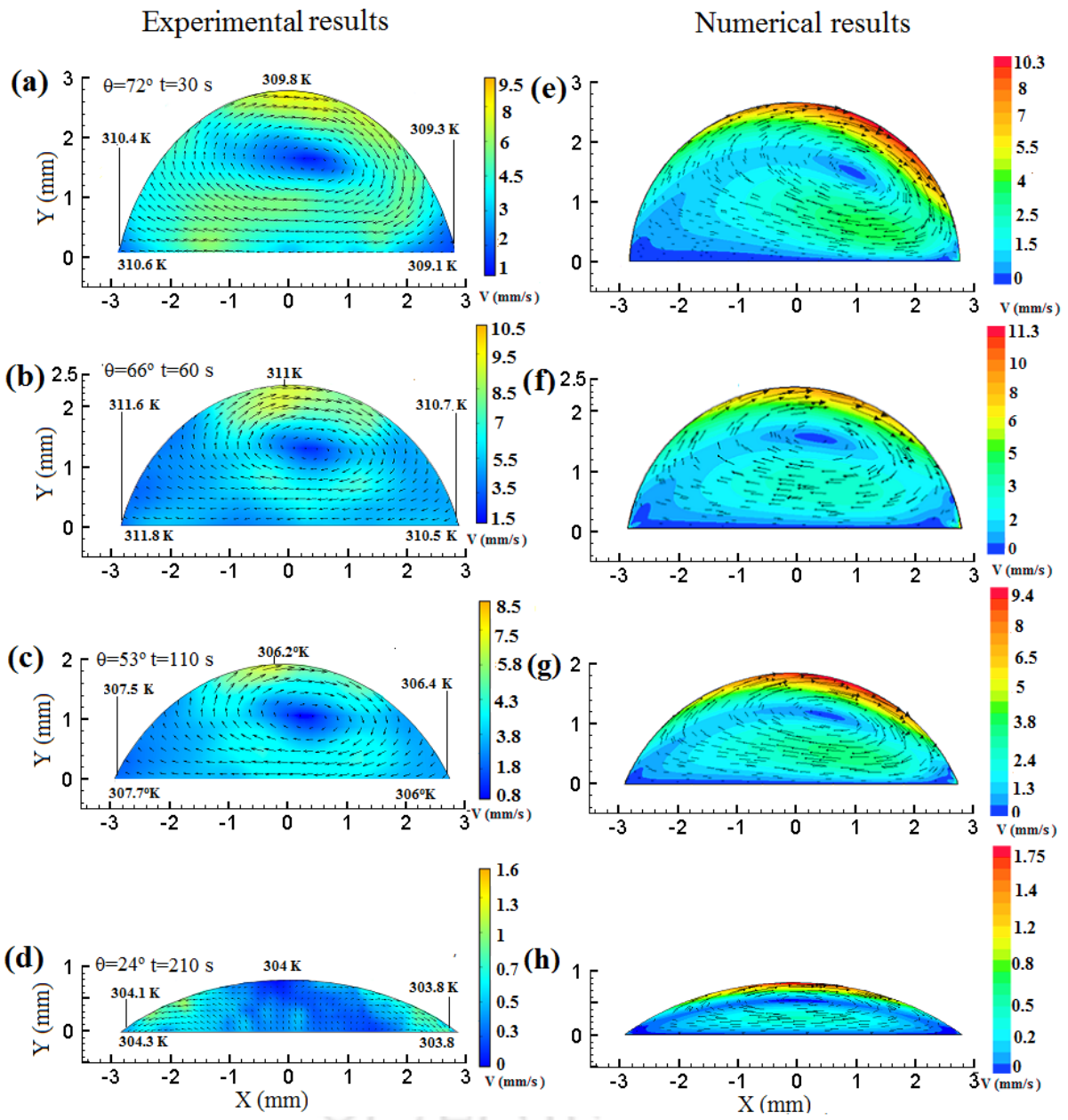


**Figure 2.14.** Experimental velocity vectors superimposed over velocity field contour colored by its magnitude during evaporation of droplet placed on the asymmetric left heated substrate after recorded at (a) 30 s (b) 60 s (c) 110 s and (d) 210 s. The right column (e-h) shows the corresponding velocity fields obtained from numerical simulation.

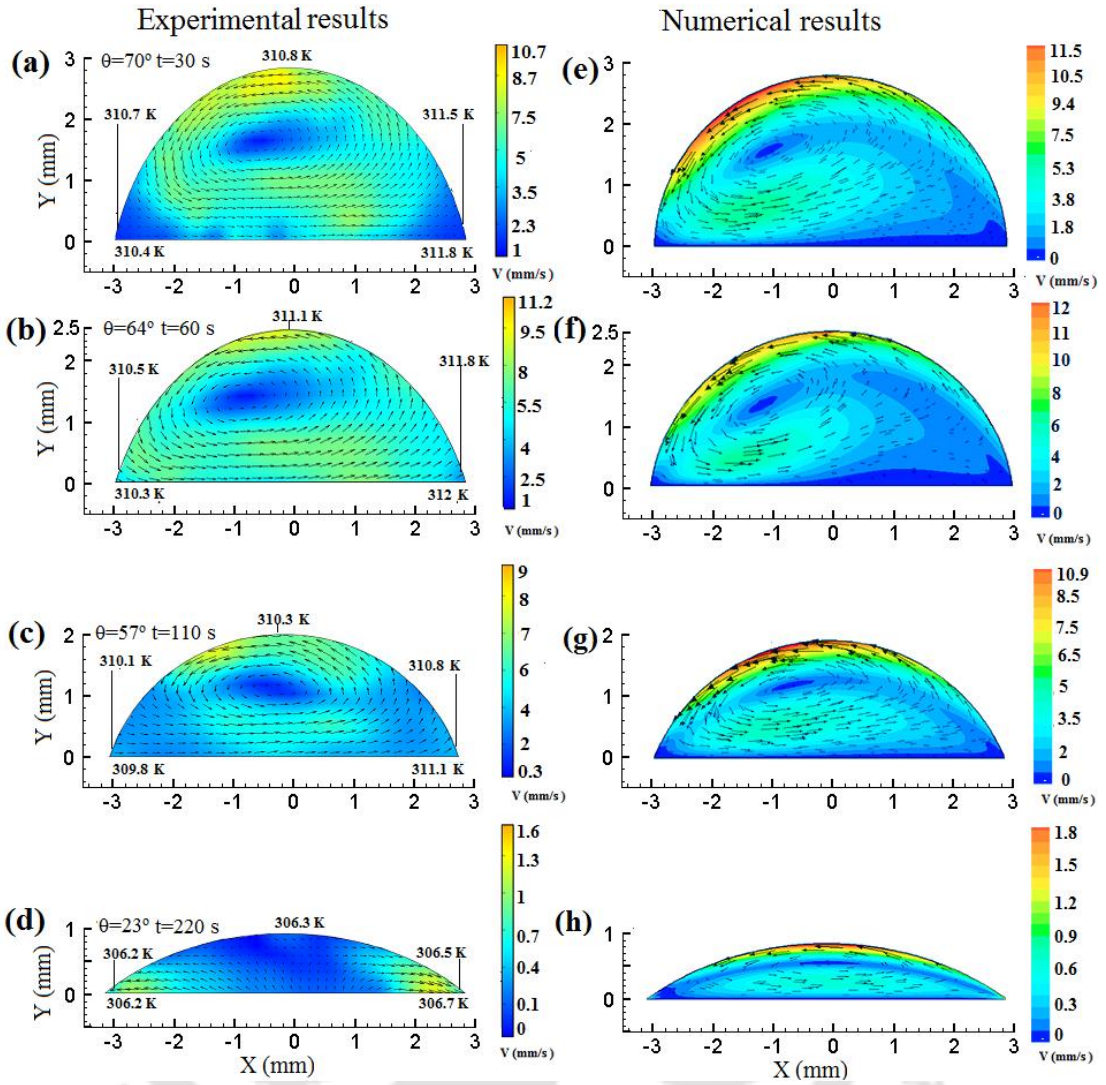


**Figure 2.15.** Experimental velocity vectors superimposed over velocity field contour colored by its magnitude during evaporation of droplet placed on the asymmetric right heated substrate after recorded at (a) 30 s, (b) 60 s, (c) 110 s, and (d) 220 s. The right column (e-h) shows the corresponding velocity fields obtained from numerical simulation.

## 2.4.3 Strength of Marangoni and buoyancy convections

The fluid motion driven by Marangoni effect as well as buoyancy effect can co-exist inside the evaporating droplet. Most of the studies believed that the fluid motion due to buoyancy effect inside the microdroplet is very weak as compared with the Marangoni convection.

In this experiment, we were interested to see that the flow motion driven by Marangoni stress along the droplet free surface may exist even where the gravity effect is negligible. Since it is difficult to isolate the Marangoni convection within the process, we have conducted the experiments in such a way that the buoyancy effect can be negligible within the process. The experimental set up was described in the previous section. Figure 2.16 shows the superimposed velocity vectors with velocity contour of evaporating droplet kept in ambient condition recorded at time 60 s and 180 s respectively. As expected two counter rotating convection cells driven by the Marangoni stress was observed. When the evaporating droplet was subjected to symmetric heating of the substrate, the direction of the fluid motion as mentioned above was found to reverse (Figure 2.17). This is due the change of surface temperature gradient induced by the heated substrate. A single Marangoni convection inside the droplet was observed when the droplet is subjected to asymmetric heated substrate. Figure 2.18 is the velocity filed when the left half of the substrate was heated (TL>TR) while Figure 2.19 is the velocity filed when the right half of the substrate was heated (TL<TR). The magnitude of the velocity field is nearly same as in the previous cases when the droplet was in a vertical plane. This indicates that the fluid motion inside the evaporating droplet is mostly driven by the Marangoni convection. The results were qualitatively similar with the velocity field describe in the previous section. Numerical simulations were also conducted to verify that the strength of the Marangoni convection is dominant inside the evaporating droplet. In these simulations, the boundary conditions were same as reported in the earlier simulations except the Marangoni stress condition was not assigned to the gas-liquid interface, i.e. the interface had zero shear stress. In alternative words, these simulations were considered only for buoyancy driven flow. Similar flow patterns were observed inside the evaporating droplet

as shown in Figure 2.20. However, the velocity magnitude is insignificantly small as compared with the magnitude of the velocity with the Marangoni stress boundary condition at the interface of the droplet. These results show that the strength of the Marangoni convection is much stronger compared to the buoyancy flow.

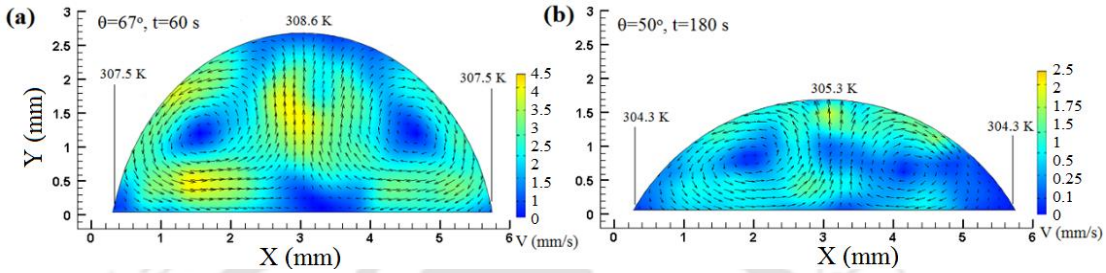


**Figure 2.16.** Velocity field inside the droplet for the case of ambient condition recorded at (**a**) 60 s and (b) 180 s respectively. θ represent the contact angle. The aspect ratio of the images has been changed for the clarity of velocity vectors.

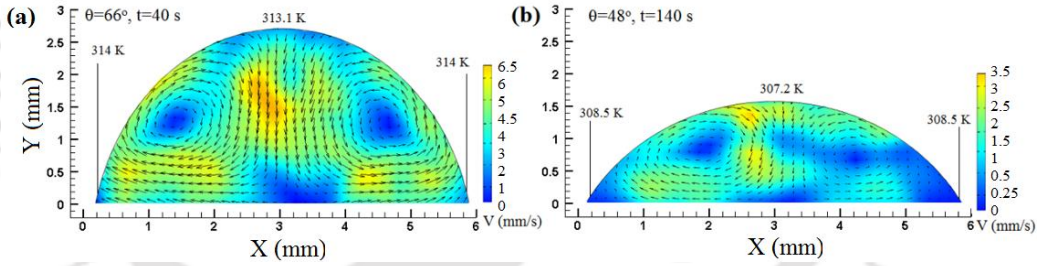


**Figure 2.17.** Velocity fields inside the droplet for the case of symmetric heated substrate recorded at (**a**) 40 s (b) 140 s respectively. Other detail is same to Figure 1.

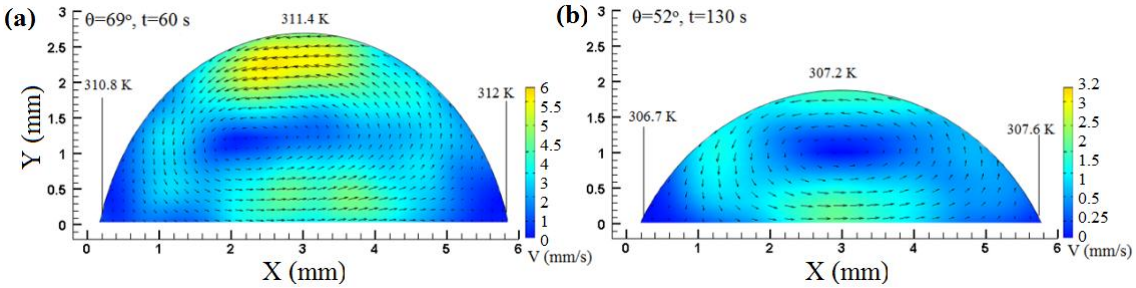


**Figure 2.18.** Velocity field inside the droplet for the case of asymmetric left heated substrate recorded at (a) 60 s (b) 130 s respectively. Other detail is same to Figure 1.

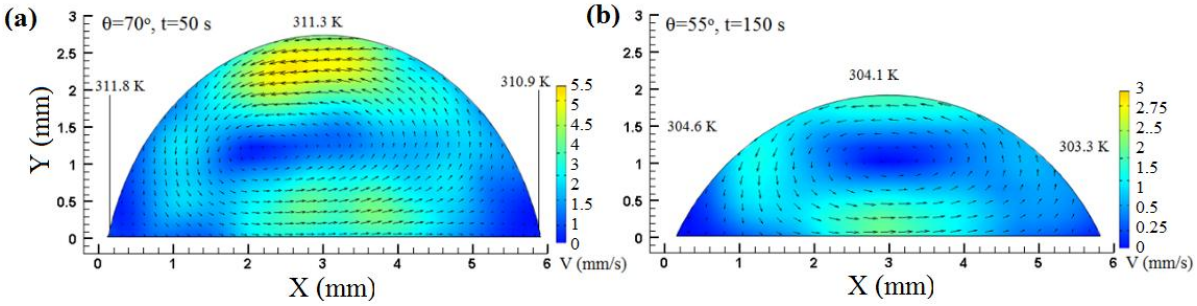


**Figure 2.19.** Velocity field inside the droplet for the case of asymmetric right heated substrate after recorded at recorded at (**a**) 50 s and (b) 150 s respectively. Other detail is same to Figure 1.

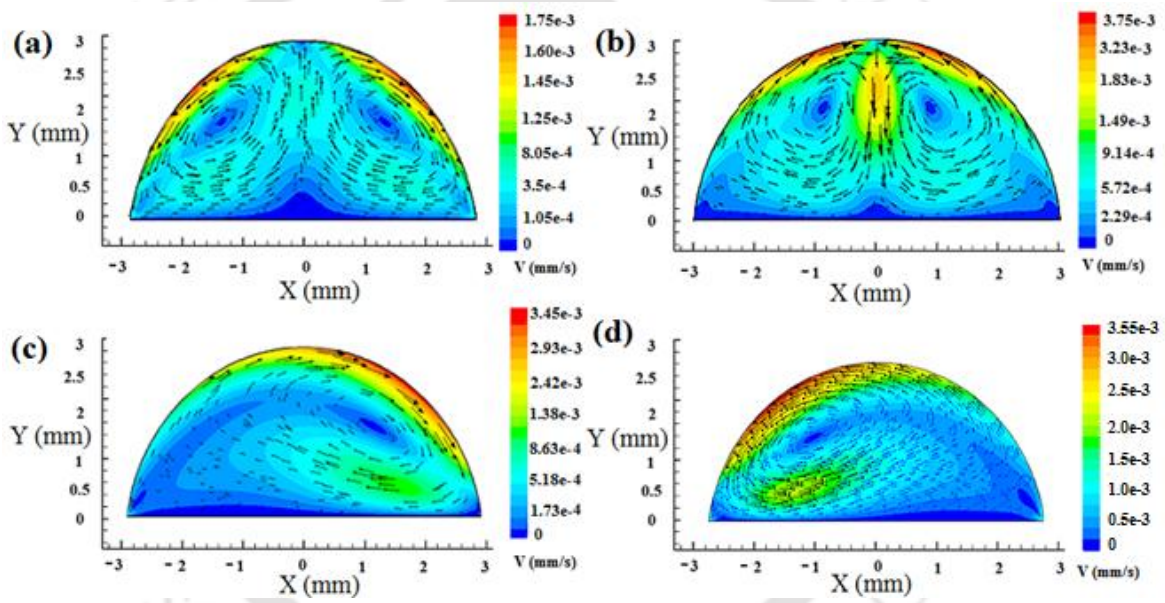


**Figure 2.20.** Velocity field from numerical simulation without considering the Marangoni stress boundary condition at the free surface. (**a**) Ambient condition (**b**) Symmetric heating of the substrate (**c**) Asymmetric heating of the substrate (TL > TR) (**d**) Asymmetric heating of the substrate (TL < TR).

The relative contribution between natural convection and Marangoni convection inside the droplet is given by the Bond number ($B_o$) which is the ratio of buoyancy force to the surface tension force. When $B_o$<<1, internal flow is dominated by the Marangoni

convection. The non-dimensional number used to characterize the strength of natural convection is the Grahshoff number (Gr) which is the ratio of buoyancy force to viscous force The natural convection can be ignored when Gr < 2400. For a pure liquid droplet, a thermal Marangoni number (Ma), defined as ratio of surface tension gradient induced by the temperature gradient to viscous force is utilized to describe the intensity of Marangoni convection. Marangoni convection can be neglected when Ma is less than 100. The values of these dimensionless numbers that existed in an experiment are given in Table 1. These values clearly indicate that all our experiments were strongly dominated by Marangoni convection. This Marangoni convection causes the suspended particles to move along with the fluid path lines. In our PIV experiments, the suspended particles also act as tracer particles whose images are analyzed for cross correlation.

**Table 1: Dimensionless numbers**

| Cases | R | Gr | Ma | Bo |
|---|---|---|---|---|
| Ambient condition | 2.86 | 60.1 | 17400 | 0.0168 |
| Symmetric heating of the substrate | 3.0 | 69.4 | 18200 | 0.0185 |
| Asymmetric heating of the substrate (TL>TR) | 2.80 | 56.4 | 17000 | 0.0161 |
| Asymmetric heating of the substrate (TL<TR) | 2.95 | 65.9 | 17900 | 0.0179 |

### 2.4.4 Particle concentration inside the evaporating droplet

In the previous section, we observed that the temperature distribution along the droplet free surface can strongly influence the internal fluid flow. For very low Stokes number

(St) the dispersed particle would simply follows the fluid streamlines. The maximum fluid velocity observed in our experiments was 16.5 mm/sec. For 10 µm diameter polystyrene particles (density ~ 1.05 gm/cc) dispersed in 5 mm diameter water droplet (density ~ 1 gm/cc, viscosity ~ 1 cp) the Stokes number (St) is O ($10^{-3}$). Therefore two-way coupling is not expected and the particles do not disturb the fluid flow. Therefore, the nature of circulation pattern inside the droplet would govern the concentration profile. In this section, the particle concentration inside the droplet is presented for all the four different experiments discussed in the previous section. To evaluate the normalized area averaged particle density ($N_i/N_T$) of dispersed particles the droplet is divided into 6 bins of equal width. The particle concentration ($N_i/N_T$) denotes the number of particles dispersed in a bin per unit area at any time ($N_i$) divided the total number of particles per unit area initially present in the droplet ($N_T$). The number of particles in the droplet was calculated using a particle tracking program. The intensity of images ranges from 0 to 255. An average pixel size of particles in the images was 2 pixels. In the particle counting code, two adjacent pixels with intensities between 240 and 255 was counted as one particle. The area of interrogation was same in all the images. Therefore, the particles which deposited were also considered in the particle count based on the pixel count. All the particles were tagged and counted. Figures 2.21 to 2.24 show the time evolution of normalized particle number density ($N_i/N_T$) for the different cases of evaporation. The normalized particle density is plotted against the bin number. It can be observed that as the evaporation progresses the particle density in several bins undergoes significant changes. Figure 2.21a shows the evolution of the particle number density for the case of evaporation under ambient conditions. It can be noticed that the initial particle concentration inside the bins are nearly same. As the evaporation proceeds, the change in the particle concentration inside the bins

can be observed. The particle concentration in the central region (bins 2, 3, 4 and 5) decreases whereas the particles close to the edges (bin 1 and bin 6) increases with time. The evolution of the concentration profile suggests that a ring like stain will be formed after complete evaporation of the droplet. To verify the prediction of deposition pattern, the image of the particles left on the substrate after the complete drying of 3D droplet was taken. The droplet of polystyrene particles was kept on the substrate for drying in ambition condition. The image showed a ring like deposition pattern on the substrate after complete evaporation as shown in Figure 2.21b. Figure 2.22a shows the concentration profile when the droplet was left to evaporate on the symmetric heated substrate. In this case, the particle concentration in the central region (bin 3 and bin 4) increased whereas the particles close to the edges (bins 1, 2, 5 and 6) decreased with time. The image of the particle deposition pattern of the 3D droplet placed on the heated surface is shown in Figure 2.22b. As expected, the particles are deposited in a spot like pattern near the center. Figure 2.23a shows the evolution of particle concentration profile for the case of asymmetric heating of the substrate. In this case, the left-half was maintained at higher temperature. It can be observed that the particles present in the concentration bins near the right edge (bin 5 and bin 6) increases whereas the particles near the right half region (bins 1, 2, 3 and 4) decreases with time. This is attributed to the direction of the velocity vector as described in the previous section on the velocity profile. The image of final deposited pattern shown in Figure 2.23b clearly shows that after the complete evaporation the particles are deposited towards the right side. The time evolution of particle number density inside the droplet evaporating on a substrate with right half at elevated temperature is shown in Figure 2.24a. In this case, also only one convection cell was observed but its direction was counter-clockwise with downward pointing velocity vectors on the left side. Such motion

is likely to transport the particles towards the left edge. The particle count on the left half (bin 1 and 2) increases whereas there is decrease in the bins on the right side. As predicted by the velocity field and particle concentration dynamics most of the particles are deposited on the left side of after complete evaporation as shown in Figure 2.24b.

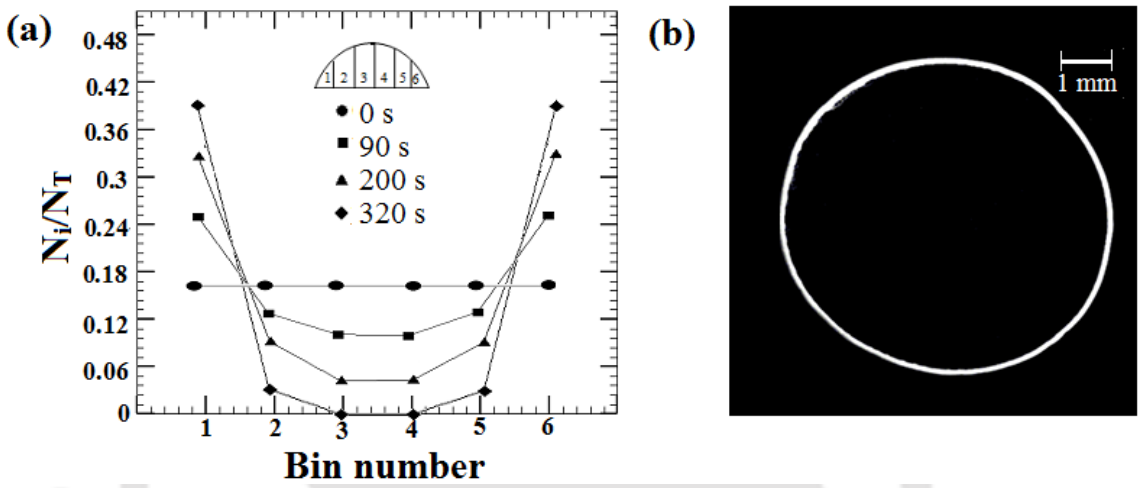


**Figure 2.21.** (a) Concentration profile of particles inside the evaporating droplet for the case of ambient condition, (b) snapshot of the particle deposition pattern.

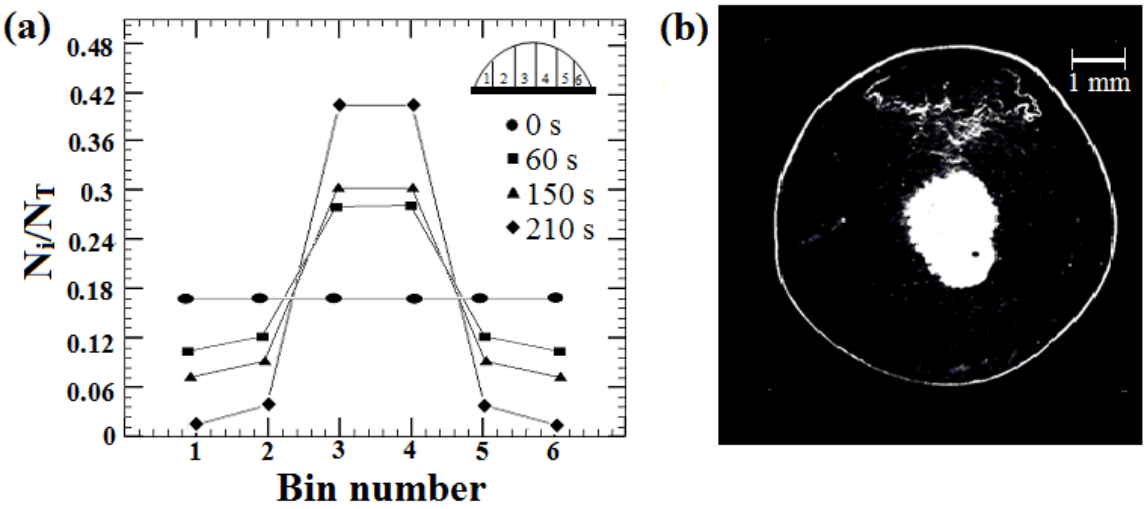


**Figure 2.22.** (a) Concentration profile of particles inside the evaporating droplet for the case of symmetric heating of the substrate, (b) snapshot of the particle deposition pattern

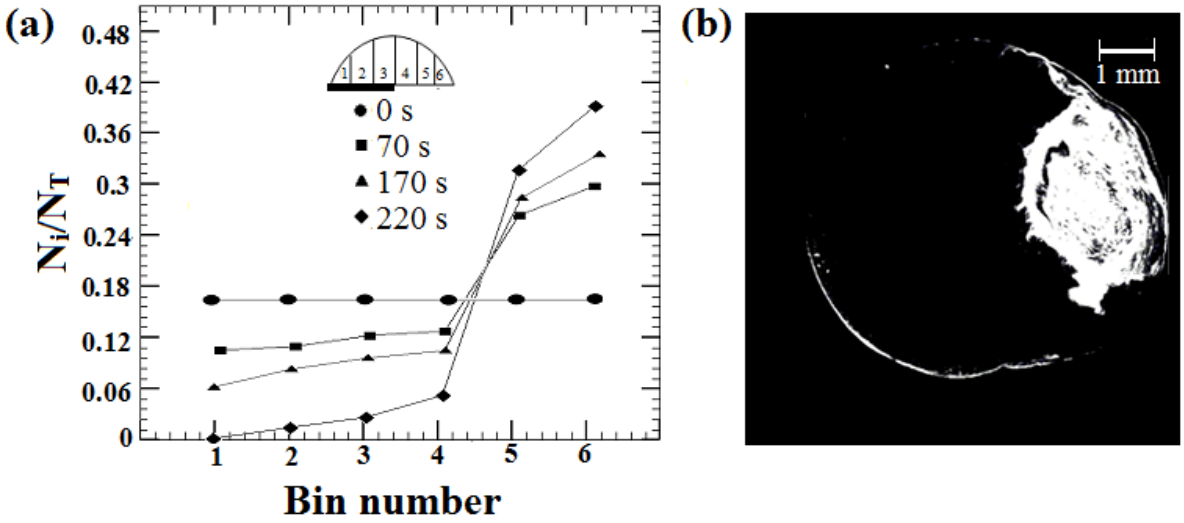


**Figure 2.23.** (a) Concentration profile of particles inside the evaporating droplet for the case of asymmetric heating of the substrate (TL>TR), (b) snapshot of the particle deposition pattern

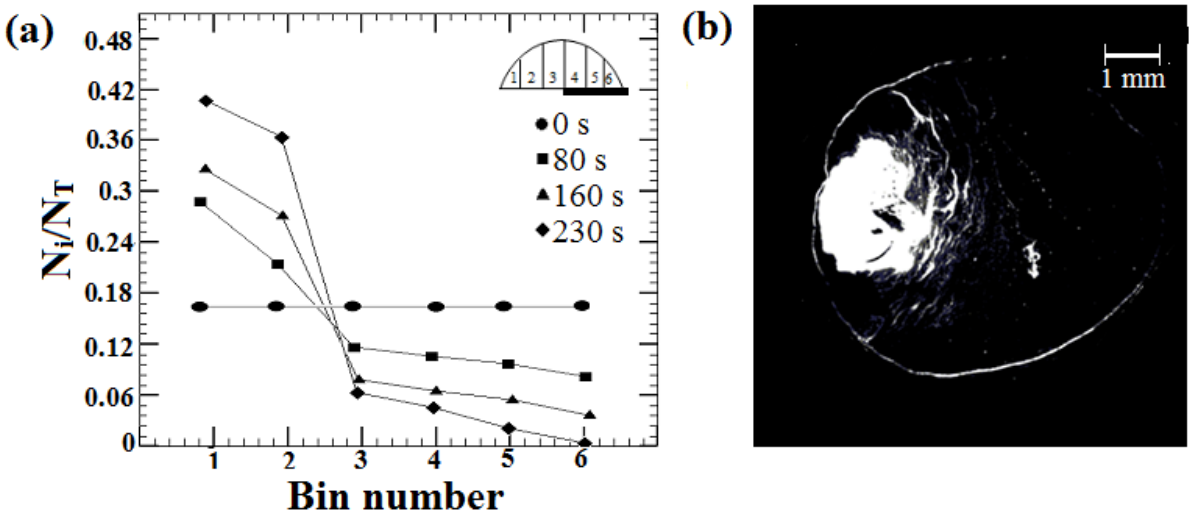


**Figure 2.24.** (a) Concentration profile of particles inside the evaporating droplet for the case of asymmetric heating of the substrate (TL<TR), (b) snapshot of the particle deposition pattern.

## 2.4.5 Effect of particle concentration

To understand the effect of dispersed particle concentration on the fluid motion inside the evaporating droplet, the experimental investigations were carried out on droplets with four different polystyrene particle concentrations. The particle concentrations considered during these experimental investigations were 3%, 5%, 8% and 12%. These experiments were carried out in ambient condition. Figure 2.25 shows the velocity field inside the evaporating droplet containing 3% polystyrene s recorded at two different time instant. As expected, the measured temperature at the edges is lower than the apex temperature of the droplet. This temperature gradient results two symmetric and counter rotating convection inside the evaporating droplet as described in Figure 2.12. Similar velocity fields were also observed inside the droplet with particle concentration of 5 %, 8 % and 12 %. However, the magnitude of the velocity decreases as the particles concentration increases. This can be seen from the velocity fields shown in figures 2.26-2.28. This is expected during the experiment because as the concentration of particles increases, the liquid viscosity increases. As a result, the magnitude of velocity inside the droplet decreases. Overall these appears to be no qualitative change in the internal circulations.

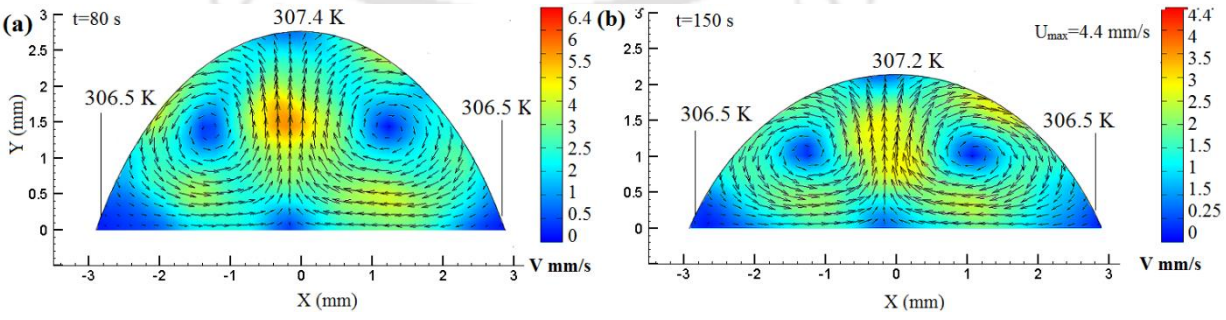


**Figure 2.25.** Velocity vectors superimposed over velocity field contour colored by its magnitude during evaporation of droplet containing 3% polystyrene particles recorded at (a) 80 s (b) 150 s respectively.

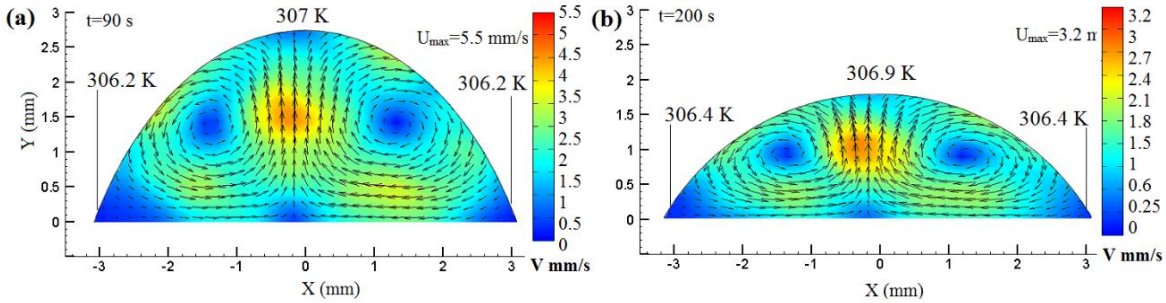


**Figure 2.26.** Velocity vectors superimposed over velocity field contour colored by its magnitude during evaporation of droplet containing 5% polystyrene particles recorded at (a) 90 s (b) 200 s respectively.

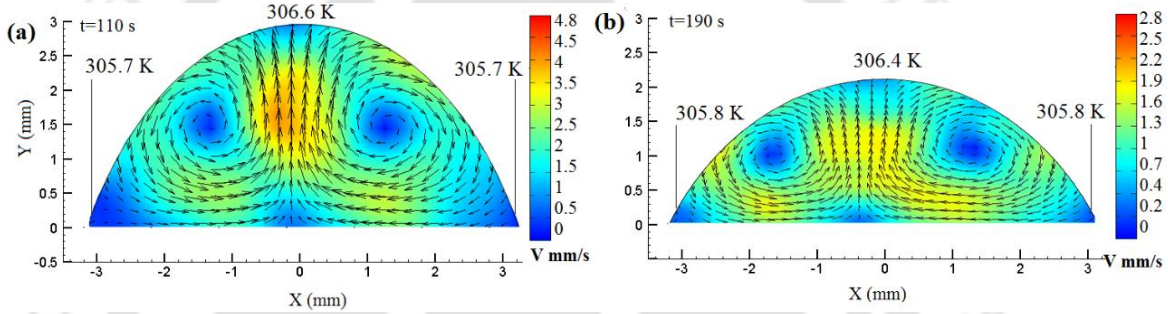


**Figure 2.27.** Velocity vectors superimposed over velocity field contour colored by its magnitude during evaporation of droplet containing 8% polystyrene particles recorded at 110 s (b) 190 s respectively.

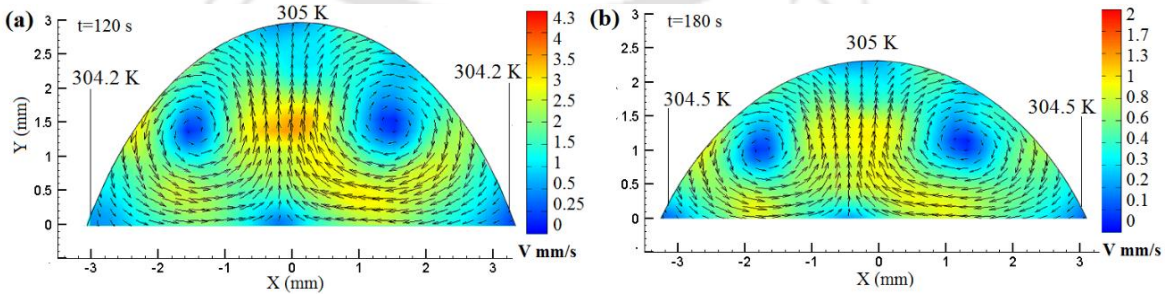


**Figure 2.28.** Velocity vectors superimposed over velocity field contour colored by its magnitude during evaporation of droplet containing 12% polystyrene particles recorded at 120 s (b) 180 s respectively.

## 2.5 Conclusion

This work demonstrates that the formation of a coffee ring like structure can be suppressed by the external heating of an evaporating droplet. The velocity field and particle concentration inside the evaporating droplet of water containing dispersed polystyrene particles were measured by the PIV technique. The contact line of the droplet remains pinned throughout the process and the particle deposition pattern on the substrate was found to depend on the direction of the internal fluid flow. Isolation of Marangoni convection is impossible within the system. As a result, the computational strategy allowed the advantage to investigate the fluid motion without considering the Marangoni stress along the droplet interface. The strength of the fluid flow driven by the Marangoni stress is dominant over the buoyancy flow inside the evaporating droplet. The velocity fields computed from steady state simulations were in qualitative good agreement with the experimental observations. The predictions of final particle deposition are also in good agreement with the observed deposition pattern obtained from a 3D evaporating droplet. This simple technique can be used in controlling the coffee ring structure in many applications.

# CHAPTER 3

# Microdroplet evaporation with surface heating

## 3.1 Introduction

In the previous chapter, we reported the velocity field and particle concentration profile for evaporating droplet placed on a heated substrate. It was found that externally heated substrate modifies the surface temperature gradient along the droplet interface, which affects the fluid flow pattern and therefore the deposition pattern formation in the evaporating droplet containing polystyrene particle. The contact line was observed to remain pinned throughout the evaporation process. Some recent studied have shown that the coffee ring can be suppressed by electrowetting (Eral *et al.*, 2011; Mampallil *et al.*, 2011) and external heating of the droplet such as laser (Putam *et al.*, 2012), infrared radiation (Thokchom *et al.*, 2014). Eral *et al.*, (2011) demonstrate that the mobilization of contact line of the droplet of colloidal suspension can be achieved by applying an AC voltage between the integrated electrodes suppressing the coffee ring. Recently, Thokchom *et al.* (2014) reported that the external heating of the droplet free surface using infrared radiation controls the particle deposition pattern. They demonstrated that the liquid droplet heated by infrared radiation heating modifies the surface temperature gradient which affects the fluid flow patterns inside the droplet and finally the particle

deposition pattern. The contact line remains pinned throughout the process and the particle transport was found to depend on the direction of the fluid motion inside the evaporating droplet. To explore the effect of external heating of the liquid droplet in detail, the investigation was conducted on the heated droplet at the top free surface using a wire like heating element. Flow visualization experiments were used to determine the flow field and particle transport inside the evaporating droplet. In this study, two cases of external heating at the drop free surface were considered. In one of the study, the droplet placed on a substrate was heated at the top by the heating wire element whereas in the other case, the droplet was heated at the left of the droplet free surface near the contact line. Numerical investigation was also performed to determine the internal fluid flow pattern inside an evaporating droplet.

## 3.2 Experimental procedure

In the previous chapter, the liquid microdroplet was placed on the externally heated substrate. In this work, the confined 2D droplet is externally heated at the droplet free surface using thin needle like heating element as shown in Figure 3.1. Figure 3.1a shows the droplet surface heated at the top. Using a microsyringe, a liquid water droplet dispersed with 10 µm polystyrene was confined in between two transparent hydrophobic surfaces placed on substrate. This heating element was inserted at the top of the droplet as shown in Figure 3.1a. The diameter of the heating element was 100 µm. The temperature of the heating element was regulated by the voltage controller. Similarly, Figure 3.1b shows the droplet heated near the left edge of the droplet. The temperature was measured at the edges, apex and substrate using K-type thermocouples. The images of the droplet during the process were captured by CCD camera. From these images, the velocity field

and average particle density were determined.

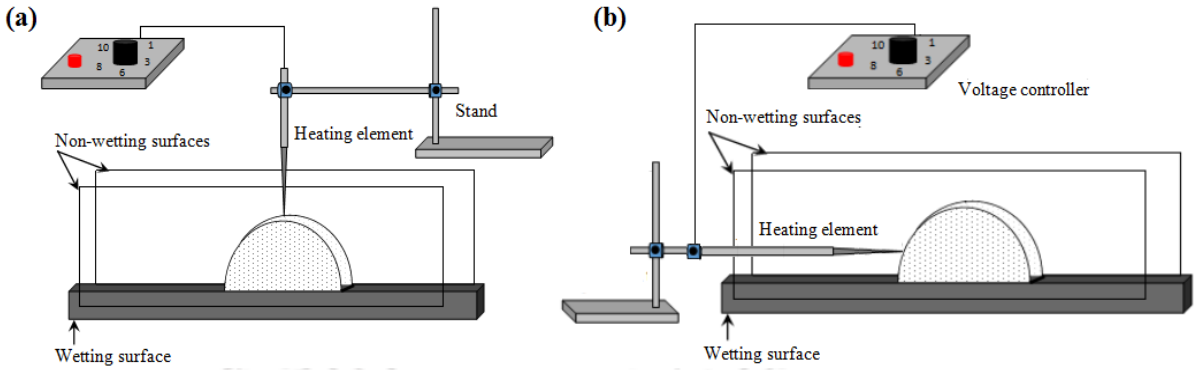


**Figure 3.1.** Schematic diagram of localized heating of the droplet. (a) Localized heating at the apex of the droplet, (b) localized heating at the left side of the droplet.

## 3.3 Results and discussion

### 3.2.1 Analysis of contact line

Figure 3.2a shows the plot of the diameter of contact line with time for two cases of surface heating of the droplet. In this plot, the diameter of contact line at any time ($d_i$) is normalized by the initial diameter of the droplet ($d_o$) and evaporation time t is normalized by the total drying time $t_o$. The initial diameters of the droplet for these two cases were 5.76 mm and 5.8 mm. It can be observed that the contact line of the droplet is change with time. The droplet subjected to localize heating at the apex was found to decrease with time. This can also be seen from the images provided in Figure 3.2b. In another experiment, the heating element was inserted in the droplet near its base (left side). In this case, the contact line diameter of the droplet was found to increase with time. It was noticed that the right side of the contact line was pinned throughout the evaporation process, but the left side (near the heating element) gradually expanded making the droplet asymmetric. This can be more apparent from the images included in Figures 3.2c.

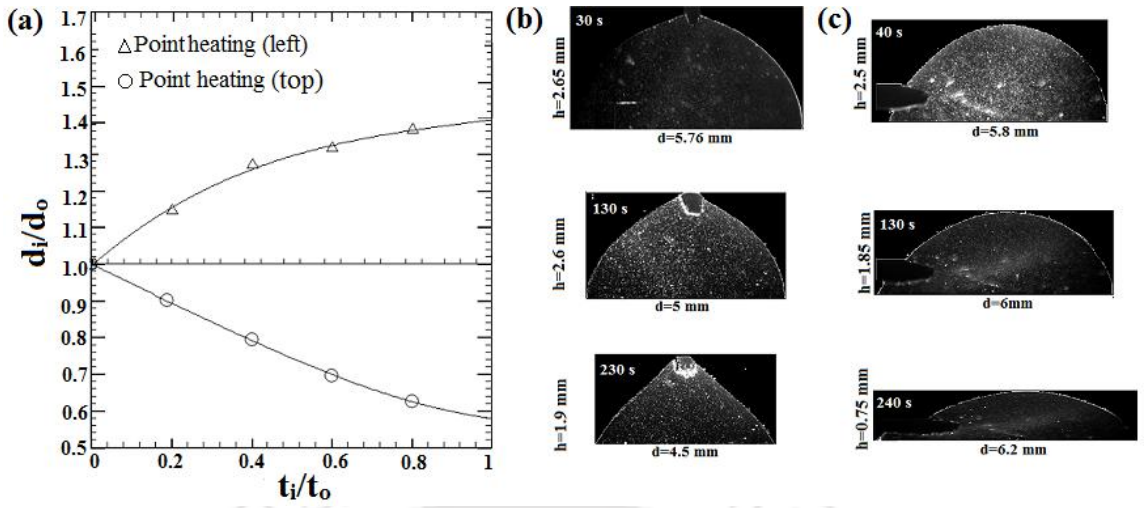


**Figure 3.2.** (a) Time evolution of contact line of the droplet normalized by the initial diameter. The photograph of the evaporating droplet at various stages: (b) top heating (c) left heating.

Figure 3.3a demonstrate the change of contact line with time. The depth of the tip of the element at the apex of the droplet was ~0.4mm. Initially, the tip of the heating element was found to stick with the droplet free surface. This is due to adhesion force between the heating element with the liquid of the droplet. The evaporation flux will be maximum at the heating point. This maximum evaporation rate and attraction of the tip of the heating element with the droplet interface, causes the droplet to shrink toward the center of the droplet. As the size of droplet reduces with time, the tendency of droplet surface is to free from the tip of the heating element. At time t=220 s, the height of the tip was controlled such that the detachment of droplet from the heating element is avoided.

In contrast to heating of the droplet at the apex, the contact line of the evaporating droplet subjected to localize left heating of the droplet was found to increase with the time. Figure 3.3b illustrates the evaporating droplet heated at the left. In this case, the forces due to interfacial tension at the contact line are expected to be imbalanced due to localize heating causing the droplet contact line to expand near the left. These interfacial forces are

illustrated in Figure 3.3c. The balanced interfacial forces at the the contact line can be expressed by the Young's equation,

$$\Upsilon_{SV} - \Upsilon_{SL} = \Upsilon_{LV} \cos\theta \qquad (3.1)$$

where $\Upsilon_{SV}$, $\Upsilon_{SL}$ and $\Upsilon_{LV}$ respectively are the surface forces of the solid/vapor, solid/liquid and liquid/vapor interfaces at the contact. When the droplet surface is heated at the left, the interfacial force of the liquid/vapor i.e. $\Upsilon_{LV}$ at the contact line decreases. This will imbalance the equilibrium at the contact line as described in Eqn. 3.1. In order to keep the forces in equilibrium at the contact line the contact angle of the droplet reduces, causing the droplet to flatten there. This may lead to expand the contact line with time (See Figure 3.2b).

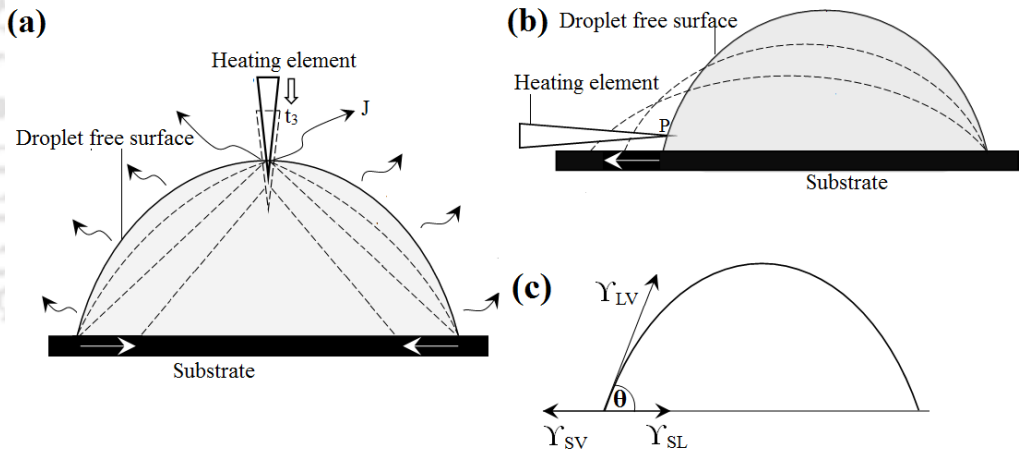


**Figure 3.3.** Schematic diagram shows the working mechanism of localized heating of the droplet free surface (a) Point heating at the apex of the droplet; (b) Point heating at the left side of the droplet and (c) The interfacial forces at the contact line of the droplet.

### 3.2.2 Velocity profile

In this section, the velocity fields inside the evaporating droplet subjected to different conditions mentioned in the previous section are discussed. Figure 3.4a shows the velocity vector superimposed on the velocity contour obtained from the experiments with top

heating. The initial height of the droplet was 2.76 mm. The temperatures at various points on the droplet free surface are also shown in figure. As expected, the measured temperature at the apex was higher than that of edge. This surface temperature gradient will create a surface tension gradient along the droplet interface. The gradient in surface tension will set up Marangoni convection carrying the fluid from the apex towards the edge along the air-liquid interface. Recirculation pattern is similar to the case of evaporation under ambient condition. The velocity fields at later stages of the evaporation are also provided in Figures 3.4 (b-d). The velocity vectors superimposed over the velocity contour obtained from the simulations corresponding to this geometry is shown in the right column of Figure 3.4. The results from the numerical simulation are observed to be in qualitative agreement with the experimental results. The direction of velocity field shown in Figure 3.4h is different from the experimental observation at time 220s. This is expected because the momentum flux driven by mass loss near the edge was not considered in the numerical simulation.

Figure 3.5 shows velocity fields for the droplet heated on the left side. The velocity fields from the experiments are given in the left column of the figure.The initial height of the droplet was 2.8 mm. In this case, the droplet temperature at the left edge is higher than the apex and right edge. The temperature on the free surface decreases monotonically from left to the right. Consequently, the surface tension gradient is created along the droplet surface with right edge having the higher value than the left edge. The value of surface tension at the apex will lie between that of left and right edge. The resulting Marangoni stress will drive the fluid towards the right edge creating a convection cell in the clockwise direction. As expected, in this case there is only single convection cell inside the evaporating droplet. Recirculation flow pattern is same as that of a droplet with left half-

heated substrate except that the contact line was found to be unpinned during the process. The figure on the right column shows the velocity field at various stage of evaporation obtained from simulations. Again, the simulation results are observed to be in qualitative agreement with the experiments.

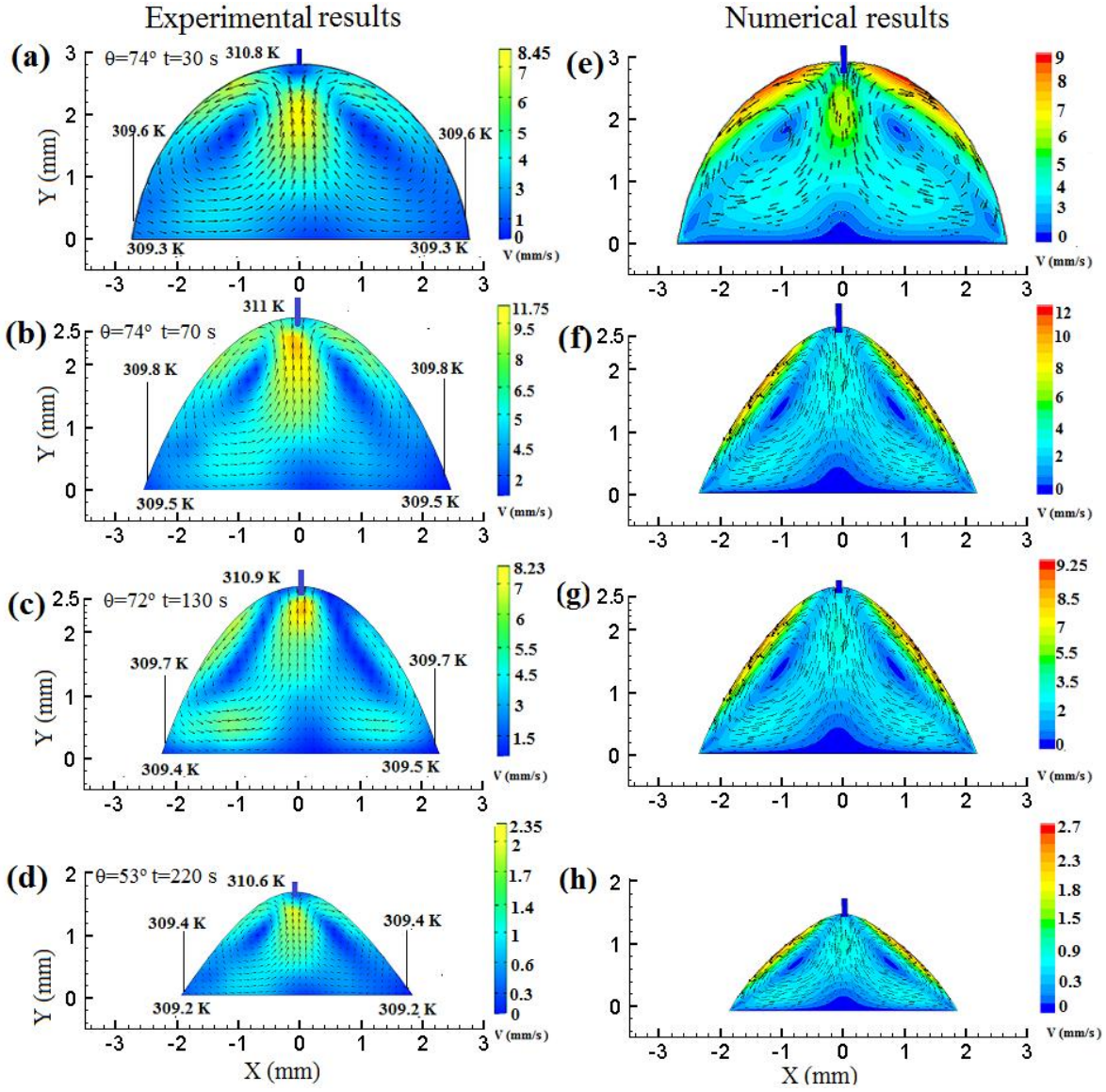


**Figure 3.4.** Experimental velocity vectors superimposed over velocity field contour colored by its magnitude during evaporation of droplet placed on the substrate in the case of localized heating at the apex after recorded at (a) 70 s; (b) 130 s; (c) 180 s and (d) 220 s. The right column (e-h) shows the corresponding velocity vectors and contour map obtained from numerical simulation.

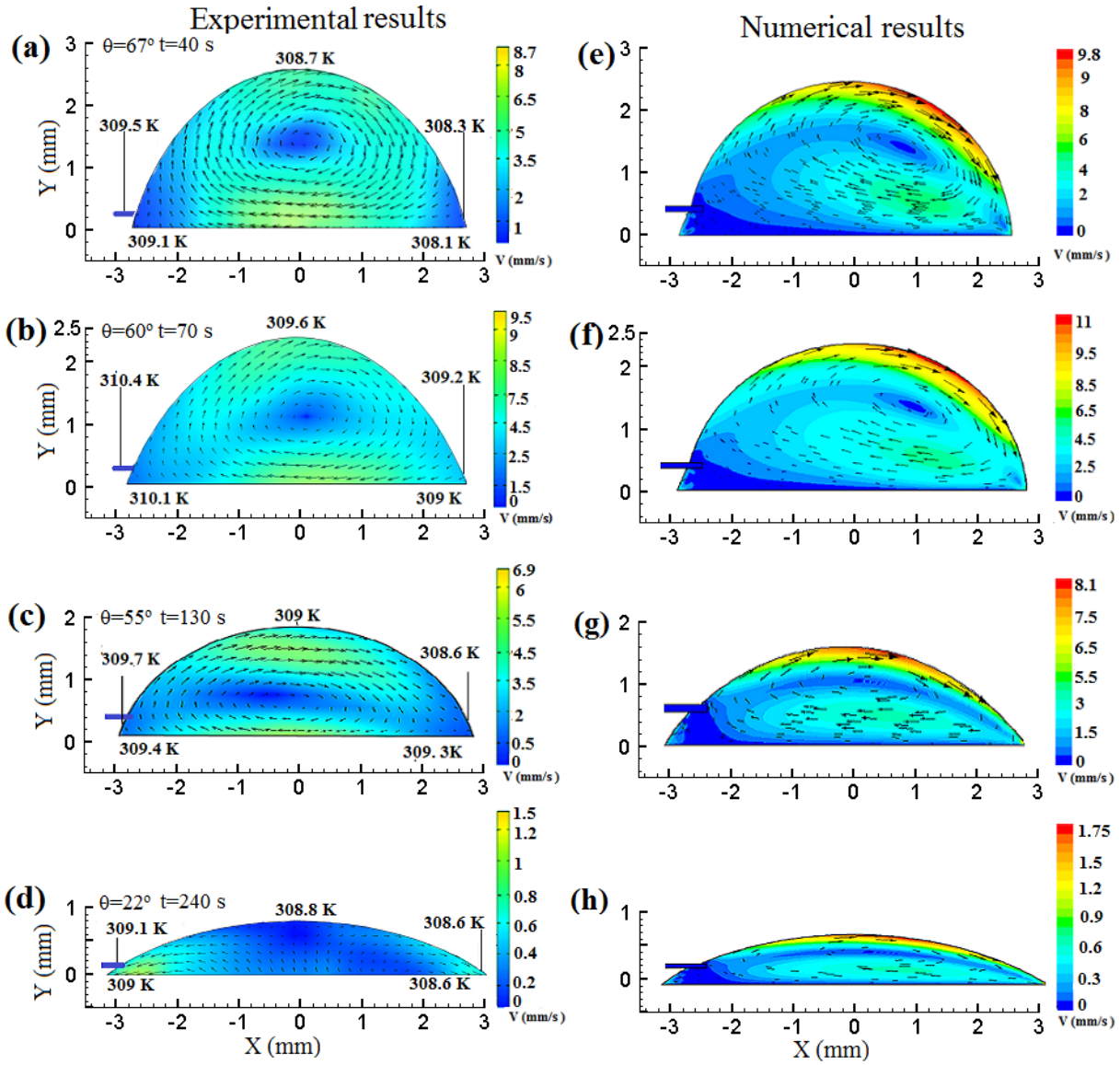


**Figure 3.5.** Experimental velocity vectors superimposed over velocity field contour colored by its magnitude during evaporation of droplet placed on the substrate for the case of localized heating at the left after recorded at (a) 70 s; (b) 130 s; (c) 190 s and (d) 240 s. The right column (e-h) shows the corresponding velocity vectors and contour map obtained from numerical simulation.

### 3.2.3 Particle concentration profile and pattern formation

In this section, the particle concentration inside the droplet for two different cases described in the previous section is discussed. The number of particles inside the bins was

counted and tagged by using a particle tracking program in Matlab as described in the Chapter 2. The normalized particle density ($N_i/N_T$) is plotted against the bin number which is shown in Figure 3.6. Figure 3.6a shows the particle distribution inside the bins for the case of top heating of the droplet. In this case, the direction of the convection was same as that of the droplet evaporating in ambient condition. However, the particle distributions inside the concentration bins are quite different. The reason for this opposite behavior is due to de-pinned contact line. We had discussed in the previous sections that introducing the heating element at the top introduces another contact point there. To compensate the loss of mass due to evaporation the contact line of the droplet with the bottom substrate recedes with time. This causes the dispersed particles to accumulate towards the center. Therefore, the particles distribution inside the central bins (2-5) is found to increase with time whereas the particles near the edges (1, 6) decreases with time. The dispersed particles are expected to be deposited at the center upon complete evaporation. In Figure 3.6b, we have shown the evolution of particle concentration profile for the case of left heating of the droplet. It can be observed that the particle concentration in the left bins (1-2) increased whereas the particles in the right bins (3-6) decreased with time. The solute present inside the droplet is expected to deposite more on the heating side.

To verify the prediction of deposition pattern, the image of the particles left on the substrate after the complete drying of 3D droplet was taken to observe the nature of deposition pattern. Figure 3.7a shows the image of the particle deposition pattern after complete drying when the droplet was heated at the top. As expected, the particles are deposited more at the center. A thin ring like structure is due to the fact that some of the particles might have been deposited during the early pinned contact line of the droplet since in this case the velocity profile predicted downward flow near the edges causing

some of the particles to plunge downward and get deposited there. Figure 3.6b shows the image of the deposition pattern from the case of left heating. From the image of polystyrene particles left after complete evaporation we found that the pattern is shifted towards the left. The observed pattern is in agreement with the predictions of velocity field for these cases. These results show that the final deposition pattern of particles from complete evaporation of a droplet can be altered by the internal circulation within the droplet which itself can be controlled by the temperature profile on the surface.

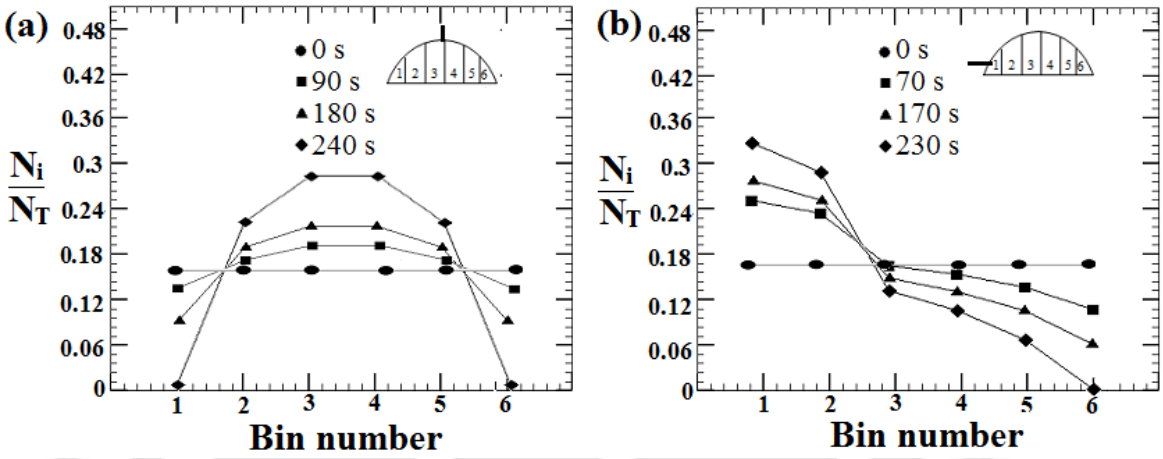


**Figure 3.6.** Particles concentration profile in an evaporating droplet subjected to localize heating. (a) Localized heating at the top, (b) Localized heating at the left side.

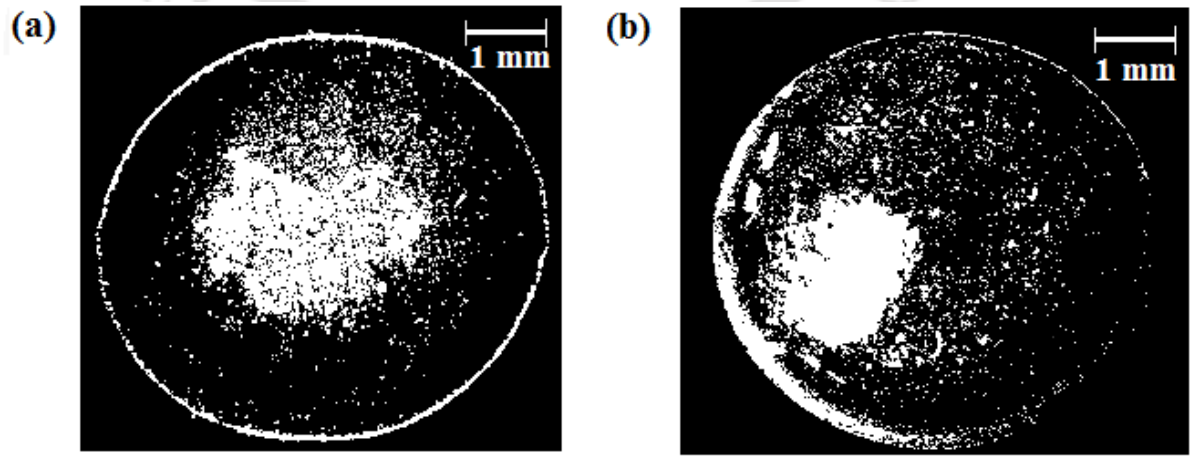


**Figure 3.7.** Particles deposition pattern after complete drying of droplet. (a) Localized heating at the top, (b) localized heating at the left side.

## 3.4 Conclusion

This work demonstrated that coffee ring formation can also be suppressed by the external heating of the droplet free surface. Two symmetric convection cells were observed during evaporation of droplet subjected to top heating of the droplet while a single cell was observed when the droplet was heated at the left side of the droplet. On other hand, concentration dynamics were found to be strongly influenced by the contact line of the droplet. The prediction of deposition pattern from velocity fields and concentration profiles obtained from the experiments were found to be true when then the dried out pattern was observed. The results computed from the numerical simulations were in qualitative good agreement with the experimental observation. Our study has provided a detailed insight into the velocity field, concentration profile and particle deposition pattern, which can be used in various applications employing evaporation based droplet micro-fluidics.

# CHAPTER 4

# Flow reversal in evaporating droplets on heated substrates

## 4.1 Introduction

In the previous two chapters, we have shown that the surface temperature gradient generates the Marangoni convection and strongly affects the deposition pattern of drying drops. Despite this, the significance of temperature profile and resulting fluid motion inside the droplet are yet to be completely understood. A number of experimental and theoretical studies have tried to explain the surface temperature in an evaporating droplet. Most of the previous studies believed that the temperature is lowestt near the contact line and surface temperature profile monotonically increases from the edges to the apex of the droplet (Deegan *et al.*, 2000, Steinchen and Sefiane, 2005). Theoretical predictions and infrared topographic observation showed that the surface temperature monotonically decreases from the edge to the top of the droplet (Ristenpart *et al.*, 2007; Xu *et al.*, 2010; Girard *et al.*, 2010). Numerical simulation by Hu and Larson (2006) predicted that the direction of surface temperature profile reverses at the critical contact angle of the droplet. Further, Ristenpart *et al.* (2007) and Xu *et al.* (2010) reported that temperature distribution along the droplet interface depends upon the relative thermal conductivity of the substrate

and liquid as well as the height of the droplet. Recent studies by Zhang *et al.* (2014) reported that uniform surface temperature distribution for all the conditions of evaporation is not reasonable and a nonmonotonic surface temperature profile may exist during the transition period i.e. when the contact angle is near to the critical value. In this study, we have realized the nonmonotonic temperature variation along the droplet surface experimentally. The resulting fluid flow inside the droplet were studied using the tool of particle image velocimetry (PIV). Numerical simulations were also performed to determine the internal fluid flow inside the evaporating droplet for similar conditions that existed in the experiment. In this work, we demonstrate that the temperature distribution along the drop free surface can significantly influence the velocity field and consequently affects the particle distribution inside the evaporating droplet.

## 4.2 Experimental procedure

In this study, we are interested to see the temperature profile and resulting velocity field during the transition period between the initial stage and final stage of the evaporating droplet. The experimental setup shown in Figure 4.1a same as we described in Chapter 2. To understand the significance of surface temperature within the system, the temperature of the droplet was measured at various point using K-type thermocouple. The temperature was also measured at the apex ($T_a$); at the intermediate point ($T_i$); near the edge of the droplet ($T_e$) and the substrate temperature ($T_s$). Before the start of experiment, the substrate was heated for few minutes using heating element regulated by the voltage controller as shown in Figure 4.1b. As soon as the temperature of the substrate stabilized, the liquid droplet of 45 µl with 1% polystyrene tracer particle was placed on the warm substrate. The continuous images taken from the CCD camera were stored in 680 x 512 pixels, 12-bit

gray scale format on a PC via frame grabber. These images were used for analysis of the contact angle, velocity field, and concentration of particles inside the evaporating droplet.

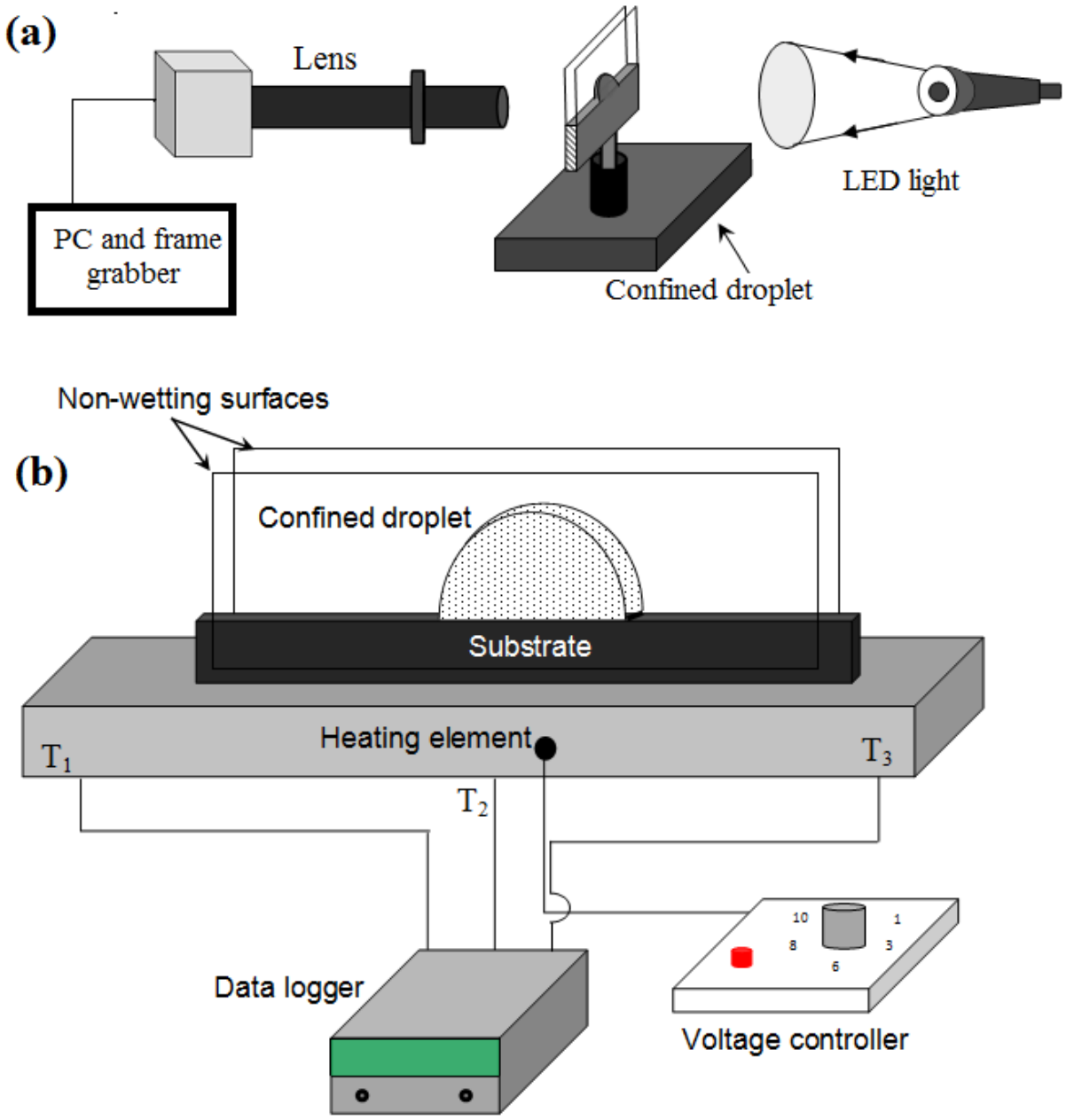


**Figure 4.1.** (a) Schematic diagram of experimental setup. (b) Schematic diagram of confined 2D droplet placed on heated substrate. $T_1$, $T_2$, $T_3$ are the thermocouples.

## 4.3 Results and Discussion

### 4.2.1 Temperature profile

In this section, the surface temperature distribution of drying droplet placed on heated surface is discussed. The droplet remains pinned on the wetting substrate throughout the process (see Figure 4.2). Figure 4.3 shows the plot of temperature against radius of the droplet (R). It can be observed that the surface temperature profile changes its direction as the evaporation progress. Four states of temperature profile are observed: (i) at 30 s, the edge temperature is higher than the apex temperature and the surface temperature profile increases monotonically from the center to the edge of the droplet; (ii) at 110 s, the temperature exhibits a nonmonotonic profile: it first increases and then decreases from the top to the edge of the droplet; (iii) at 170 s, the edges temperature is lower than the apex temperature and the temperature profile decreases monotonically from the top of the droplet to the edge; (iv) at 220 s, the surface temperature profile is nearly constant. To understand the temperature profile along the droplet interface, it is reasonable to think in terms of relative influences of evaporative effect and conduction path from the substrate to the droplet free surface. As the evaporation process proceeds, the evaporative cooling reduces the temperature along the surface of the droplet. To compensate the heat loss and to maintain the necessary temperature for evaporation, the heat transfer due to conduction take place from the substrate to the droplet free surface. Hence, the temperature distribution is defined by two factors: evaporative cooling along the droplet interface and the heat conduction from the substrate to the surface of the droplet (Zhang et al., 2014). When the liquid droplet is placed on the warm plate, the bottom temperature of the droplet will be higher than the temperature at the top surface of the droplet. Moreover, the contact

angle of the droplet is large and thermal conductivity of the substrate is 16 W/m.K. This may also enhance the heat transfer due to conduction from the substrate to the top surface of the droplet. Thus, the edge temperature is higher than the apex temperature at t= 30 s. Ristenpart et al. (2007) and Zhang et al. (2014) predicted similar temperature profile. As the evaporation progresses, the evaporative cooling along the interface of the droplet continues to reduce the temperature along the droplet interface. A coupling between the heat transfer due to conduction and that of evaporative cooling effect may induce thermal stratification along the surface of the droplet. Hence, the surface temperature is nonmonotonic at the transition period. When the contact angle is small, the cooling effect due to nonuniform evaporation along the droplet interface may be predominant over the heat transfer due to conduction within the process. Thus, the temperature decreases monotonically from the top to the edge of the droplet at time 170 s. The result is not consistent with a theory proposed by Ristenpart *et al.* (2007). This clearly indicated that the droplet placed on a substrate with finite thickness temperature not only depends on the thermal conductivity but also on the height of the droplet. Our observation is similar to the prediction of Xu et al. (2010) and Zhang *et al.* (2014). As the evaporation progress, the contact angle reduces and the droplet will behaves like a thin film and the heat fluxes along the droplet surface will be equivalent. Therefore, the measured temperature at all the points is nearly equal at t= 220 s.

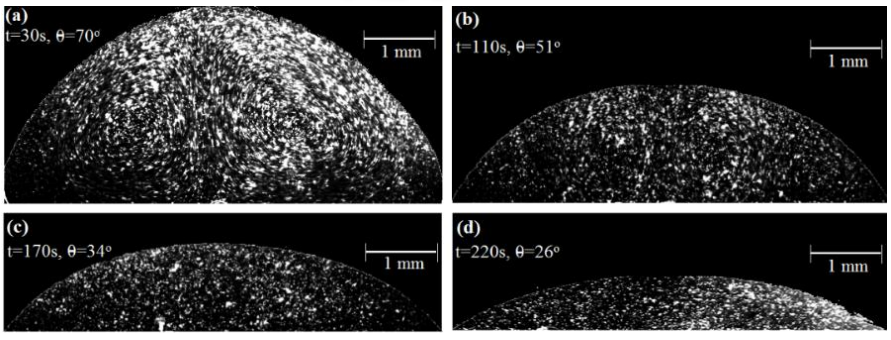


**Figure 4.2.** Time sequence of the images of the droplet captured by the CCD camera.

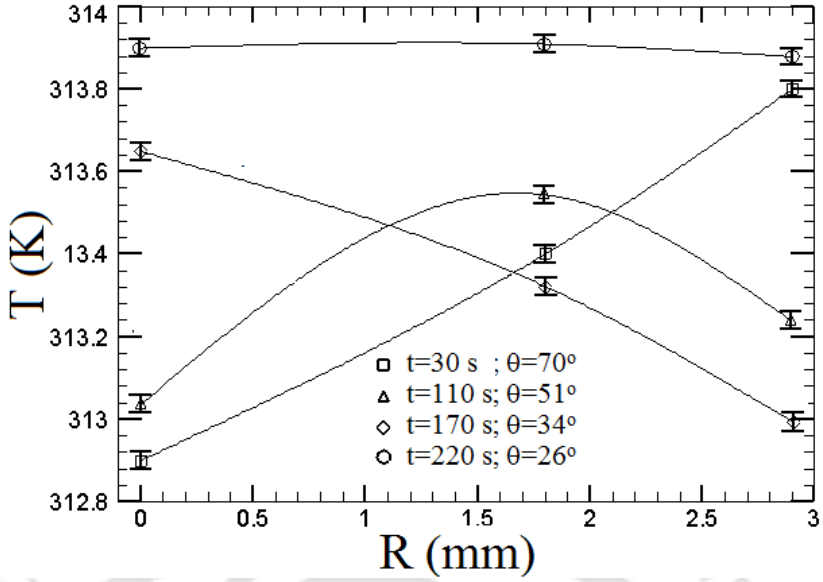


**Figure 4.3.** Surface temperature distribution at various times of the evaporating droplet.

### 4.2.2 Velocity profile

In the previous section, the surface temperature profile and its dependence on by the conduction path as well as evaporative cooling was discussed. In this section, the fluid motion inside the evaporating droplet is described. Four distinct flow patterns corresponding to the temperature profile in Figure 4.3 were observed as shown in Figure 4.4. Two symmetric counter rotating convection cells inside the evaporating droplet were observed at t= 30 s. The structure of the fluid flow inside the droplet can be explained by the Marangoni stress due to nonuniform temperature distribution along the droplet free surface. It was noticed that the temperature at the edge was higher than the apex temperature of the droplet. The surface tension will be weak near the edge but strong at the top of the droplet. As a result, surface tension will drive the fluid from the edge towards the apex along the surface of the droplet. This generates recirculation of two counters rotating convection cells inside the evaporating droplet. At t= 110 s four convection cells were observed. This is attributed to nonmonotonic temperature gradient along the droplet

surface described in the earlier section. Such temperature distribution creates a surface tension gradient, which is inward at the center and becomes outward in the outer region of the droplet interface. Thus, this nonmonotonic gradient in surface tension along the droplet interface will drive four vortices inside the droplet. Zhang *et al.* (2014) predicted similar velocity field inside the droplet through numerical simulation. We would like to mention that the criteria described by Xu et al. (2010) predicted the critical angle (corresponding to $K_R >> 2$) of $25^o$ at which flow direction would reverse. The direction of the Marangoni convection cells inside the evaporating droplet shown in Figure 4.4a was found to be reversed at t= 170 s. This observation is consistent with the prediction of Xu et al. (2010). However, it was noticed that the fluid flow is radially outward along the droplet surface and parallel to the substrate at 220 s. This is expected because the flow is strongly influenced by the maximum evaporation near the contact line as predicted by Deegan *et al*. (1997). Hence, the surface temperature distributions significantly influence the internal fluid flow patterns. Numerical simulations were also conducted for the steady state condition using the geometry and boundary condition obtained from the experiment. Figure 4.4(e-h) shows the velocity field obtained from the numerical simulation that correspond to the geometry described in Figure 4.4(a-d). The droplet interface was assigned a linear temperature profile between the edge temperature and the apex temperature of the droplet. The Marangoni stress was assigned to the interface of the droplet. Linear temperature profile between the edges temperature and no slip condition were assigned at the bottom surface. The results were in quantitative good agreement with the experimental observations. However, the velocity field obtained from the experimental result at t= 220 s was found to differ from the simulation result. As already mentioned, the primary reason is that the momentum transport resulting from the evaporation flux near the edges was not considered in the simulation. In addition, the temperature gradient and

subsequently Marangoni stress along the droplet interface were considered in the numerical simulation, which is expected to be small at the end of the process in the experiment.

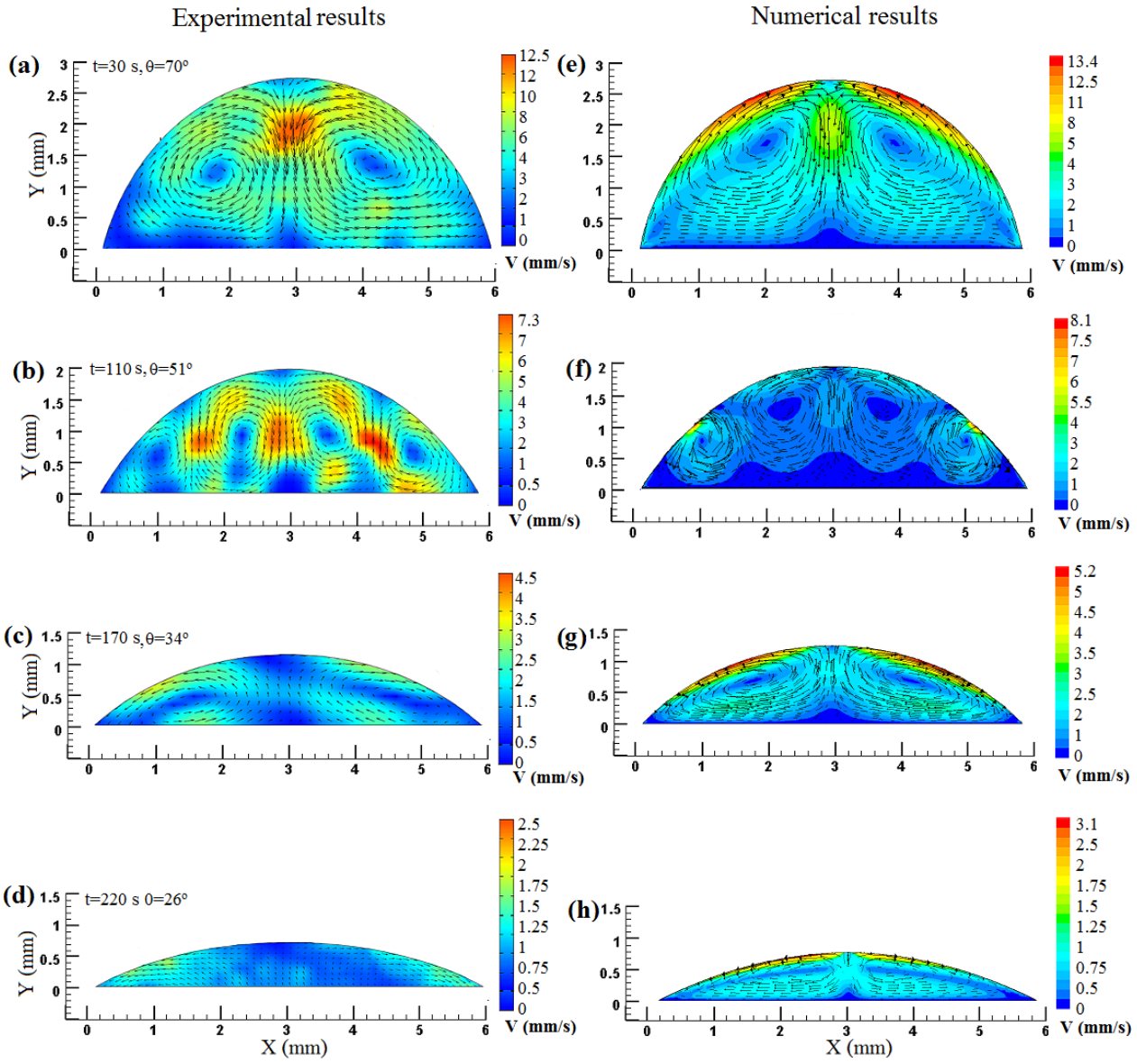


**Figure 4.4.** Velocity field at different stages of the droplet obtained from the experiment at (a) 30 s (b) 110 s (c) 170 s (d) 220. The right column (e-h) shows the corresponding velocity fields obtained from the Numerical simulations.

### 4.2.3 Concentration profile and particle deposition pattern

In this section, we describe the particle concentration inside the droplet at various stages of the evaporation process. To evaluate the normalized area averaged particle density ($N_i/N_T$) of solute particles the droplet is divided into 10 bins of equal width. The particle concentration ($N_i/N_T$) denotes the number of particles dispersed in a bin per unit area at any time ($N_i$) divided the total number of particles per unit area initially present in the droplet ($N_T$). The number of particles in the droplet was calculated using a particle tracking program in Matlab. It can be noticed from Figure 4.5a that the count of the particles inside the bins is nearly same at the initial stage of the process. As the evaporation proceeds, the convection leads to the change in the particle concentration inside the bins. At early time (t= 30 s, 120 s) the particle concentration within the central region (bins 4-7) increased whereas the particles near the edges (bins 1, 2, 9 and 10) decreased with time. This particle distribution is attributed to the velocity field described in Figure 4.4a. With the progress of time, the particle inside the bins near the edges bins (1, 2, 9 and 10) was found to increase whereas at the center bins (4-7) decreases. As expected the direction of fluid flow described in Figure 4.4c has effect on the concentration dynamic of the particle. As the evaporation progresses with more time, more and more particles concentrate near the edges. The evolution of concentration profile predicts a spot with ring like deposition pattern is expected after complete evaporation. To verify the prediction of deposition pattern inferred from the concentration profiles, experiments was conducted with drying 3D droplets. The image of the particles left after complete drying was taken to observe the nature of deposition pattern. It can be noticed from the image that the prediction of particle deposition pattern from the velocity field and concentration profile is true (see Figure 4.5b).

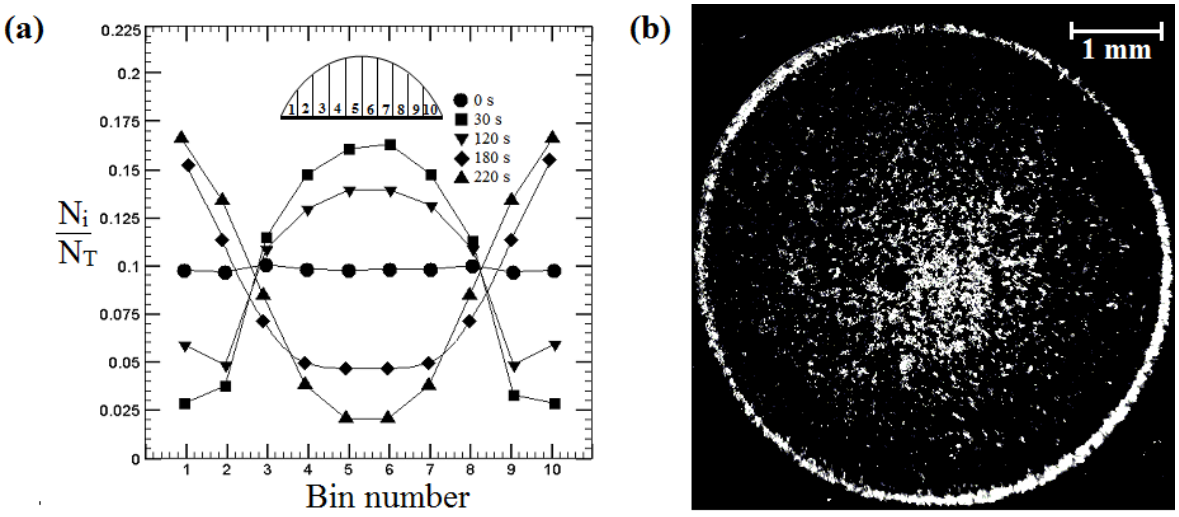


**Figure 4.5.** (a) Concentration profile inside the droplet at different times. (b) Snapshot of the particle deposition pattern.

## 4.4 Conclusion

Four distinct flow patterns were revealed inside the drop at different stages of the process. The flow pattern is significantly influenced by the surface temperature distribution of the evaporating drop. Two symmetric counter rotating flow patterns observed in the initial stages are driven by the monotonic temperature gradient which increases from the apex to the edge of the drop. The second stage shows four vortices inside the drop due to nonmotonic temperature distribution along the drop surface. The direction of flow pattern was reversed at the third stage where the temperature gradient is again monotonic but in opposite to the final case. The final stage is characterized by the radially outward flow toward the edge to replenish the evaporation loss. Velocity fields from simulation were observed to be in qualitative agreement with the experiment. The concentration profile and image of the particle deposition pattern clearly shows that the particle transport are strongly affected by the internal fluid flow.

CHAPTER 5

# Evaporation of bacterial suspension drops

## 5.1 Introduction

The particle deposition of evaporating droplet of biological suspension has attracted many researchers attention over the past few decades, as there is evidence that useful information can be extracted from the deposition pattern left on the substrate. In particularly, drying of human blood on a substrate in ambient condition result in unique structure in the solid phase. These unique structures can acts as biomarker that may reflect the health condition of a person. Therefore, this unique pattern has a potential to develop a simple and low cost technique for medical screening and diseases diagnosis.

Several research groups have reported that controlling this phenomenon is of great interest for the development of disease diagnostics in developing countries where resources are limited and infectious diseases such as malaria, HIV and tuberculosis are prevalent. (Semples *et al.* 2013, Sefiane *et al.* 2010). Burtin *et al.* (2010) has examined the resulting deposition pattern from drying drops of human blood of healthy, anemic and hyperlipidemic patient. They have reported that drying of human blood drop reveals uniqueness in pattern formation that reflects the health of the person and this can be used person (see Figure 5.1a). Wen *et al.* (2013) used the 'coffee ring effect' for rapid protein

detection and for characterization of the blood sample and as potential marker for disease diagnosis. They also reported that signal intensity arising from particle concentration due to the coffee ring effect on the hydrophobic surfaces was six fold higher than those on hydrophilic surfaces (see Figure 5.1b).Shabalin and Shatokhina (2007) have found that human tears, synovial fluid and urine additionally exhibited distinctive deposition pattern. Killen *et al.* (2006) ascertained the various deposition pattern left when complete evaporation of human blood from persons suffering from B cell disorder and multiple myeloma to those of healthy investigated the nature of the substrate that will enhance the particle concentration. Wong *et al.* (2011) have demonstrated the separation of different sized biomolecules at the edge line after complete evaporation of the droplet. The separation was based on a particle-size selection at the contact line in an evaporating droplet. Trantum *et al.* (2013, 2014) observed that the fluid flow caused by the Marangoni stress along the droplet interface causes the suspended particles to concentrate in a visually detectable spot which is vital in the disease diagnosis technique as shown in Figure 5.2a.

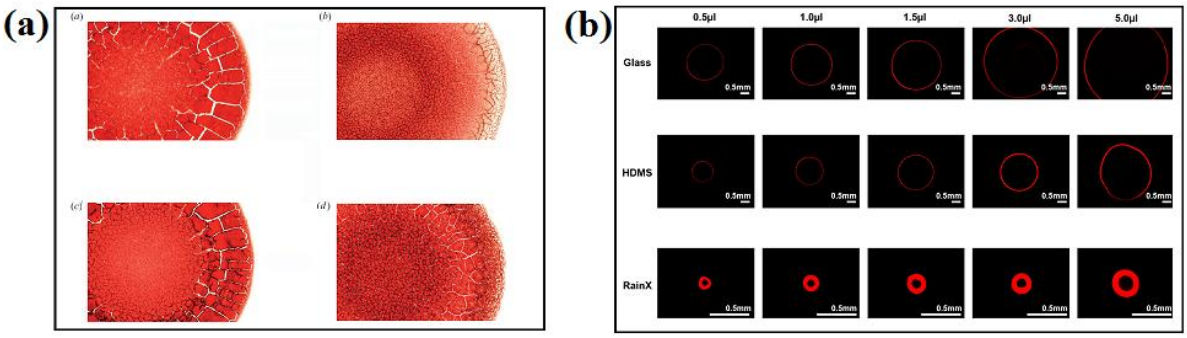


**Figure 5.1.** (a) Drying of blood drops from individuals (from Burtin *et al.* 2010, *J Fluid Mech*. 667:85-95. Copyright 2010 by the Copyright Cambridge University Press). (b) Florescent images of coffee ring on different substrate (from Wen *et al.* 2013, *Langmuir* 29, 8440−8446. Copyright 2013 by the American Chemical Society).

Evaporation of a liquid droplet of biological materials (virus, bacteria, and cells) could be a complicated process. Usually the suspended particles move with the inner fluid flow arising from temperature variation on the free surface of the evaporating droplet. However, in the case of evaporation of a droplet containing suspended bacteria, there is a possibility of interaction with other driving mechanism that may influence the fluid convection within the droplet. Tuval *et al.* (2005) explained that the interplay of chemotaxis and diffusion of nutrient can produce variety of deposition patterns. They observed the suspension of *Bacillus subtilis* forming the self-organized generation of a persistent hydrodynamic vortex that traps cells near the contact line. Nellimoottil *et al.* (2007) studied the deposition pattern in droplet of suspension of motile as well as non-motile bacteria. They observed uniform deposition pattern when the droplet containing suspension of motile bacteria dries out while a ring like stain was left after complete evaporation of the droplet containing suspended non-motile bacteria. They argued that uniform deposition pattern was due to motile bacteria moving against the convection which will produce a ring like structure. However, their work invited critical comments by Sommer and Zhu (2007) since the motion against the convection of the fluid can only happen when there is chemotaxis due to presence of nutrients within the droplet. Recently Semples *et al.* (2013) have conducted experiments to study 'coffee ring effect' in two types of droplets; one containing live *Pseudomonas aeruginosa* bacteria and other containing live *E. coli* bacteria. For the suspension of *P. aeruginosa* no coffee ring depositions were observed whereas *E. coli* suspension showed dense deposits of bacteria near the contact line. *P. aeruginosa* bacteria are known to auto-produce rhamnolipids, which are strong biosurfactants. In contrast, a homogeneous deposition of the bacteria, concentrated at the contact line was obtained when a knock-out mutant, unable to produce biosurfactants, was added to the suspension of *P. aeruginosa* bacteria. They have also

conducted experiments to study the role of non-ionic surfactants (Triton X-100) on the dynamics of *E. coli* systems during drying and it was observed that in the presence of surfactants, the dynamics changed dramatically. Based on these experiments they speculated that the presence of auto-produced biosurfactant induces Marangoni stresses that reverse the outward capillary flow, leading to a homogeneous distribution of the bacteria upon drying as shown in Figure 5.2b.

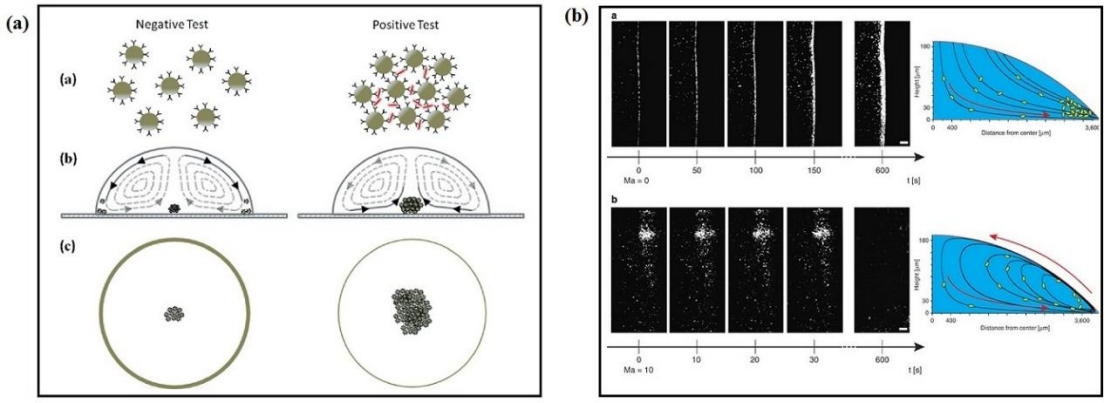


**Figure 5.2.** (a) Schematic diagram of particle transported by the Marangoni flow and final deposition pattern of an evaporating droplet (from Trantum *et al.* 2014, *Lab Chip* **14**, 315-324. Copyright 2014 by the Royal Society of Chemistry). (b) Internal fluid flow of an evaporating droplet of *E-coli* was observed in the absence (above image) and in the presence of Triton X-100 (below image). (From Semples *et al.* 2013, *Nat. Commun.* **4**, 1757. Copyright 2013 by the Nature Publishing Group).

Quantitative visualization of fluid flow inside the evaporating droplet provides the information about transportation of particles during the evaporation process. Subsequent studies have shown that secondary flows caused by direct and indirect effects of the non-uniform evaporation rate (Hu and Larson, 2006; Thokchom *et al*. 2014; Ristenpart *et al*., 2007). However, the internal fluid flow pattern as described above may be disturbed when there is strong influence of chemotaxis created by introducing a chemoattractant like a

sugar crystal at the base of the droplet (see Figure 5.3a). Chemotaxis refers to directed swimming motion of bacteria using its flagellar motors towards a nutrient site (Darnton *et al*. 2007; Wadhams *et al*. 2004) as shown in Figure 5.3b. Recent investigations have shed light on the signal transduction events that occur inside *E. coli* cells during chemotaxis Sagawa *et al*. (2014). Our objectives in this work are to understand how the internal fluid flow, particle transport and the particle deposition pattern of the evaporating droplet of bacterial suspension are affected in the presence and absence of chemotaxis

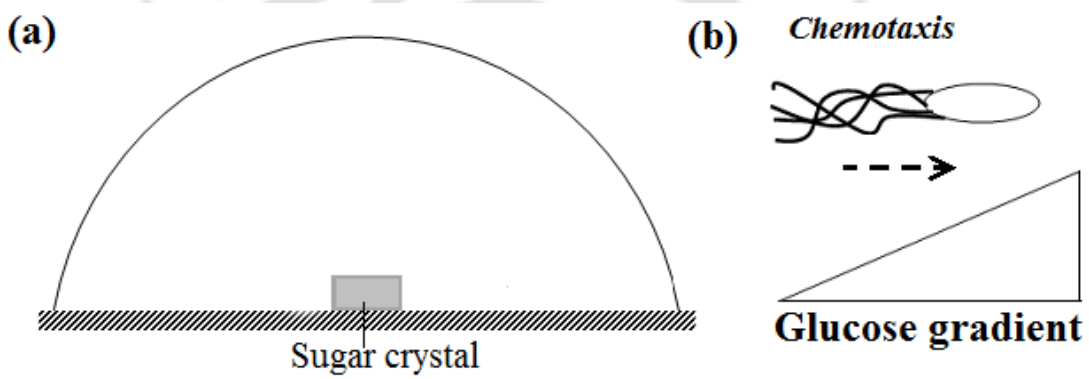


**Figure 5.3.** (a) Droplet of bacterial suspension with a sugar crystal on the substrate (d) Schematic representation of chemotaxis in *E.coli*

## 5.2 Experimental details

### 5.2.1 Preparation of biological tracers

*Escherichia coli* bacteria (DH5α strain) were used as biological tracers in our experimental studies. *E. coli* bacteria (previously transformed to express Green. Floures cent Protein, GFP) was grown in Luria-Bertani (LB) (HiMedia, Mumbai, India) medium containing ampicillin, incubated in a shaker (180 rpm) at 37$^{o}$C for 4—6 hours The employed to enable imaging of bacteria with a CCD camera. The recombinant green

fluorescence protein (GFP) expressing *E. coli* was generated by cloning the GFP gene into an ampicillin-resistant pUC-derived plasmid vector (Gogoi *et al* 2001). We also prepared the suspension of dead bacteria by keeping aside some quantity of above sample for more than a week at room temperature (25-30 $^{o}$C), so that the all suspended bacteria would have died.

### 5.2.2 Experimental procedure

The PIV experimental setup as already described in Chapter-2 was used to determine the velocity field and particle transport inside the evaporation droplet except the biological tracers. The experiments were conducted in air conditioned room whose temperature was maintained at 24$^{o}$C. The relative humidity range for all our experiments varied between 30 and 40%. The droplet containing suspended microorganisms was visualized by LED light and the images were recorded by a CCD camera (PixFly Hires from PCO) of 1360 ×1024 pixel resolution in conjugation with a zoom lens (Navitar). The images were recorded at the speed of 19 images $s^{-1}$ and stored in a computer for PIV analysis.

## 5.3 Results and discussion

### 5.3.1 Velocity profile

In this section, we describe the velocity field inside the droplet of bacterial suspension subjected to different experimental conditions. No polystyrene particles were added in these experiments. First, we discuss the experimental results for the case when the droplet of live bacterial suspension was evaporated with no sugar at surface using a syringe inserted in the gap between two non-wetting surfaces. As the droplet detached from the syringe, it spread in the form of half disc-shape sandwiched between the two non-wetting

surfaces. The contact line of the droplet was observed to be pinned to the bottom substrate during the evaporation process. Soon the motion of suspended particles was observed and the CCD camera recorded the images. Velocity field was computed from these images at various stages of evaporation..Figures 5.4a and 5.4b shows the velocity vectors superimposed over the velocity contour after 30 s and 1330 s of evaporation where recirculation of two symmetric convection cells can be clearly observed. In an evaporating droplet placed on solid substrate the rate of evaporation is maximum near the edges. This creates a temperature gradient along the droplet surface. Since the surface tension of liquids is a function of temperature, a surface tension gradient is created along the free surface. As a result the free surface experiences Marangoni stresses, thus pulling the liquid towards the region of high surface tension along the free surface. This sets up fluid circulations inside the droplet. The circulation patterns as shown above are very similar to the observations of Kang *et al.* (2004) and Jaijus and Singh (2010) with suspension of polystyrene particles. However, the direction of circulation is different than those reported in the simulations of Hu and Larson (2006). Ritsenpart *et al.* (2007) using asymptotic analyses have shown that the direction of circulation depends both on the contact angle and ratio of the thermal conductivities of the substrate and liquid ($K_R$). For evaporating liquid droplet placed on a flat substrate the evaporation flux is largest near the contact line which results into highest heat flux there. If the substrate has large thermal conductivity then the energy is readily supplied to the edge regions which have shortest conduction path. This helps the contact line to maintain a comparatively high temperature (compared to the top) despite the energy lost due to evaporation. This will create Marangoni flow radially inward along the liquid-air interface, but radially outward along the liquid-substrate interface. On the other hand, the substrates with low thermal conductivity are unable to readily provide the energy. As a result the more energy is extracted from the

liquid drop. Since the rate of evaporation is highest near the edges the drop is coldest there. The resulting Marangoni flow will be directed radially outward along the liquid-air interface, and radially inward along the liquid-substrate interface. The theoretical analysis (supported by experimental observations) of Ristenpart *et al.* (2007) have shown that for $K_R > 2$ the Marangoni flow is directed radially outward along the substrate whereas for $1.45 < K_R < 2$, the flow direction depends on the value of contact angle, and for $K_R < 1.45$ the circulation direction is radially inward along the substrate. The thermal conductivities of water, glass and metal substrate (stainless steel) used in our experiments can be taken as 0.58, 1.05 and 16 respectively. If it were an unconfined 3D droplet the ratio of thermal conductivity of metal substrate and liquid ($K_R \sim 27.5$) would predict radially outward flow along the liquid-substrate interface. However, in our experiments with droplet confined between two glass plates the contact area of the liquid with bottom substrate is only a small fraction of the area in contact with the glass plates. Therefore it is the conductivity of the glass plate which has greater influence on the droplet temperature compared to the metal substrate. The $K_R$ value in this case would be 1.8 (neglecting the very thin layer of Teflon). The low thermal conductivity of glass plate will help to maintain the drop to be coldest near the edge and hence, the direction of flow will be radially outward along the air-liquid interface as observed in our experiments. Therefore, our observations are in agreement with the findings of Ristenpart *et al.* (2007) We would like to mention that Ristenpart *et al.* (2007) predicted the critical angle (corresponding to $K_R = 1.8$) of $15^o$ at which flow direction would reverse. Hu and Larson (2006) carried our numerical simulation for water droplet on glass surface and observed that the Marangoni number changes at contact angle of $14^o$ reversing the direction of circulation. We wanted to verify this in our experiments but it was observed that when the contact angle decreased to low values, there were few dispersed particles (since most of the particles are already deposited ) making the finding

of correlation peaks erroneous and hence it was not possible to get correct velocity vectors at the current concentration of particles. In our experiments we could not carry out PIV analysis for droplet contact angle below $18^{o}$. However, it was noticed that when the droplet height reduced the Marangoni circulation disappeared and mostly radially outward flow along the substrate was observed (Figure 5.4c). To understand the effect of temperature gradient on the direction of convection cells we have conducted an experiment in which thin wire (K-type) thermocouples were used to measure the temperature of the apex and edge of the droplet. For evaporating droplet under ambient conditions (as is the case with all our experiments reported here) the temperature at the apex was measured to be $26.5^{o}$C, the edges were at $26.1^{o}$C and the direction of Marangoni flow was radially outward.

In the next step, we conducted experiments in the presence of bacterial chemoattractant in the form of sugar crystal placed on the center of the substrate. The size of cube shaped sugar crystal was 0.7mm. It was observed that the velocity fields inside the droplet were comparatively different from the previous case. The live bacteria were observed to move towards the nutrient site. This can be noticed from the velocity vectors recorded at 110 s and 950 s and are shown in Figures 5.5a and 5.5b, respectively. The circulation patterns are not only reversed but it can also be noticed that the velocity vectors near the sugar crystal are all directed towards it. The circulation patterns were also found to be asymmetric. As the evaporation progresses the sugar crystal gradually dissolves in the fluid. At a later stage (t = 1200 s) it was noticed that the sugar was completely dissolved. The Marangoni circulations disappear and motion was observed to be radially outward (Figure 5.5c). This is expected since the surface temperature gradient for a thin drop becomes small enough to generate Marangoni flow. The velocity pattern at this stage is qualitatively similar to that with live or dead bacteria in the absence of sugar. This

indicates that the concentration gradient of sugar disappears and chemotaxis stops. Figure 5.6 shows the snapshots of droplet with sugar at different time intervals. When sugar crystal was placed on the bottom of the substrate we noticed that the crystal completely dissolved in the medium by 1000 s. Therefore it is expected that as long as sugar crystal remained at the substrate the concentration gradient would have existed which drives the chemotaxis. From the knowledge of diffusivity of sugar in water it is possible to estimate the time of diffusion. The internal circulation observed in our experiments is expected to enhance the transport of sugar molecules away from the sugar crystal. This could be the reason for the absence of chemotaxis after the complete dissolution of sugar since the internal circulations would have created uniform concentration of dissolved sugar throughout the drop. In the absence of any concentration gradient the bacteria faithfully follow the fluid streamlines. In order to verify that the sugar crystal does not change the hydrodynamics of internal circulation but only the motion of live bacteria, we conducted experiments with dead bacteria as tracer particles. Figure 5.5d illustrates the velocity field inside the droplet of suspension of dead bacteria recorded at 90 s. Figure 5.5e shows the velocity field after 900 s when the height of the droplet reduced to 1.4 mm from 2.8 mm. During this time the volume of the sugar crystal also reduced to 80% of the initial volume. We observe two counteracting rotating velocity fields as described in the earlier case (Figures 5.5a and 5.5b) and in contrast to velocity fields observed with live bacteria in presence of sugar (Figures 5.4a and 5.5b). This is because dead bacteria do not display chemotaxis. Figures 5.5f shows the velocity field at 1000 s when the sugar crystal is completely dissolved. As expected the velocity field is similar to the case in Figure 5.3c. The medium used in the experiments was different from the experiments with polystyrene particles (i.e. water). The viscosity of the medium in which bacteria were suspended was

much higher than the water which was the continuous phase for experiments with polystyrene particles. This is the reason for order of magnitude difference in the velocity.

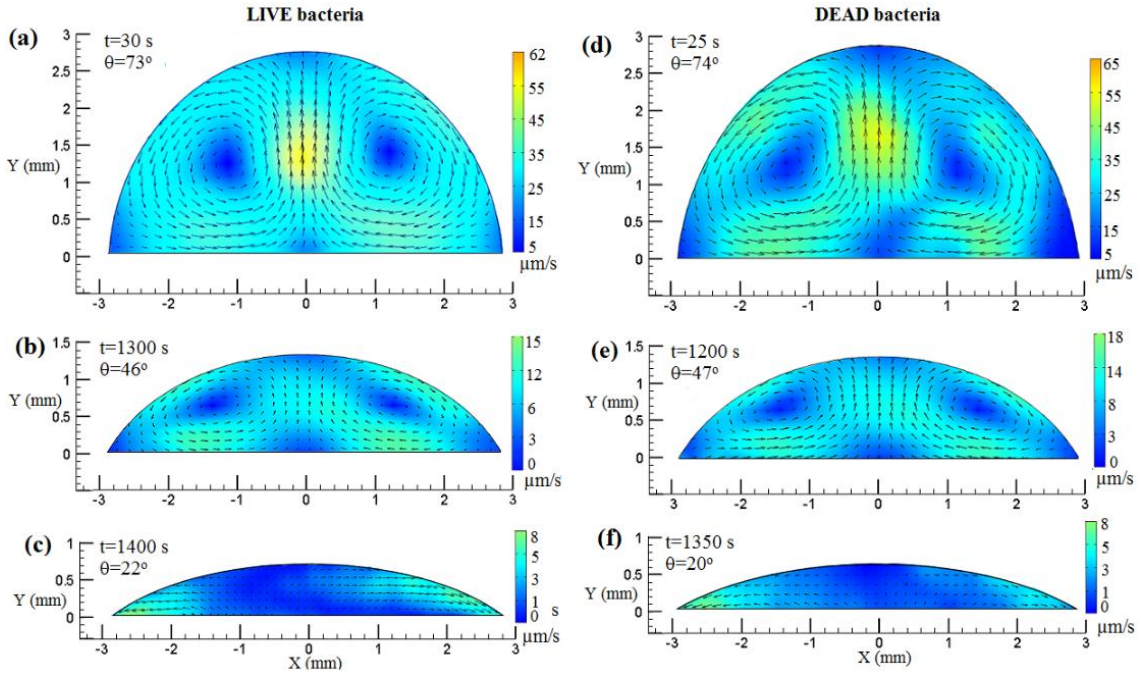


**Figure 5.4.** Velocity vectors superimposed over velocity contour colored by the velocity magnitude for the case of evaporating droplet containing suspension of live bacteria recorded at (a) 30 s (b) 1300 s and (c) 1400 s. The corresponding velocity fields inside the evaporating droplet with suspension of dead bacteria recorded at (e) 25 s, (d) 1200 s and (f) 1350 s.

To verify that the chemotaxis alone plays an important role in deposition pattern, we have performed additional experiments with droplet of live bacterial suspension in the presence of a metal block of size equivalent to sugar crystal employed. The velocity fields are shown in Figures 5.8. We observed that the velocity fields were different when compared with the case of sugar crystal. This shows that chemotaxis plays an important role in suppression of the coffee ring formation. The object (sugar crystal or metal block) is also expected to introduce small disturbance in the internal flow. The PIV analysis in

our experiments was carried out by considering interrogation windows of 128×128 pixels. In order to capture the disturbance close to the object we tried to analyze the PIV images by considering smaller interrogation windows (64×64 pixels) but this resulted into wrong velocity vectors. Cross correlation with smaller interrogation windows requires higher particle density but it was noticed that at higher concentration the suspension was turbid and quality of images were not suitable for PIV analysis. Another problem arose from the reflection of light from the object which makes the evaluation of velocity vectors close to the object difficult.

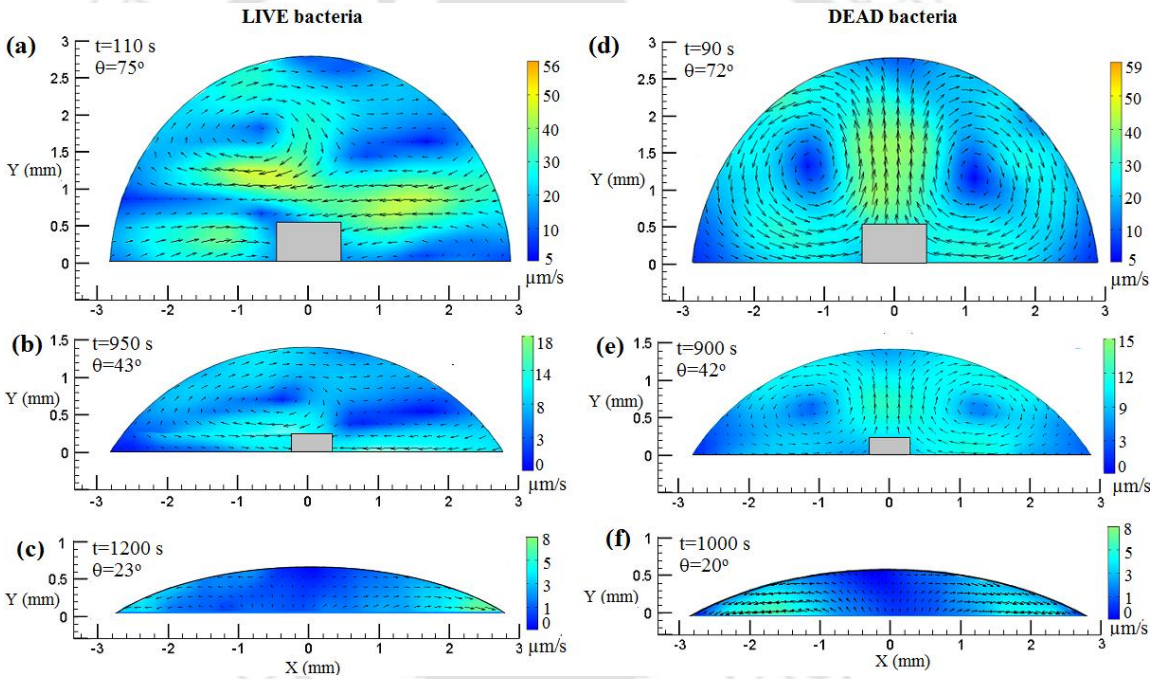


**Figure 5.5.** Velocity vectors superimposed over velocity contour colored by the velocity magnitude for the case of evaporating droplet containing suspension of live bacteria recorded at (a) 110 s, (b) 950 s and (c) 1200 s and when the sugar is at the center (represented by a rectangle in figure). The corresponding velocity fields inside the evaporating droplet containing suspension of dead bacteria recorded at (d) 90 s, (e) 900 s and (f) 1000 s when the sugar is at the center.

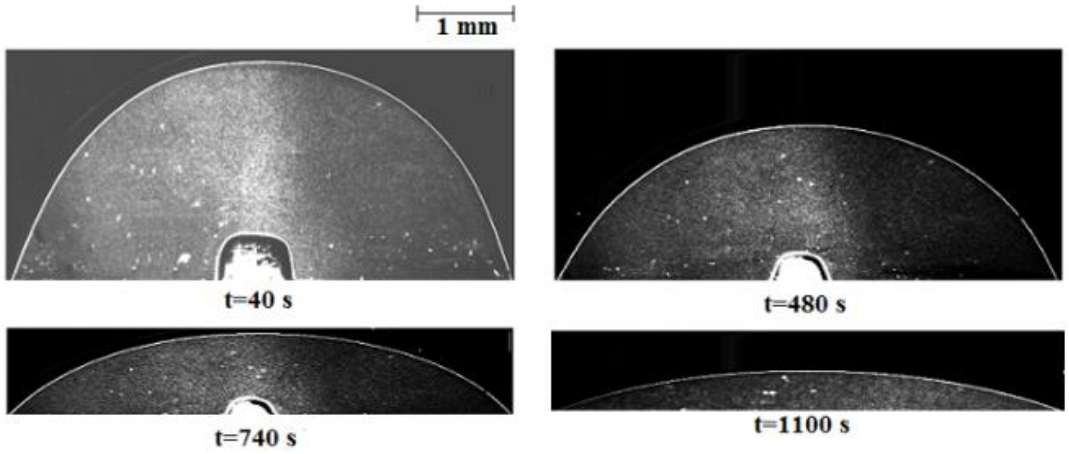


**Figure 5.6.** Snapshot of the evaporating droplet with sugar at the center

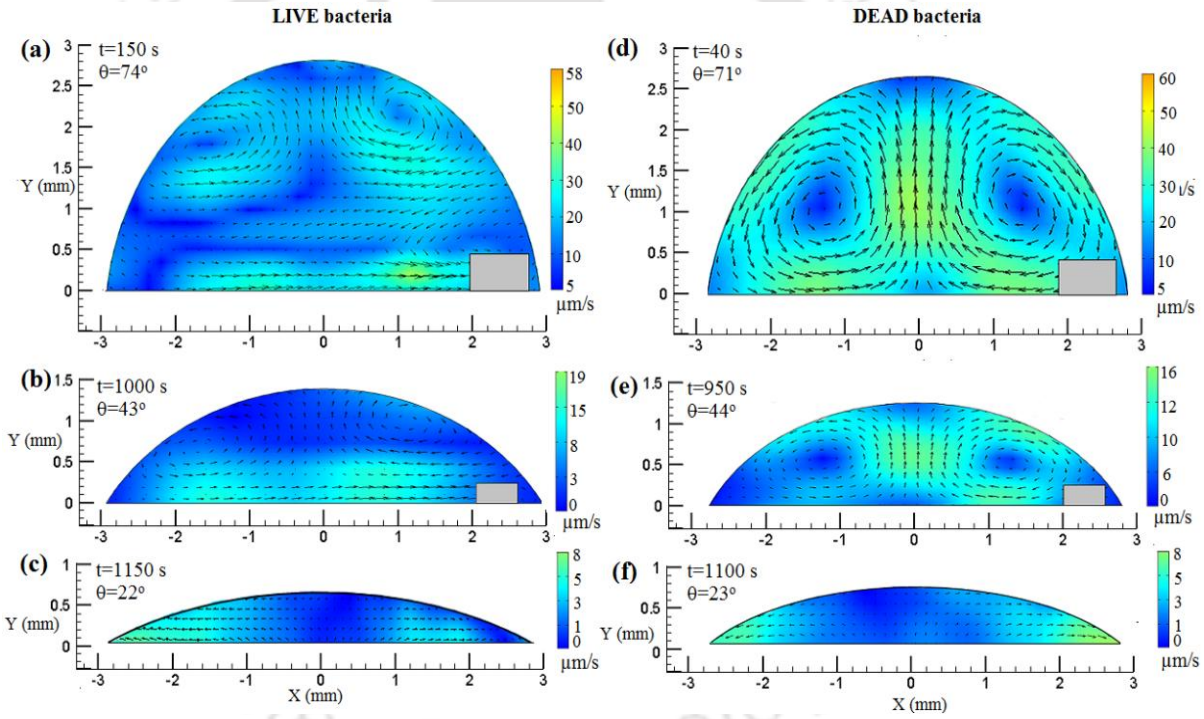


**Figure 5.7.** Velocity vectors superimposed over velocity contour colored by the velocity magnitude for the case of evaporating droplet containing suspension of live bacteria recorded at (a) 150 s, (b) 1000 s and (c) 1150 s when is sugar on the right side of the droplet. The corresponding velocity fields inside the evaporating droplet containing suspension of dead bacteria recorded at (d) 40 s, (e) 950 s and (f) 1100 s.

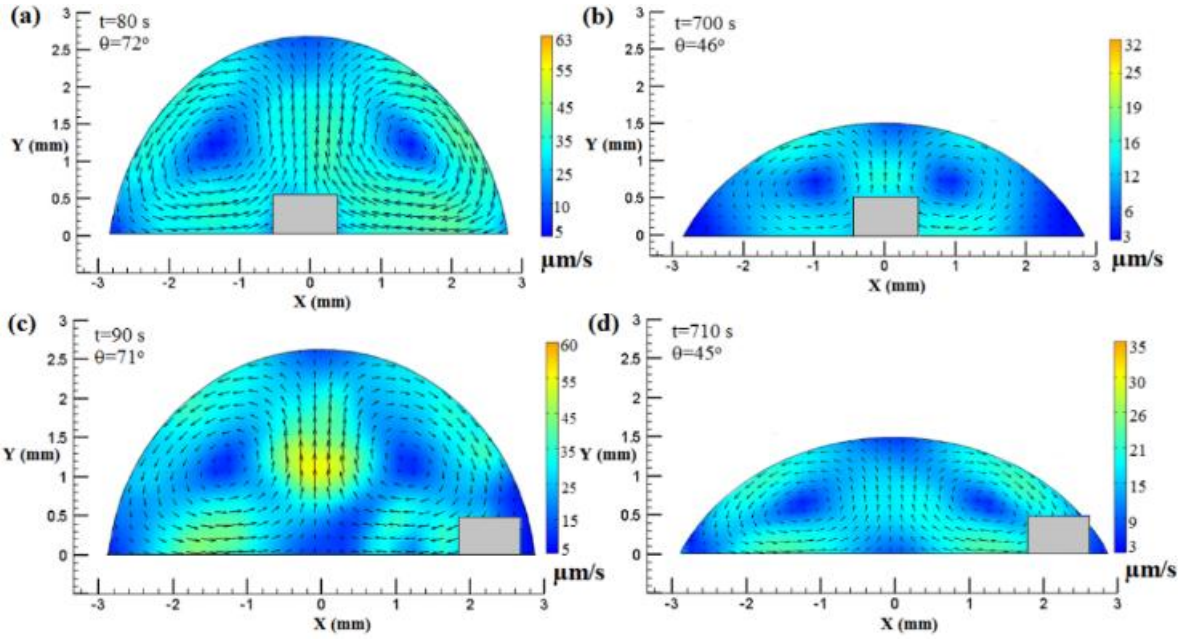


**Figure 5.8.** Velocity vectors superimposed over velocity contour colored by the velocity magnitude for the case ofevaporating droplet containing suspension of bacteria recorded at different times: (a-b) When the metal block at the center (c-d) When the metal block at the right. The aspect ratio of these images has been changed for the clarity of the velocity vectors.

## 5.3.2 Concentration profile

To understand the evolution of concentration profile of bacteria, the images of the droplet were divided into 10 bins of equal width as shown in Figure 5.9. The number of particles in the droplet was counted using a particle tracking program based on the intensity value of pixels in the raw images. In gray scale format the intensity of images ranges from 0 to 255. The average pixel size of particles in the images was 1 pixel. In the particle counting code any pixel with intensity between 150 and 255 was counted as one particle. This way all the particles were tagged and counted. The concentration of bacterial suspension ($N_i$ /$N_T$) denotes the number of particles in a bin per unit area at any time ($N_i$) divided by the

total number of particles per unit area initially present in the droplet ($N_T$). It is likely that the algorithm was unable to count some of the particles resulting from improper illumination. This can introduce a small error in particle count but it is not expected to alter the particle count qualitatively.

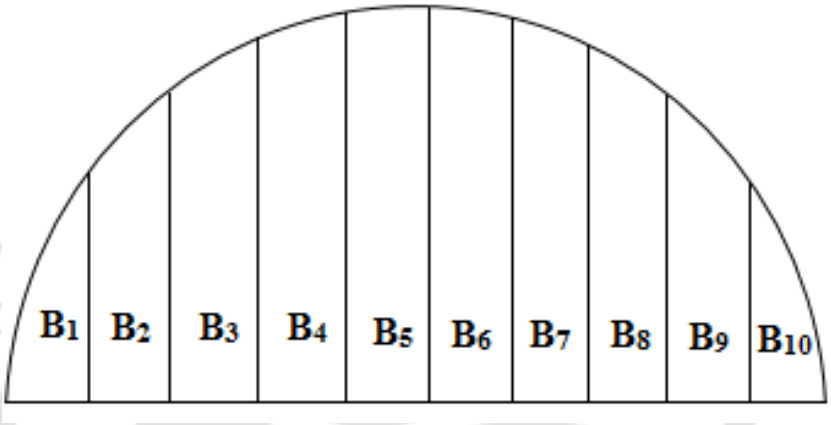


**Figure 5.9.** Schematic diagram of concentration bin of the droplet

Figure 5.10 shows the concentration profile of bacteria during early and late stage of evaporation. Figure 5.10a shows the concentration profile of live bacterial suspension whereas Figure 5.8b shows that of dead ones. In both the cases there was no nutrient placed on the substrate. It can be noticed that during the early time, the concentration of the bacteria inside all the bins are nearly same. As the evaporation progresses there is change in the concentration. The concentration of the live bacteria inside the bins (1, 2, 9 and 10) which are near the edges increases whereas the concentration of the central bins (3-8) decreases with time. This trend is observed in both the figures since the dynamics of live and dead bacteria are not significantly different in the absence of nutrient. The evolution of concentration profile suggests that a ring like pattern will be formed after complete evaporation of the droplet. Figure 5.10c shows the concentration profiles for the suspension of live bacteria when sugar crystal on the substrate was placed at its center. In

this case it can be observed that the concentration in the central bins (4-7) increases with time while the concentration inside the bins near the edges decreases with time. This is attributed to bacterial chemotaxis as described earlier in the section on the velocity field. With the progress of time more and more bacteria concentrate near the center of the drop where the highest concentration gradient of sugar exists. Therefore, a spot like deposition at the center is expected after complete evaporation. In case of droplet of suspension of dead bacteria in the presence of sugar crystal (Figure 5.10d) the dynamics are very similar to that observed in Figures 5.10a and 5.10b (in the absence of sugar crystal).

Figure 5.10e shows the concentration profiles of live bacteria when sugar on the substrate was placed on the right side of the droplet. We observed that the concentration in bins on the left (1-6) decreases while the concentration inside the bins on the right (7-10) increases with time. Therefore, a spot like deposition at the right is expected after complete evaporation. However, in the same scenario with droplet of suspension of dead bacteria, we observed that the concentration in bins (1,2,9,10) near the edges increase while the same in bins (3-8) at the center decreases with time as shown in Figure 5.10f. One would expect again that a ring like stain will be left after complete evaporation due to the absence of chemotaxis in dead bacteria. We would like to mention that for the suspension of dead or live bacteria in the absence of any nutrient (Figures 5.10a, 5.10b, 5.10d and 5.10f) the sum of normalized concentrations at all the ten bins adds to value close to unity since the y axis values in the plots were normalized by the total initial count of particles,. However, we noticed that in the presence of sugar crystal (Figures 5.10c and 5.10e) the sum of normalized values at later stages of evaporation (t = 650 s and 800 s) is more than unity. Therefore, it appears that during the time of evaporation there was some bacterial growth in the presence of nutrient.

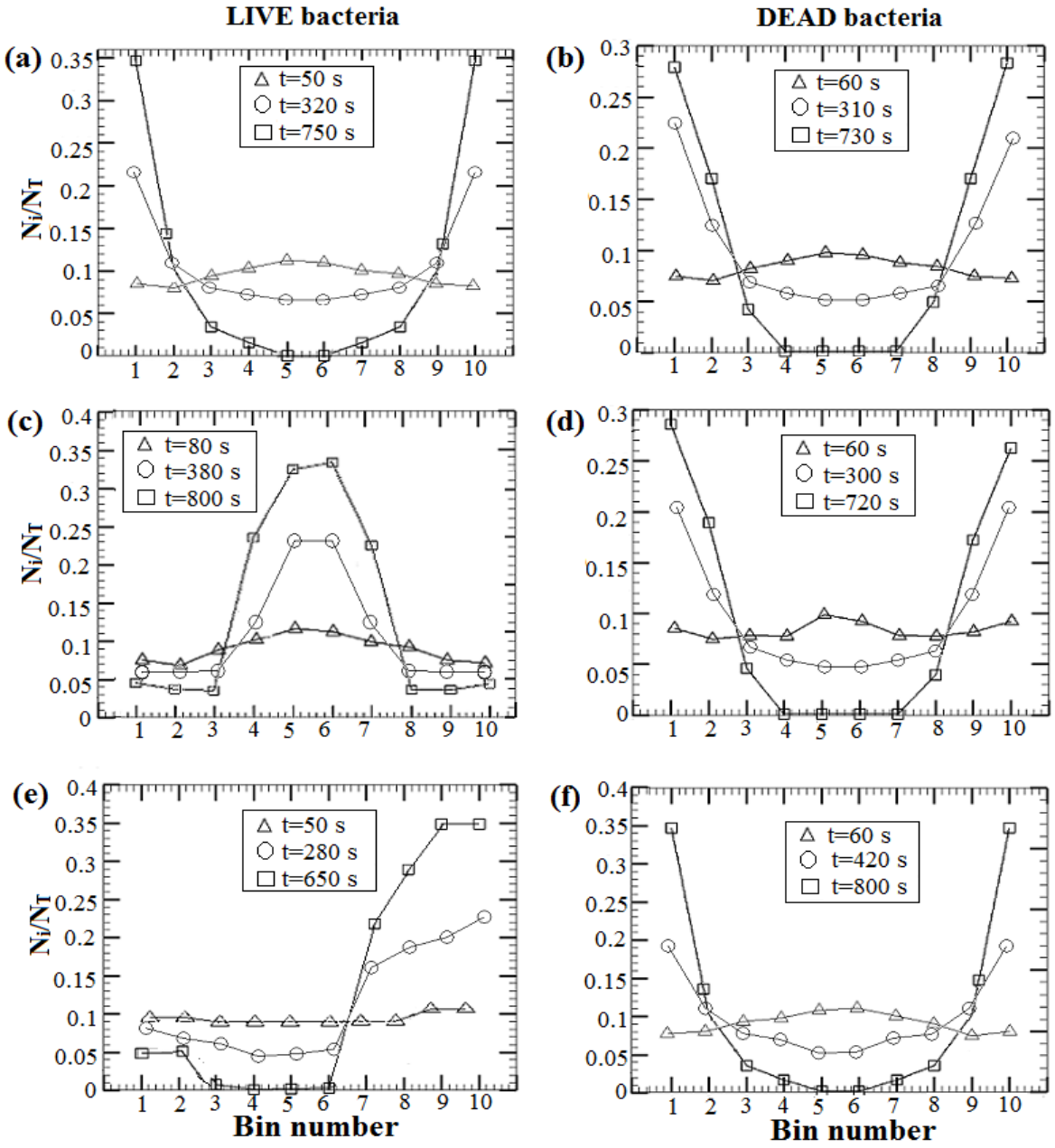


**Figure 5.10.** The changes in concentration of bacteria inside each bin are plotted at early and late stages of evaporation. Left columns represent the concentration of live bacteria in suspension while the right columns illustrates the changes in concentration of dead bacteria. The plots are labeled as follows. (a), b): when there is no sugar on the substrate; (c), (d): when sugar on the substrate is at the center; (e), (f): when sugar on the substrate is on the right side.

The concentration profiles of the evaporating droplet of bacterial suspension in the presence of metal block on the substrate are shown in Figure 5.11. It can be noticed that during the early time, the concentration of the bacteria inside all the bins are nearly the same. As the evaporation progresses there is change in the concentration. The concentration of the live bacteria inside the bins (1, 2, 9 and 10) which are near the edges increases whereas the concentration of the central bins (3-8) decreases with time. This trend was observed in both the Figures 5.11a and 5.11b since the dynamics of bacterial suspension are not significantly different in the absence of nutrient

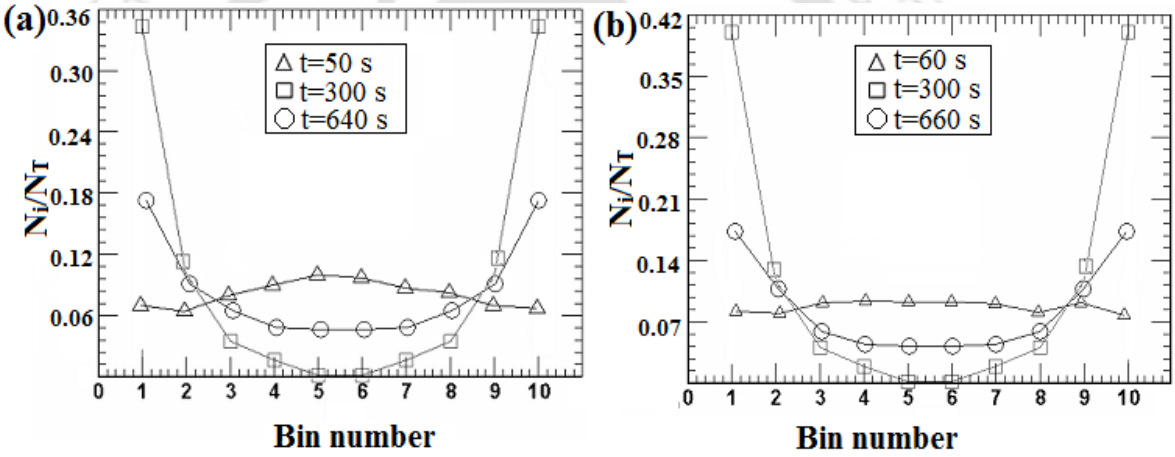


**Figure 5.11.** The normalized count of bacteria inside the bins at three different times (a) metal block on the substrate is at the center of the droplet, (b) metal block on the substrate is on the right side of the droplet.

### 5.3.3 Pattern formation

To verify the predictions of deposition pattern inferred from the velocity and concentration profiles, images of dry pattern left after complete evaporation of 3D droplets of bacterial suspension were acquired. We would like to clarify that in these experiments the droplet was not confined but was placed on the substrate and left to dry out in ambient. Figures

5.12a and 5.12b shows the images of the particles left after the complete drying. In both these cases there was no sugar on the substrate. Qualitative similarity can be observed in both the patterns showing deposition near the rim. Figures 5.12c and 5.12d shows the deposition pattern when a sugar crystal was placed on the center of the substrate. A large spot at the center and ring like stain around the rim is observed when the droplet containing suspension of live bacteria dries out. The spot at the center is the result of bacterial chemotaxis. The ring like stain is due to the fact that towards the end of evaporation (when sugar is completely dissolved and concentration gradient vanishes) some of suspended live bacteria are also transported towards the pinned contact line by the radial outward fluid flow (see the Figure 5.5c). On the contrary, the sugar crystal does not influence the dynamics inside the droplet containing suspension of dead bacteria. Consequently, a ring like deposition was observed for this case as shown in Figure 5.12d.

Figures 5.12e and 5.12f shows the particle deposition when sugar crystal on the substrate was placed on the right side. In this case, the chemotaxis causes the live bacteria to move towards the right and hence the final dried out pattern shows deposition also displaced towards the right, which is clearly visible in Figure 5.12e. However, a ring like deposition (similar to Figure 8a) was observed when the droplet of suspension of dead bacteria was dried out in the presence of sugar crystal placed on the right as shown in Figure 5.12f. This observation is consistent with absence of chemotaxis in dead bacteria.

Figure 5.13 shows the image of the deposition pattern of drying drops in presence of metal block. This shows chemotaxis plays an important role in suppression of the coffee ring formation.

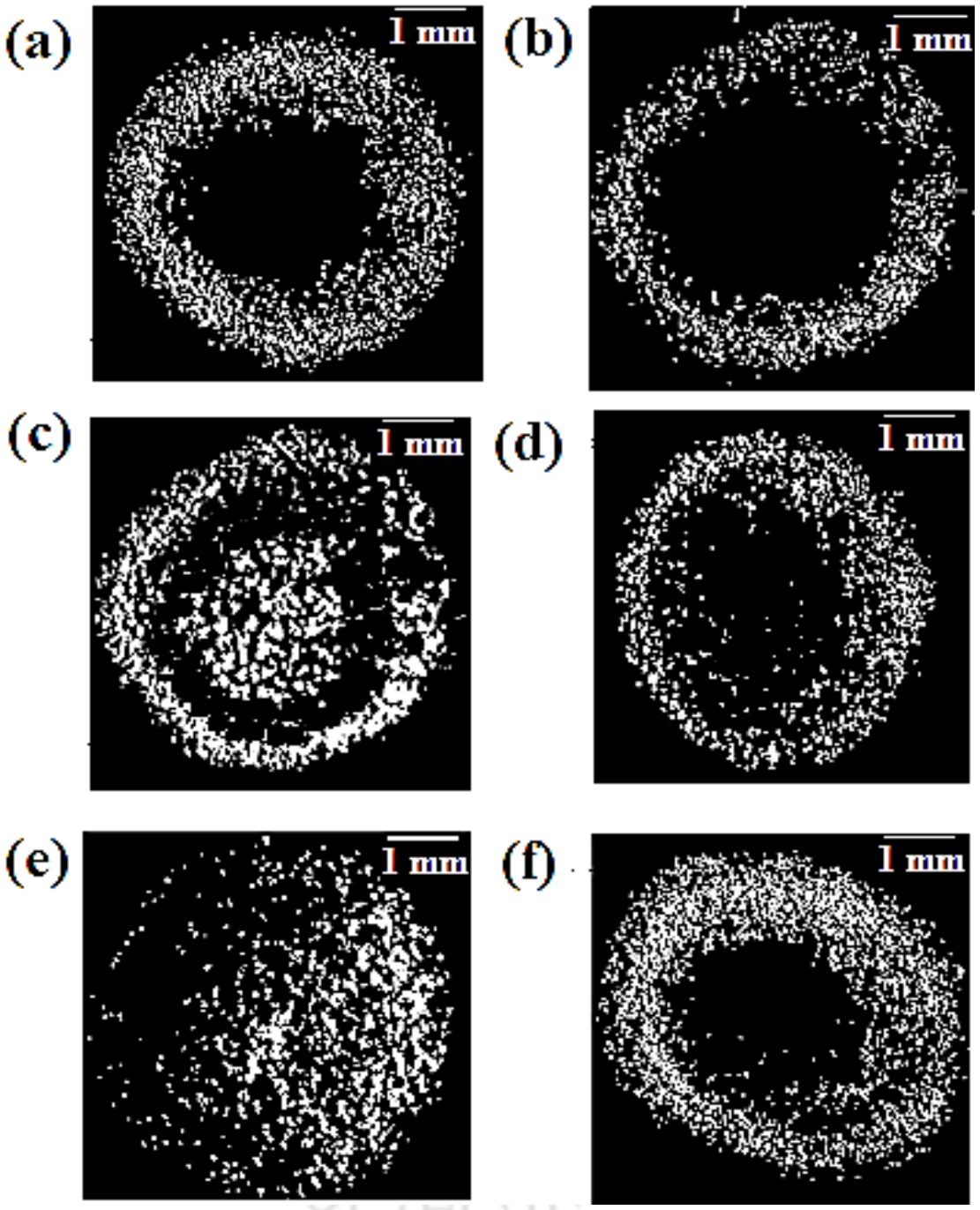


**Figure 5.12.** Photographs of the deposition pattern of suspended bacteria left on the substrate after complete drying of the droplet. (a-b) when there is no sugar on the substrate; (c-d) when sugar on the substrate is at the center of the droplet; (e-f) when sugar on the substrate is on the right side of the droplet. Left column illustrates the deposition pattern of live bacteria and right column shows the deposition pattern of dead bacteria.

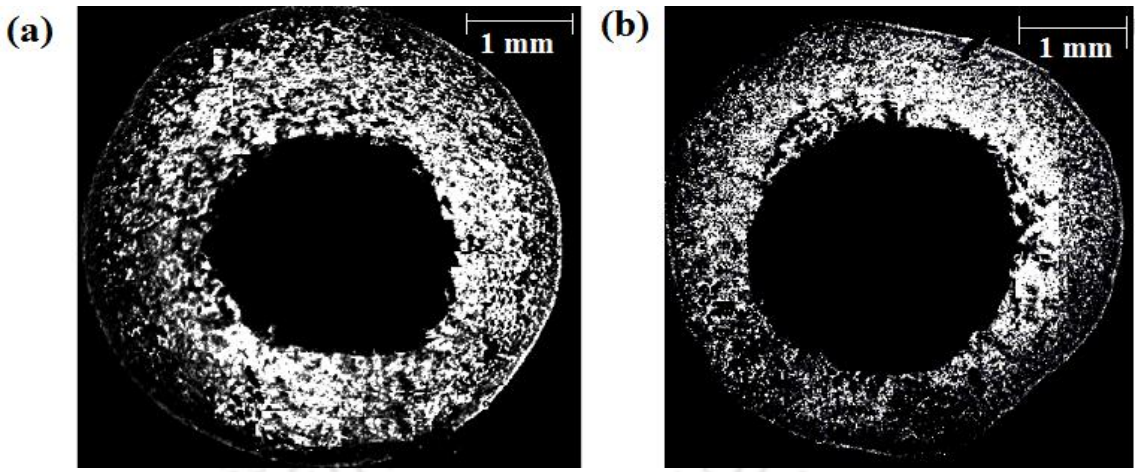


**Figure 5.13.** Photographs of the deposition pattern of bacteria left on the substrate after complete drying of the droplet. (a) The metal block on the substrate was at the center of the droplet; (b) The metal block on the substrate was on the right side of the droplet.

## 5.4 Conclusion

This work demonstrates that formation of coffee ring-like particle deposition pattern can be suppressed by introducing a chemoattractant when a drop containing suspension of live bacteria undergoes evaporation. Flow visualization technique of particle image velocimetry was used to map the velocity and concentration profiles in the presence and absence of bacterial chemotaxis. Two symmetric convection cells were observed during evaporation of droplet of suspension of dead bacteria. On the other hand, the dynamics of live bacteria were found to be strongly influenced by the chemoattractant, as supported by their chemotaxis towards the nutrient site. The final deposition pattern of suspended live bacteria was also shifted toward the food site. The predictions from the velocity fields and concentration profiles obtained from the PIV analysis are found to be in good agreement with the observed deposition pattern.

# CHAPTER 6

# Evaporating droplet on curved surface

## 6.1 Introduction

Patterning is of great importance to create nano- and microstructure material. Transparent conductive coatings are used in a wide range of applications such as displays (LCD, plasma, touch screens, e-paper, *etc*.), lighting devices (electroluminescence, OLED), and solar cells. Layani *et al.* (2014) reported that coffee ring effect can be utilized to obtain a functional property, namely transparency and conductivity, by forming 2-D arrays composed of interconnected conductive rings as shown in Figure 6.1a. With a low cost process of inkjet printing, the fabrication of the arrays is spontaneous. Francois and co-workers (1994) first introduced the breath figure method for preparing microstructured polymer films. The principle is very simple but the method is very challenging. This principle is based on rapid evaporation of solvent that decreases the temperature of the solution/air interface and induces the condensation of water droplets into an ordered hexagonal array favored by the Marangoni convection and arrange into ordered two- or three-dimensional (2D or 3D) arrays. Finally, a film with ordered porous structure is obtained after the solvent and water are thoroughly evaporated (Wan *et al*. 2014) as shown in Figure 6.1b. Recently, Leon *et al*. 2014 reported that the breath figure approach and coffee ring effect could be used to fabricate structured pattern on a relatively large scale.

Less information are available on heat and mass transfer, fluid motion and particle transport of an evaporating droplet on curved surface. In this work, the internal fluid flow and particle transport inside the droplet on curved surface are investigated using the tool of PIV. This work reveals that patterning in the self-assembly can be controlled and is expected to contribute significantly in the fabrication of devices associated with many applications such as sensor, soft lithography and touch screen in smart phone.

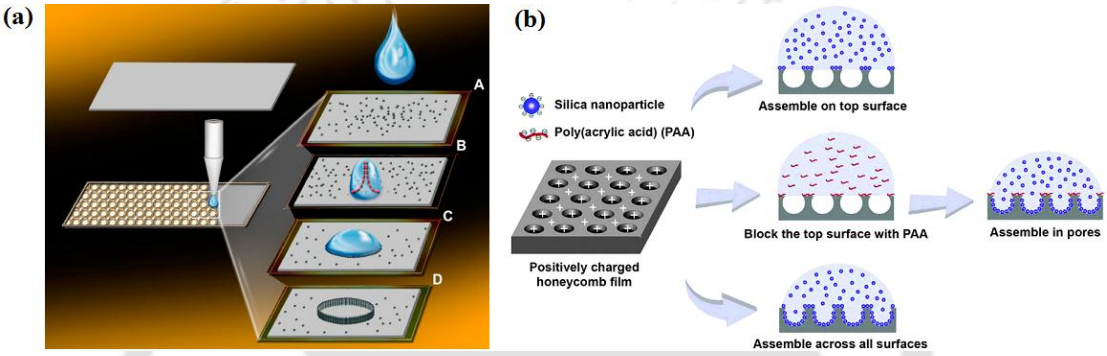


**Figure 6.1.** (a) Schematic diagram to develop smart screen (from Layani et al., 2014, *Appl. Mater. Interfaces*, **6**, 18668−18672. Copyright 2014 by the American Chemical Society); (b) Breath figure (from Want *et al.* 2014, *Chem. Commun.*; **50**:4024–4039. Copyright 2014 by the Royal Society of Science).

## 6.2 Experimental procedure

The experiment setup, that was described in the Chapter-2 was used to determine the internal fluid motion and particle transport inside the liquid microdroplet. The material and thickness of the substrate were also same except the geometry of the substrate is concave shape. The geometry and dimension of the substrate is shown in Figure 6.2a. Using syringe a confined 2D droplet of 75 µl is generated on a curved substrate in between the two non wetting transparent glass slide as shown in Figure 6.2b. The curved geometry was found

to amplify the contact angle of the liquid droplet and the substrate behaves as a hydrophobic material. The initial contact angle ($\theta_o$) of the droplet was 140$^o$ (see Figure 6.4a). The experiments were carried out in ambient condition. As soon as the liquid droplet was placed on a surface, the images of the droplet were captured by CCD camera. These images were used to determine the contact angle, internal fluid motion and average particle density of an evaporating droplet.

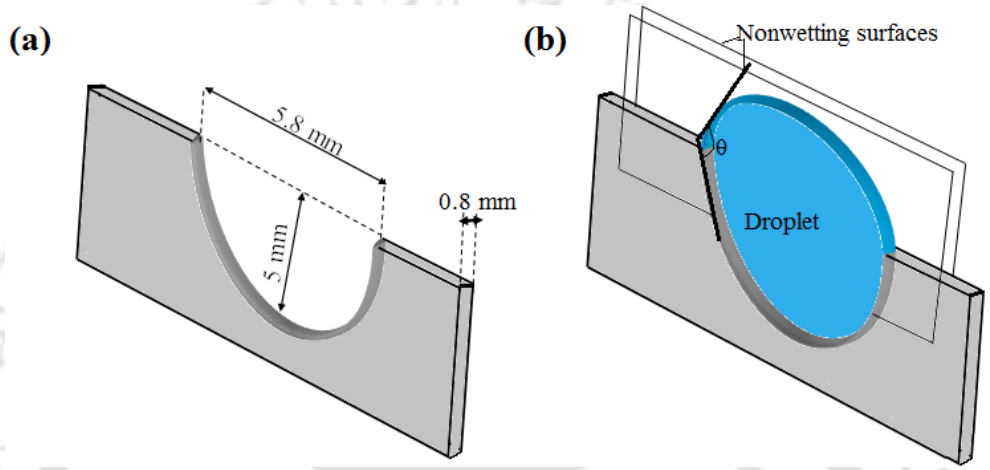


**Figure 6.2.** (a) Schematic diagram of curved geometry of the substrate. (b) Schematic diagram of confined 2D droplet with a contact angle θ.

## 6.3 Results and Discussion

### 6.3.1 Contact angle and surface temperature distribution

As mentioned in previous sections, except for the rate of evaporation the experiments with disc shaped 2D drops have similar evaporation dynamic as the 3D droplets (Jaijus and Singh, 2010). In our experiments the droplet rests on a curved and rough substrate. Since the droplet was confined between two parallel plates, which were nonwetting to water, the top surface was free to move. As the evaporation progresses there is fluid volume loss in the droplet, which makes the contact angle and height of the drop decrease continuously. The contact angle of the droplet was measured from the images. Figure 6.3a shows the

plot of contact angle with time. In this plot, the contact angle θ is normalized by initial contact angle $\theta_o$. It can be observed that dynamics of the contact angle of the evaporating liquid droplet placed on curved surface is similar to liquid droplet evaporating on a flat surface. The contact line of the droplet was found to be unpinned as the evaporation progress with time. It can be more apparent from the time sequences of the images provided in Figure 6.4.

Figure 6.3b shows the plot of temperature distribution along the interface of the droplet. The temperature was measured at the edges, apex and substrate using K-type thermocouples. The surface temperature of an evaporating droplet placed on flat surface in ambient condition monotonically increases from the center to the edge whereas the liquid droplet placed on curved surface shows monotonically decreasing temperature from center to the edge of the droplet. This is expected because for the curved substrate the wetted area is larger than the evaporation area. As a result, the amount of heat loss due to evaporation is always lower than the amount of heat transferred from the substrate to the surface of the droplet. This can be more apparent from the raw images of the droplet provided in Figure 6.5. When the vapor escapes the drop it gives bright image in LED light. As the evaporation progress with time, the area of the white patch along the droplet interface is nonuniform which signifies that the evaporation flux is nonuniform along the droplet interface. The white patch is the water vapor due to evaporation. In the case of droplet evaporating on the flat surface, the area of the white patch decreases as we move from the bottom to the top of the droplet while for the curve surface the area of the white patch is lower near the edges. This indicates that the evaporative cooling effect is more at the top surface of the droplet placed on curved surface. Thus, the apex temperature is lower than the edges temperature of the droplet placed on curved substrate. Petsi and Burganos (2011) also predicted the similar temperature profile.

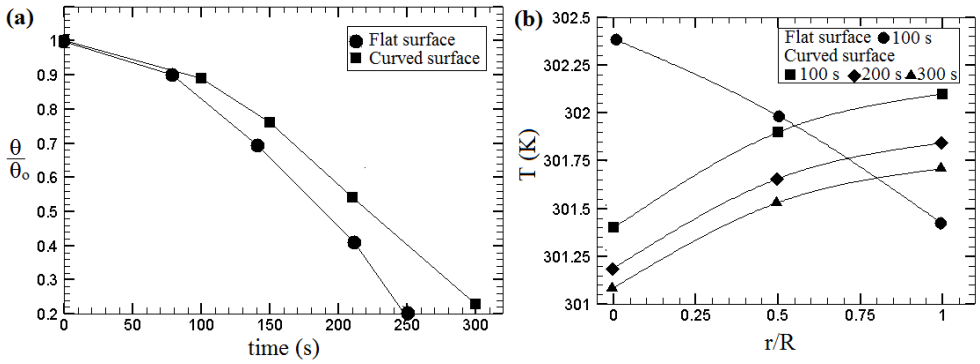


**Figure 6.3.** Comparison of Flat and curved surfaces. (a) Time evolution of contact angle, (b) surface temperature distribution of an evaporating droplet.

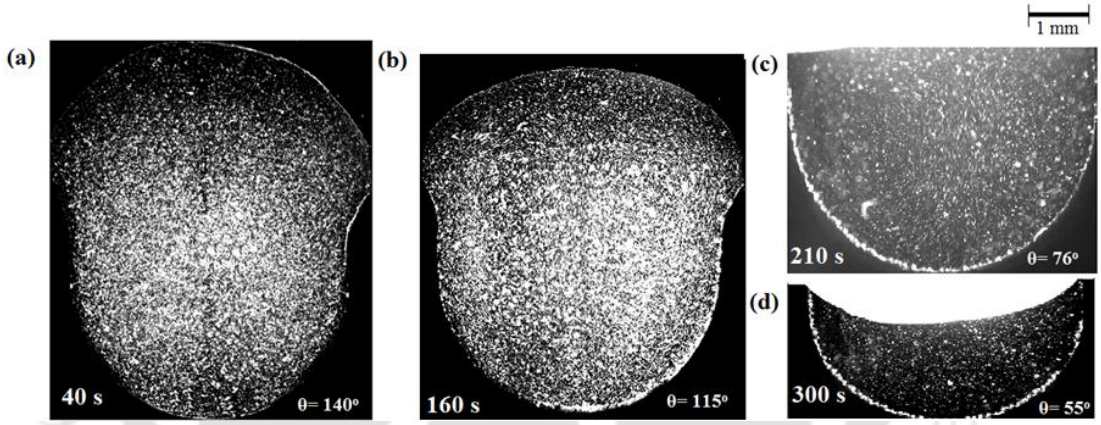


**Figure 6.4.** Time sequence of image of the droplet (a) 40 s (b) 100 s (c) 160 s (d) 210 s (e) 300 s.

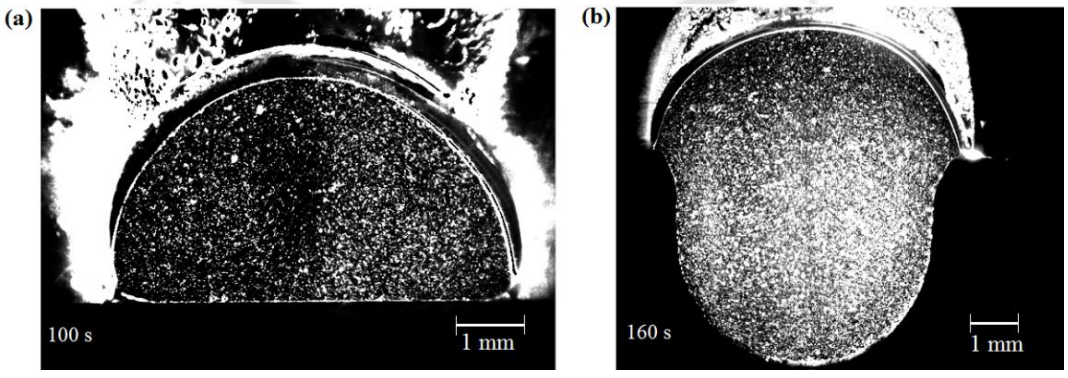


**Figure 6.5.** Images of the evaporating droplet on the surfaces. (a) Flat surface, (b) curved surface. (White patch represent the water vapor along the droplet free surface).

### 6.3.2 Velocity field

In this section, we describe the velocity field inside an evaporating droplet placed on a curved surface. Figures 6.6a shows the velocity vectors superimposed over the velocity contour at 100 s. The measured temperatures at various points in the droplet are also shown in figure. The apex temperature was lower than the temperature at the edge. This temperature difference will create surface tension gradient known as Marangoni stress along the droplet interface. The surface tension will be stronger at the top but weaker at the edge of the droplet. Therefore, the Marangoni stress will drive a fluid motion from the edge toward the apex of the droplet. Two symmetric counter rotating convection cells were observed. The internal fluid flow pattern remains qualitatively the same at various stages as shown in Figures 6.6b- 6.6d. Analysis of dimensionless numbers such as Grahshoff number, Marangoni number and Bond number that indicates the strength of Marangoni flow is more. The evaluated values of these numbers are 54, 5625 and 0.0153 respectively. These numbers indicated that the flow driven by Marangoni stress is strong inside the evaporating droplet. The numerical simulations were carried out for steady state conditions using the boundary temperature profile obtained from the experimental observations. Linearly varying temperature profile between the apex temperature and edge temperature and Marangoni stress were assigned along the right interface and left interface of the droplet. No-slip condition and linear temperature profile between the two edges of the droplet were assigned at the droplet free surface. The velocity vectors superimposed over the velocity contour obtained from the simulations are shown in Figures 6.6 (e-h). The results are in qualitative agreement with the experimental results. From the velocity field, the solute particles present inside the droplet is expected to transport towards the center of the droplet.

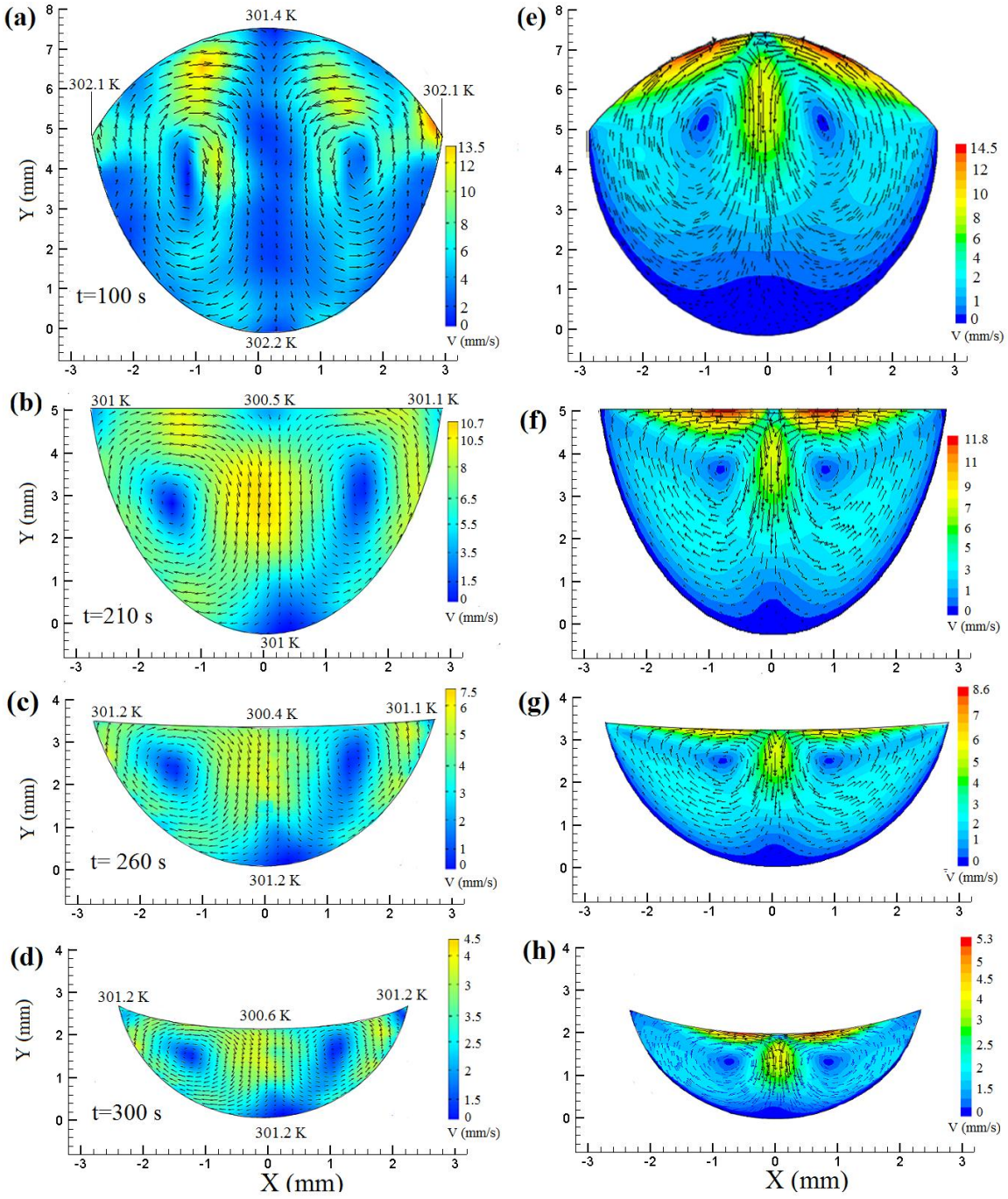


**Figure 6.6.** Velocity field inside the evaporating droplet placed on curved obtained from the experiment at time (a) 100 s (b) 210 s (c) 260 (d) 300 s. The right column (e-h) represent the corresponding velocity field obtained from the numerical simulations.

### 6.3.3 Concentration profile

Figure 6.7a shows the time evolution of averaged particle density ($N_i/N_T$) of solute particles. The normalized particle density at various time instant is plotted against the bin number. Initially, the particles were uniformly distributed in all the bins. As the evaporation proceeds, the convection leads to change in the particle concentration inside the bins. The particle concentration in the central region (bins 4-7) increases with time whereas the particles near the edges (bins 1, 2, 9 and 10) decreases with time. This particle distribution is attributed to the velocity field described in Figure 6.5. Particle deposition is expected to be more at the center of the droplet after complete evaporation.

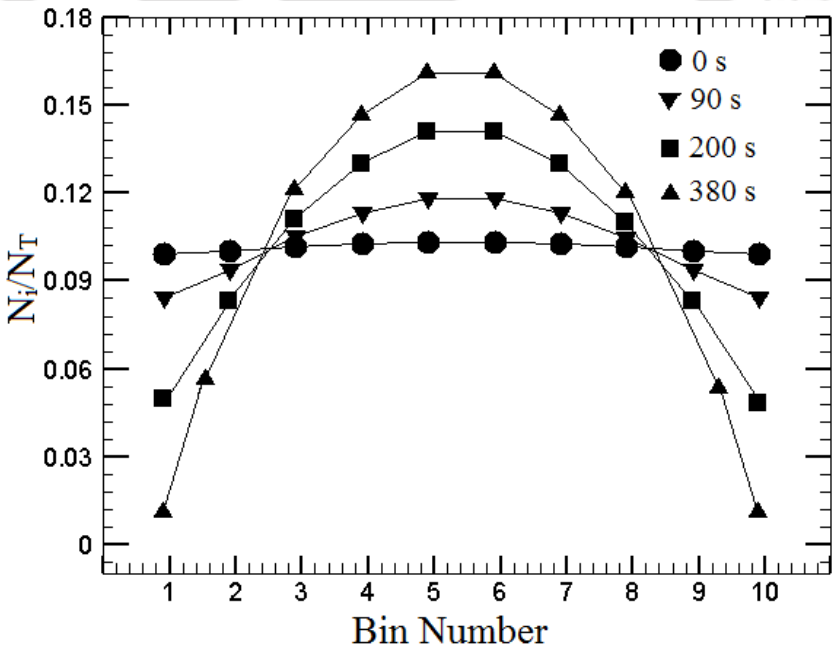


**Figure 6.7.** Particle concentration distribution inside the evaporating droplet at various times.

### 6.3.4 Particle deposition pattern

To verify the prediction of deposition pattern inferred from the concentration profiles, experiments were conducted with drying 3D droplets. Figure 6.8 shows the image of the

particles left after complete drying. The outer rim of the image is the diameter of the well. It can be observed that the deposited particles are more concentrated at the center of the droplet. As mentioned above, the contact line of the droplet recedes as the evaporation progress with time. This may also enhance the particle to deposit more at the center of the droplet. This image confirms that the prediction of particle deposition pattern from the velocity field and concentration profile is true.

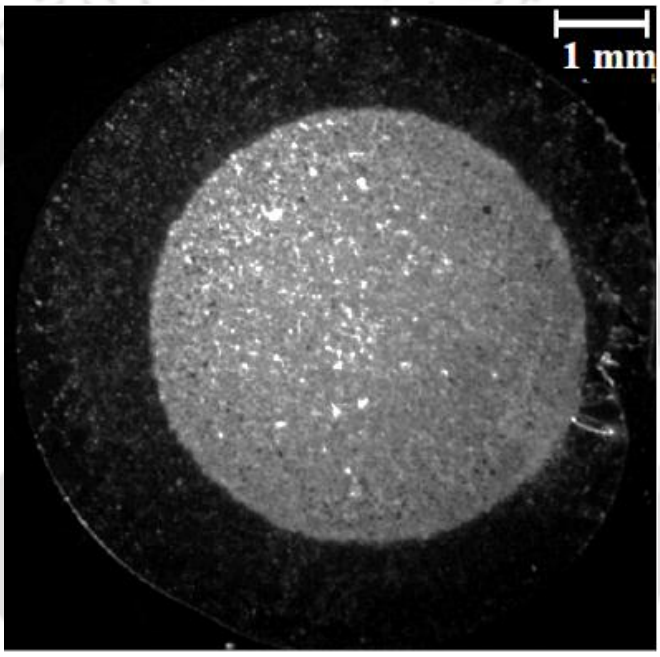


**Figure 6.8.** Photographs of the deposition pattern of polystyrene left on the substrate after complete drying of the droplet.

## 6.4 Conclusion

In this work, the fluid flow and particle transport inside the droplet placed on curved surface were investigated through experimental measurements as well as numerical simulations. It was observed that the curved surface modifies the surface temperature gradient and consequently affects the internal flow pattern and finally suppresses the

coffee ring deposition pattern. Numerical simulation results were in qualitatively good agreement with the experimental observations. The predictions of final deposition pattern from the velocity fields and particles concentration dynamics was confirmed from the image of the dried out particles.

# CHAPTER 7

# Conclusion

This work was aimed at providing insight into the fluid motion and deposition pattern in an evaporating droplet containing dispersed particles. The formation of patterns on substrate depends on the evaporation conditions and physiochemical properties of the dispersed particles. The research discussed in this dissertation highlights that the surface temperature distribution plays an important role in determining the internal fluid pattern and subsequently final deposition pattern. This work also explored the significance of the contact line on the final deposition pattern of an evaporating droplet.

The internal fluid flow and particle deposition of an evaporating droplet placed on the heated substrate were examined in Chapter 2. PIV technique was used to determine the fluid flow and particle transport inside the evaporating drop of dispersed polystyrene particles placed on the heated substrate. For simplicity and avoiding the problems encountered in the 3D PIV experiments on evaporating drop, the 2D PIV technique was used to determine the velocity field inside the evaporating droplet. We have considered four different cases of externally heated substrate. Different flow patterns were revealed inside the evaporating droplet of polystyrene particles subjected to different conditions that were considered in our studies. Two symmetric counter rotating convection cells (anti-clockwise direction at the left half and clockwise direction at the right half) were observed inside the evaporating drop placed on a wetting substrate in ambient condition. The

number of particles present inside the bins nearer to the contact line were found to increase whereas the central bins were found to decrease as the evaporation proceeds. A dark ring like structure was formed on the substrate after completely evaporation. The direction of the internal fluid flow inside the evaporating was found to reverse when the droplet was kept on the heated substrate. The particle density inside the central bins increases and the bins near to the edges decreases with time. A center spot with ring like structure was formed upon complete drying of droplet. When the drop was placed on the asymmetric half heated substrate, single convection cell was observed. The particle on the substrate showed asymmetry deposition pattern after complete evaporation. This clearly showed that the heated substrate modifies the surface temperature distribution of the droplet with pinned contact line thereby, initiating the internal fluid flow which consequently alters the final deposition pattern of the particles. Results from numerical simulations for steady state condition were in qualitative agreement with experiments. The internal fluid flow in the evaporating droplet can result from both Marangoni flow and buoyancy flow. Analysis of dimensionless numbers concluded that the strength of Marangoni flow was dominant over the buoyancy flow inside the evaporating droplet. Experiments were also conducted in such a way that the gravitational effect can be neglected. Similar flow patterns revealed that the fluid flow due to Marangoni stress dominates over the buoyancy flow in small microdroplet. Numerical simulations at the steady state condition with the zero shear stress along the droplet interface also showed that the Marangoni convection is dominant inside the evaporating droplet. Evaporating droplet with dispersed polystyrene particles of different concentration under ambient condition showed similar flow pattern inside the evaporating droplet. However, the magnitude of the velocity was found to decrease with the increase in the concentration of the polystyrene particles.

In Chapter-3, further investigation were carried out to understand the role of contact line on final deposition pattern of drying drop. It was observed that the final deposition pattern of an evaporating droplet with pinned contact line is strongly influenced by the internal fluid flow. When the droplet was subjected to local heating at the drop apex it showed similar internal fluid flow patterns as that of the drop evaporating in ambient condition except that the contact line was found to be unpinned. The contact line diameter decreased with time. The particle deposition pattern showed a center spot with ring like structure near the periphery of the droplet. When the droplet surface near to the contact line was heated at the left, the particle deposition was found to shift towards the left side of the droplet. This shows that the contact line also significantly influence the final deposition pattern in an evaporating droplet. The velocity fields computed from steady state simulation were in qualitative agreement with the experimental observations. The prediction of particle deposition from the contact line, the velocity field and particle concentration of 2D experiment were in good agreement with the final deposition pattern observed for a 3D droplet.

The surface temperature and internal fluid flow during the transition stage of the were examined in Chapter-4. Four states of temperature distribution were found to appear as the evaporation progress with time. At large contact angle of the droplet, the surface temperature distribution is monotonically increasing from the center to the edge, whereas temperature distribution along the droplet free surface was found to reverse at small contact angle of the droplet. Contrarily, the temperature distribution was nonmonotonic along the droplet surface at the intermediate contact angle i.e. it first increases and then decreased toward the edge of the droplet. Toward the end of the process, the temperature distribution along the droplet surface was found to be almost the same. This surface

temperature distribution strongly affects the internal fluid flow pattern. Four distinct flow patterns were revealed inside the evaporating droplet. Monotonic surface temperature distribution results two symmetric convection cells, whereas nonmonotonic temperature distribution showed four vortices inside the droplet. At the end, the radial fluid flow inside the drop was observed. Finally, the dynamics of particle inside the droplet was strongly influenced by the internal fluid. The results obtained from the numerical simulation were in good qualitative agreement with the experimental observations.

In Chapter-5, pattern formation of evaporating droplet of biological fluid was investigated. In this work, the formation of the coffee ring-like pattern was suppressed by introducing a chemoattractant when a drop containing suspension of live bacteria undergoes evaporation. Flow visualization technique of particle image velocimetry was used to determine the velocity and concentration profiles in the presence and absence of bacterial chemotaxis. Two symmetric convection cells were observed during evaporation of droplet of suspension of dead bacteria. On the other hand, the dynamics of live bacteria was significantly influenced by the chemoattractant, as supported by their chemotaxis towards the nutrient site. The final deposition pattern of suspended live bacteria was also shifted towards the food site. The predictions from the velocity fields and concentration profiles obtained from the PIV analysis were found to be in good agreement with the observed deposition pattern. Our results can be employed to develop coffee ring effect based diagnostics to detect presence of live bacteria in poorly sterilized water samples.

Finally, the effect of the geometry of the substrate in evaporating droplet was examined in Chapter-6. The curved geometry of the substrate was found to amplify the contact angle of the droplet and behaves as hydrophobic substrate. The evaporative cooling along the interface was found to strongly influence by the curved surface. In addition, the

dynamics of the contact line, fluid flow pattern and particle deposition pattern were also found to be strongly affected by the geometry of the substrate. The predicted fluid flow patterns inside the droplet through experiment were in qualitative agreement with the numerical simulation results. The coffee ring stain can be suppressed by modifying the geometry of the substrate.

Overall, we have demonstrated that the changes in the experiment conditions results in variation of the particle deposition. This work also revealed that the formation of pattern after complete evaporation of droplet with pinned contact line is strongly influenced by the internal fluid flow in an evaporating droplet. This work also reveals that pattern formation of biological matter (i.e. *E-coli*) can be used for the identifying the nature of the fluids and nature of the dispersed particles in many biological applications. The final deposition pattern also depends on the dynamic of the contact line and structure of the substrate. Furthermore, the results of this work could to lead to control of the coffee ring effect in many microfluidic devices and future development of inexpensive disease diagnostic devices.

There are several opportunities for extending this research works. Further investigation could include the internal fluid flow and particle transport in evaporating 3D droplet. This will improve the understanding of the underlying mechanism in the coffee ring effect. We can also study the fluid motion and particle dynamics inside the evaporating droplet placed on superhydrophobic substrate. Another very interesting work would be studied the fluid motion using two different particle size such that one particle will follow the fluid motion (*Marangoni convection*) driven by the Marangoni stress along the droplet interface and other particle may resist the fluid motion. The coffee ring phenomenon can be further studied to understand the auto separation of particles at the

contact line. In addition, the pattern formation in various biological fluids could create a large database of images. This may improve the development of inexpensive disease diagnostic devices based on pattern recognition technique.

## References


ADACHI, E.; DIMITRO, A.S. & NAGAYAMA, K. 1995 Stripe patterns formed on a glass surface during droplet evaporation, *Langmuir* **11**, 1057–1060

ADRIAN, R. J.; KEANE, R. D. & ZHANG, Y. 1995 Super resolution particle imaging velocimetry. *Meas Sci Technol.* **6**, 754–768.

ADRIAN, R. J.; & WESTERWEEL, J. 2010 Particle image velocimetry. *Cambridge*.

BERTHIER, J. 2008 Microdrops and digital microfluidic. *William Andrew*.

BHARDWAJ, R.; FANG, X.; SOMASUDARAN, P. & ATTINGER, D. 2010 Self-assembly of particles from evaporating colloidal droplets: Role of the pH and proposition of a phase diagram. *Langmuir*, **26**, 7833-7842.

BIGIONI, T.P.; LIN, X.M.; NGUYEN, T.T.; CORWIN, E.I.; WITTEN, T.A. & JAEGER, H.M. 2006 Kinetically driven self-assembly of highly ordered nanoparticle monolayers *Nat Mater*. **5**, 265-270BURTIN, D., SOBAC, B; LOWUET, B. & SAMPOL, J. 2011 Pattern formation in drying drops of blood. *J. Fluid Mech.* **667**, 85-95.

CAREY, P. V. 1992 Liquid–vapour phase-change phenomena. *Taylor Francis*.

CAZABAT, M.; HESLOT, F.; TROIAN* S. M. & CARLES, P. 1990 Fingering instability of thin spreading films driven by temperature gradients. *Nature* **346**, 824-826.

CRIVOI, A. & DUAN, F. 2013 Evaporation-induced branched structures from sessile nanofluid droplets. *J. Phys. Chem. C*, **117**, 7835–7843.

CUI, L.; ZHANG, J.; ZHANG, X.; LI, Y.; WANG, Z.; GAO, H.; TIEQIANG WANG, T.; ZHU, S. YU, H. & YANG, B. 2012 Avoiding coffee ring struc-

ture based on hydrophobic silicon pillar arrays during single-drop evaporation *SoftMatter*, **8**, 10448-10456.

DARNTON, N. C.; TURNER, L. ROJEVSKY, S. & BERG, H. C. 2007 On torque and tumbling in swimming *Escherichia coli. J. Bacteriol.* **189**, 1756–1764.

DAVID, S.; SEFIANE, K. & TADRIST, L. 2007 Experimental investigation of the effect of thermal properties of the substrate in the wetting and evaporation of sessile drops, *Colloids and Surfaces A: Physicochem. Eng. Aspects* **298** 108–114.

DEEGAN, R. D.; BAKAJIN, O.; DUPONT, T. F.; HUBER, G.; NAGEL, S. R. & WITTEN T. A. 1997 Capillary flow as the cause of ring stains from dried liquid drops. *Nature* **389**, 827–829.

DEEGAN, R. D. 1998 Deposition at pinned and unpinned contact lines: Pattern formation and applications. PhD Dissertation (University of Chicago).

DEEGAN, R. D. 2000 Pattern formation in drying drops. *Phys. Rev. E: Stat. Phys., Plasmas, Fluids, Relat. Interdiscip. Top.* **61**, 475–485.

DEEGAN, R. D.; BAKAJIN, O.; DUPONT, T. F.; HUBER, G.; NAGEL, S. R. & WITTEN, T. A. 2000 a Contact line deposit in an evaporating drop. *Phys. Rev. E* **62**, 756–765

DE GENNES, P.G.; BROCHARD-WYART, F. & QUÉRE, D. 2004 Drops, Bubbles, Pearls, Waves. *Springer*.

DREXLER, W. & FUJIMOTO, J.G. 2008 Optical Coherence Tomography: Technology and Applications. *Springer*.

ERAL, H. B.; AUGUSTINE, D. M.; DUITS M. H. G. & MUGELE, F. 2011 Suppressing the coffee stain effect: how to control colloidal self-assembly in evaporating drops using electrowetting. *Soft Matter* **7**, 4954–4958.

FANG, X.; BINGQUAN, L.; ERIC, P.; YOUNG, S. S.; VLADIMIR, A.; SAMUILOV, J. C.; YONG, C.; JONATHAN, C. S.; CHWEN, Y. S. & RAFAILOVICH, H. M. 2006 Drying of DNA droplets. *Langmuir* **22**, 6308-6312.

FISCHER, B.J. 2002 Particle convection in an evaporating colloidal droplet, *Langmuir* **18** 60–67.

GIRARD, F.; ANTONI, M. & SEFIANE, K. 2008 On the effect of Marangoni flow on evaporation rates of water drops, *Lagmuir* **24** 9207-9210.

GIRARD, F.; ANTONI, M. & SEFIANE, K. 2010 Infrared thermography investigation of an evaporating sessile water droplet on heated substrates, *Lagmuir* **26** 4576-4580.

GIRARD, F.; ANTONI, M. FAURE, S. & STEINCHEN, A. 2008 Evaporation and Marangoni convection in small heated water droplet, *Lagmuir* **22** 11085-11091.

GOGOI, S. K.; GOPINATH, P.; PAUL, A.; RAMESH, A.; GHOSH, S. S. & CHATTOPADHYAY, A. 2006 Green fluorescent protein-expressing *Escherichia coli* as a model system for investigating the antimicrobial activities of silver nanoparticles. *Langmuir* **22** 9322-9328.

GULKA, C. P.; SWARTZ, J. D.; TRANTUM, J. R.; DAVIS, K. M.; PEAK, C. M.; DENTO, A. J.; HASELTON, F. R. & WRIGHT, D. W. 2014 Coffee ring as low-resources diagnostics: detection of the malaria biomarker plasmodium falciparum histidine-rich protein-II using-coupled ring of Ni(II)NTA gold-plated polystyrene particles. *Appl. Mater. Interface* **6**, 6257-6263.

HOLMAN, J. P. 2002 Heat transfer, *McGraw-Hill Education. Europe*.

HONG, S.W.; BYUN, M. & LIN, Z. 2009 Robust self-assembly of highly ordered complex structures by controlled evaporation of confined microfluidics, *Angew. Chem. Int. Ed*. **48**, 512–516.

HONG, S.W.; XIA, J. & LIN, Z. 2007 Spontaneous formation of mesoscale polymer patterns in an evaporating bound solution, *Adv. Mater.* **19**, 1413–1417.

HU, H. & LARSON, R. G. 2005 Analysis of the microfluid flow in an evaporating sessile droplet. *Langmuir* **21**, 3963–3971.

HU, H. & LARSON, R. G. 2005 Analysis of the effects of Marangoni stresses on the micro flow in an evaporating sessile droplet. *Langmuir***, 21**, 3972-3980.

HU, H. & LARSON R. G. 2006 Marangoni effect reverses coffee-ring depositions. *J. Phys. Chem. B.* **110**, 7090–7094.

JAIJUS, P. J & SINGH, A. 2010 Flow visualization, and solute transport in evaporating droplets. *AIChE J.* **56**, 1674-1683

JINESH, K. B. & FRENKEN, J. W. M. 2006 Capillary condensation in atomic scale friction: how water acts like a glue. *Phys. Rev. Lett.* **96**, 166103.

JING , J.; REED , J.; HUANG , J.; HU , X.; CLARKE , V.; EDINGTON, J.; HOUSMAN , D.; ANANTHARAMAN , T. S.; B. MISHRA, PORTER , B.; SHENKER , A.; WOLFSON , E.; HIORT, C.; KANTOR ,R.; ASTON C. & SCHWARTZ, D. C. 1980 Automated high resolution optical mapping using arrayed fluid-fixed DNA molecules. *Proc Natl Acad Sci U S A.*, **95**, 8046-8051.

KANG, K. H.; LEE, S. J.; LEE, C. M. & KANG, S. 2004 Quantitative visualization of flow inside an evaporating droplet using the ray tracing method. *Meas Sci Technol.* **15,** 1104-1112.

KANG, K. H.; LIM, H. C.; LEE, H. W. & LEE, S. J. 2013 Evaporation-induced saline Rayleigh convection inside a colloidal droplet. *Phys. Fluids* **25**, 042001.

KILLEN, A. A.; OSSINA, N.; MCGLENNEN, R. C.; MINNERATH, S.; BORGOS, J.; ALEXANDROV, V. & SARVAZYAN, A. 2006 Protein self-organization pattern in dried serum reveal changes in B-cell disorder. *Mol. Diag. Ther.* **10**, 371-380.

LARSON, R.G. 2014 Transport and deposition patterns in drying sessile droplets. *AIChE* **60**, 1538-1571.

LAWMAN, H. & LIANG, H. 2011 High precision dynamic multi-interface profilometry with optical coherence tomography. *Appl. Optics* **50**, 6039-6048

LAYANI, M.; GRUCHKO, M.; MILO, O.; BALBERG, I.; AZULAY, D. & MAGDASSI, S. 2009 Transparent conductive coatings by printing coffee ring arrays obtained at room temperature. *ACS Nano.***3**, 3537-3542.

LEBEDEV-STEPANOV, P. V.; KADUSHNIKOV, R. M.; MOLCHANOV, S. P.; A. IVANOV, A.; MITROKHIN, V. P.; VLASOV, K. O.; RUBIN, N. I.; YURASIK, G. A.; NAZAROV, V. G. & ALFIMOV, M. V. 2013 Self-assembly of nanoparticles in the microvolume of colloidal solution: physics, modeling, and experiment. *Nanotechnologies in Russia* **8**, 137-162.

LEON, A. S.; DEL CAMPO, A.; FRANANDEZ-GARCIA, M.; RODRIGUES-HERNADEZ, J. & MUNOZ-BONILLA, A. 2014 Tuning the pore composition by two simultaneous interfacial self-assembly processes: breath figures and coffee stain. *Langmuir* **30**, 6134-6141.

LU, G.; DUAN; Y. Y.; WANG, X. D. & LEE, D. J. 2011 *Int. J. Heat Mass Transfer*. **54**, 4437-4447.

MARIN, A.G.; GELDERBLOM, H.; LOHSE, D. & SNOEIJAR, J.H. 2011 Order-to-disorder transition in ring-shaped colloidal stains. *Phys. Rev. Lett.*, **23**, 091111.

MAJUMDER, M.; RENDALL, C.S.; EUKEL, J.A.; WANG, J.Y.L.; BEHABTU, N.; PINT, C.L.; LIU, T.Y.; ORBAEK, A.W.; MIRRI, F.; NAM, J.; BARRON, A.R.; HAUGE, R.H.; SCHMIDT, H.K. & PASQUALI, M. 2012 Overcoming the ‘‘coffee-stain’’ effect by compositional Marangoni flow-assisted drop-drying, *J. Phys. Chem. B* **116**, 6536–6542.

MAKI, K. L. & KUMAR, S. 2011 Fast evaporation of spreading droplets of colloidal suspension. *Langmuir*, **27,** 11347–11363.

MANUKYAN, S.; SAUER, H. M.; ROISMAN, I. V.; BALDWIN, K. A.; FAIRHURST, D. J.; LIANG, H; VENZMER, J. & TROPEA, C. 2013 Imaging internal flows in a drying sessile polymer dispersion drop using spectral radar optical coherence tomography (SR-OCT). *J. Colloid Interface Sci.* **395**, 287-293.

MINOR, G.; OSHKAI, P. & DJILALI, N. 2007 Optical distortion correction for liquid droplet visualization using the ray tracing method: further considerations. *Meas. Sci. Technol.* **18**, 23–28.

MOFFAT, J.R.; SEFIANE, K.; SHANAHAN. M.E.R. 2009 Effect of $TiO_2$ Nanoparticles on Contact Line Stick−Slip Behavior of Volatile Drops *J Phys Chem B*, **113**, 8860.

MOFFAT, J.R. SEFIANE, K. & SHANAHAN M.E.R. 2009a Nanofluid droplet evaporation kinetics and wetting dynamics on flat substrates *J Nano Res-SW*, **7**, 75-80.

NELLIMOOTTIL, T. T.; RAO, P. N.; GHOSH, S. S. & CHATTOPADHYAY, A. 2007 Evaporation-induced patterns from droplets containing motile and non-motile bacteria. *Langmuir* **23**, 8655-8658.

NILGHAZ, A.; ZHANG, L. & SHEN, W., 2015. Coffee-stain on paper. Chem. Engg. Sci. 129, 34–41.

OREJON, D.; SEFIANE, K. SHANAHAN, M.E. 2011 Stick–Slip of Evaporating Droplets: Substrate Hydrophobicity and Nanoparticle Concentration**.** *Langmuir*, **27**, 12834-12843.

PAULIAC-VAUJOUR, E.; STANNARD, A.; MARTIN, C. P.; BLUNT, M. O.; NOTINGHER, I.; MORIARTY, P. J.; VANCEA, I. & THIELE, U. 2008 Fingering instabilities in dewetting nanofluids. *Phys. Rev. Lett.* **100**, 176102.

PEREIRA, F.; LU, J.; CASTANO-GRAFF, E. & GHARIB,M. 2007 Microscale 3D flow mapping with μDDPIV. *Exp. Fluids* **42**, 589-599.

PETSI, A. J. & BURGANOS, V. N. 2005 Potential flow inside an evaporating cylindrical line. *Phys. Rev. E***, 72**, 047301.

PETSI, A.J.; KALARAKIS, A.N. & BURGANOS, V.N., 2010. Deposition of Brownian particles during evaporation of two-dimensional sessile droplets. Chem. Engg. Sci. **65**, 2978–2989.

POPOV Y.O. 2005 Evaporative deposition patterns, spatial dimension of the deposit, *Phys Rev E*. **71** 036313-1-036313-17.

RISTENPART, W. D.; KIM, P. G.; DOMINGUES, J. & STON, H.A. 2007 Influence of substrate conductivity on circulation reversal in evaporating drops. *Phys. Rev. Lett*. **99**, 234502.

RUAN, C. Y.; LOBASTOV, V. A.; VIGLIOTTI, F.; CHEN, S. & ZEWAIL; A. H. 2004 Ultrafast electron crystallography of interfacial water. *Science* **304**, 80.

SAGAWA, T.; KIKUCHI, Y.; INOUE, Y.; TAKAHASHI, H.; MURAOKA, T.; KINBARA, K.; ISHIJIMA, A. & FUKUOKA, H. 2014 Single-cell *E. coli* response to an instantaneously applied chemotactic signal. *Biophys. J.* **107**, 730–739

SAHA, A.; BASU, S.; SURYANARAYANA, C. & KUMAR, R. 2010 Experimental analysis of thermophysical processes in acoustically levitated heated droplets, *Int. J. Heat Mass Transfer* **53**, 5663–5674.

SAVINO, R. & MONTI, R. 1996 Buoyancy and surface-tension driven convection in hanging drop protein crystallizer, *J Cryst Growth* **165**, 308–318.

SAVINO, R.; PATERNA, D. & FAVALORO, N. 2002 Buoyancy and Marangoni Effects in an Evaporating Drop, *J. Thermophys Heat Transfer* **4**, 562-574.

SEFIANE, K. 2010 On the formation of regular patterns from drying droplets and their potential use for bio-medical applications. *J. Bionic Engg.* **7**, S82–S93.

SEMPLES, W.; DIER, R. D.; MIZUNO, H.; JOHAN, H. & VERMANT, J. 2013 Auto-production of biosurfactants reverses the coffee ring effect in a bacterial system. *Nat. Commun.* **4**, 1757.

SHABALIN, V. N. & SHATOKHINA, S. N. 2007 Diagnostics markers in the human biological liquids. *Singap. Med. J.* **48**, 404-446.

SHEN, X.; HO, C. M. & WONG, T. S. 2010 Minimal Size of Coffee Ring Structure. *J. Phys. Chem.* B **114**, 5269–5274.

SIRRINGHAUS, H.; KAWASE, T; FRIEND, R. H.; SHIMODA, T. & INBASEKARAN, M.; WU, W. & WOO, E. P. 2000 High resolution ink-jet printing of all-polymer transistor circuits. *Science* **290**, 2123-2126.

SOMMER, A.P. 2007 Microtornadoes under a nanocrystalline igloo: results predicting a worldwide intensification of tornadoes. *Cryst. Growth Des.* **7**, 1031-1034.

SOMMER, A.P. & ROZLOSNIK, N. 2005 Formation of crystalline ring patterns on extremely hydrophobic supersmooth substrates: extension of ring formation paradigms. *Cryst. Growth Des.* **5**, 551-557.

SOMMER, A. P. & ZHU, D. 2007 Comments on Evaporation-induced patterns from droplets containing motile and non-motile bacteria. *Langmuir* **23**, 11941-1194.

SOMMER, A. P.; CARON, A. & FECHT, H. J. 2008 Tuning nanoscopic water layers on hydrophobic and hydrophilic surfaces with laser light. *Langmuir* **24**, 635-636.

SOMMER, A. P. & FRANKE, R. P. 2003 Biomimicry patterning with nanosphere suspensions. *Nano Lett.* **3**, 573-575.

STEINCHEN, A. & SEFIANE K. J. 2007 Self-organised marangoni motion at evaporating drops or in capillary menisci – thermohydrodynamical model *Non-Equilib. Thermodyn.*; **30**, 39-51.

STIFTER, D. 2007 Beyond biomedicine: a review of alternative applications and developments for optical coherence tomography. *Appl. Phys. B* **88**, 337-357.

TARASEVICH, Y. Y. 2005 Simple analytical model of capillary flow in an evaporating sessile drop. *Phys. Rev. E,* 72, 027301.

TARASEVICH, Y. Y. & PRAVOSLAVNOVA, D. M. 2007 Drying of a multicomponent solution drop on a solid substrate: Qualitative analysis. *Tech. Phys.* **52**, 159–163.

THIELICKE, W. & STAMHUIS, E. J. 2005 Time-resolved digital particle image velocimetry tool for matlab. *PIVlab*.

THOKCHOM, A. K.; GUPTA, A.; JAIJUS, P. J. & SINGH, A. 2014 Analysis of fluid flow and particle transport in evaporating droplets exposed to infrared heating. *Int. J. Heat Mass transfer* **68**, 67-77.

TRANTUM, J. R.; BAGLIA, M. L; EAGLETON, Z. E; MERNAUGH, R. L. & HASELTON, F.R. 2014 Biosensor design based on Marangoni flow in an evaporating droplet. *Lab Chip* **14**, 315-324.

TRANTUM, J. R.; EAGLETON, Z. E.; PATIL, C. A.; SCHWARTZ, M. T.; BAGLIA, M. L.; SKALA, C. S. & HASELTON, F. R. 2013 Cross-sectional tracking of particle motion in evaporating drops: flow field and interfacial accumulation. *Langmuir* **29**, 6221-6231.

TRANTUM, J. R; EAGLETON, WRIGHT, D.W. & HASELTON, F. R. 2012 Biomarker-mediated disruption of coffee-ring formation as a low cost resource diagnostic indicator. *Langmuir* **28**, 2187-2193.

TUVAL, I.; CISNEROS, L.; DOMBROWSKI, C.; WOLGEMUTH, C. W.; KESSLER, J. O. & GOLDSTEIN, R.E. 2005 Bacterial swimming and oxygen transport near contact lines. *Proc Natl Acad Sci U S A.*, 102, 2277–2282.

UENO, I. & KOCHIYA, K. 2008 Effect of evaporation and solute capillary-driven flow upon motion and resultant deposition of suspended particles in volatile droplet on solid substrate. *Adv. Space Res.*, **41**, 2089-2093.

VINCENT, D.; JÉRÔME, B. & ELIANE, S. 2005 Droplet evaporation study applied to DNA chip manufacturing. *Langmuir* **21,** 9130-9136.

WADHAMS, G. H. & ARMITAGE, J. P. 2004 Making sense of it all: bacterial chemotaxis. *Nat. Rev. Mol. Cell Biol.* **5,** 1024–1037.

WAN, L.; H.; ZHU, L. W.; OU, Y. & XU, Z. K. 2014 Multiple interfaces in self-assembled breath figures. *Chem. Commun.* **50**, 4024-4039.

WEN, J. T.; HO, C. M. & LILLEHOJ, P. B. 2013 Coffee ring aptasensor for rapid protein detection. *Langmuir* **29,** 8440−8446.

WEON, B. M. & JE, J. H. 2013 Fingering inside the coffee ring. *Phys. Rev. E* **87,** 013003.

WIDJAJA, E. & HARRIS, M.T. 2008 Particle deposition study during sessile drop evaporation. *AIChE J*. **54,** 2250–2260.

WIDAWSKI, G.; RAWISO, M. & FRANCOIS, B. 1994 Self-organized honeycomb morphology of star polymerpolystyrene films. Nature **369,** 5457-5471.

WIDJAJA, E. & HARRIS M.T. 2008 Particle deposition study during sessile drop evaporation, *AIChE J*. **54** 2250–2260.

WONG, T. S.; CHEN, T. H.; SHEN, X. & HO, C. M. 2011 Nanochromatography driven by the coffee ring effect. *Anal. Chem.* **83,** 1871–1873.

XIE, Y.; GUO, S.; GUO, C.; HE, M.; CHEN, D.; JI, Y.; CHEN, Z.; WU, X.; LIU, Q. & XIE, S. 2013 Controllable two-stage droplet evaporation method and its nanoparticle self-assembly mechanism. *Langmuir* **29,** 6232−6241.

XU, J.; LUO, J. & GUO, D. Criterion for reversal of thermal Marangoni flow in drying drops. *Langmuir* **26,** 1918-1922.

XU, J.; XIA, J. & LIN, Z. 2007 Evaporation-induced self-assembly of nanoparticles from sphere-on-flat geometry. *Angew. Chem. Int. Ed.* **46**, 1860–1863.

YUNKER, P. J.; STILL, T.; LOHR, M. A. & YODH. A. G., 2011. Suppression of the coffee-ring effect by shape-dependent capillary interactions. *Nature* **476**, 308-311.

ZHANG; J. Y.& MELTON, L. A. 1994 Numerical simulations and restorations of laser droplet-slicing images *Appl. Opt.* 33, 192-200.

ZHANG, K.; MA, L.; XU, X.; LUO, J. & GUO, 2014 D. Temperature distribution along the surface of evaporating droplets. *Phys. Rev. E.* **89**, 032404.

ZHANG, N. & WANG, W.J. 1982 Natural convection in evaporating minute drops, J Heat Transfer **62**, 756–765.

ZHANG, W.; YU, T.; LIAO, L. & CAO, Z. 2013 Ring Formation from a drying sessile colloidal droplet. *AIP Adv.*, **3**,102109.

ZHU, Y. & GRANICK, S. 2001 Viscosity of interfacial water. *Phys. Rev. Lett.***,** 87, 096104.

# Research output

| Sl. no. | Published Journal Articles/ Manuscripts to be submitted or under preparation |
|---|---|
| 1 | **Ashish Kumar Thokchom**, Subrata Kumar Majumder and Anugrah Singh. Control of internal fluid flow and particle deposition patterns in externally heated sessile droplets. (Under review). |
| 2 | **Ashish Kumar Thokchom**, Rajaram Swaminathan, and Anugrah Singh. Fluid flow and particle dynamics inside an evaporating droplet containing live bacteria displaying chemotaxis. Langmuir, 2014, 30(42), 12144–12153. |
| 3 | **Ashish Kumar Thokchom**, Abhishek Gupta, Pallippadan Johny Jaijus, Anugrah Singh. Analysis of fluid flow and particle transport in evaporating droplets exposed to infrared heating. Int. J. Heat Mass transfer, 2014, 68, 67-77. |
| 4 | **Ashish Kumar Thokchom**, Subrata Kumar Majumder and Anugrah Singh. Analysis of heat transfer and fluid flow inside an evaporating sessile droplet. (manuscript under preparation). |

| Sl. no. | Conference |
|---|---|
| 1 | **Ashish Kumar Thokchom**, Rajaram Swaminathan, and Anugrah Singh. Visualization of internal flow patterns and particle dynamics in evaporating droplet of active suspension. CompFlu, Dec 22-24 2014, JNCASR, Bangalore |
| 2 | **Ashish Kumar Thokchom** and Anugrah Singh. Analysis of heat transfer and fluid flow inside an evaporating sessile droplet. CompFlu 22-24 Dec 2014 2014, JNCASR, Bangalore. |
| 3 | **Ashish Kumar Thokchom**, Abhishek Gupta and Anugrah Singh, Dynamics of particle deposition in a heated evaporating droplet containing solute particles. International Conference on Multiphase Flow (ICMF-2013), 26-31 May 2013, Jeju, South Korea. |
| 4 | **Ashish Kumar Thokchom**, S K Majumder and Anugrah Singh. Effect of external heating on fluid flow and particle transport in evaporating droplets. CAFE 2012, Noida. |